Application of High-Throughput Screenings on the Interfaces of Chemistry, Biology and Material Science

Zur Erlangung des akademischen Grades eines

DOKTORS DER NATURWISSENSCHAFTEN
(Dr. rer. nat.)
von der KIT-Fakultät für Chemie und Biowissenschaften
des Karlsruher Instituts für Technologie (KIT)

genehmigte

Dissertation

von

Maximilian Seifermann, M. Sc.

aus Rastatt

Tag der mündlichen Prüfung: 06.02.2024
Dekan: Prof. Dr. Martin Bastmeyer
Referent: Prof. Dr. Pavel Levkin
Korreferent: Prof. Dr. Patrick Théato

Kurzfassung

In den letzten Jahrzehnten führte der technologische Fortschritt einer schnell wachsenden Bevölkerung mit einer kontinuierlich steigenden Lebenserwartung. Damit einhergehend steigen die Anforderungen an Wirtschafft und Wissenschaft. Infektionskrankheiten breiten sich weiter aus und die krankheitsverursachenden Viren und Bakterien werden resistenter, die Entwicklung neuer Medikamente wird dringlicher. Gleichzeitig besteht die Notwendigkeit mit sämtlichen Ressourcen möglichst sparsam und umweltschonend umzugehen. Diese Herausforderung einerseits die wissenschaftliche Leistung zu steigern und andererseits Kosten und negative Einflüsse auf die Umwelt zu reduzieren kann auf verschiedene Weisen angegangen werden, Ansätze sind z.B. grüne Chemie, Chemoinformatik oder Miniaturisierung. Diese Arbeit konzentriert sich auf die Anwendung von Miniaturisierung in der Hochdurchsatz-Experimentation mit dem Ziel, ihren Anwendungsbereich zu erweitern und gleichzeitig die Menge der verbrauchten Materialien zu verringern. Ansatz wird durch das Droplet MicroArray (DMA) ermöglicht, ein Array von hydrophilen Spots auf einem superhydrophoben Hintergrund. Die Plattform ist kompatibel mit Flüssigkeits-volumina bis in den einstelligen Nanoliter-bereich und eignet sich für verschiedene experimentelle Ansätze wie Zellkultur, Festphasen- oder Lösungschemie und Polymerisation.

Diese Arbeit ist in drei Teile unterteilt, die sich alle um die Anwendung des DMA an der Schnittstelle verschiedener wissenschaftlicher Disziplinen wie Biologie, Chemie und Materialwissenschaft drehen. Der erste Teil zeigt die Anwendung des DMA als Plattform zur Generierung und Analyse von Materialien im Nanoliter-Maßstab. Etwa 1000 verschiedene binäre Materialien werden im Maßstab von 130 nL pro Probe hergestellt, und dann werden ihre Photodegradationskurven unter Verwendung von Fluoreszenzmikroskopie aufgezeichnet. Durch die anschließende Kombination der Hochdurchsatzplattform mit Machine Learning wird auf potenziell effizientere Weise die Entdeckung neuer Materialien für die Anwendung in verschiedenen Bereichen ermöglicht. Ein abschließendes Experiment vergleicht die Eigenschaften der Materialien generiert von Messungen auf Nanoliter- und Mikrolitermaßstab und zeigt eine gute Übereinstimmung der Zersetzbarkeit zwischen den beiden Maßstäben.

Die beiden folgenden Teile präsentieren Ansätze zur Synthese neuartiger Moleküle mit therapeutisch interessanten Strukturmotiven sowie deren chemische und biologische Charakterisierung in einer In-situ-Screening-Pipeline. Die beiden vorgestellten Ansätze ermöglichen die Synthese und Bewertung von Molekülen, die Inhibitoren oder Proteolysis-Targeting-Chimeras (PROTACs) ähneln und zur Behandlung der Überaktivierung der Mitogen-aktivierten Protein-Kinase-Kinase (MEK) in menschlichen Krebszellen eingesetzt werden. Beide Pipelines werden chemisch charakterisiert, um eine präzise Kontrolle über die freigesetzte Menge an Zielmolekülen für ein nachfolgendes biologisches Screening zu gewährleisten und die durchschnittliche Reinheit der freigesetzten Verbindungen zu quantifizieren. Der synthetische Erfolg der Bibliotheksvorbereitung wird anschließend mit MALDI-TOF-MS quantifiziert. Die charakterisierten chemischen Workflows werden verwendet, um die Verbindungen in einem auf Fluoreszenzmikroskopie basierenden Test gegen HT-29 menschliche Dickdarmkrebszellen zu screenen, wobei Propidiumiodid-Färbung verwendet wird, um potente Wirkstoffkandidaten zu identifizieren. Schließlich werden ausgewählte Verbindungen für Dose-Response-Messungen in einer 384-Well-Platten mittels Luciferase-basiertem Viabilitätstest verwendet, um die Aktivität der identifizierten Verbindungen zu bestätigen und mit von der FDA zugelassenen Medikamenten zu vergleichen.

Abstract

Technological advances over the recent years have allowed for a rapidly growing population with a continuously rising life expectancy. Due to this, the demands in many aspects of economy and science are rising. Infectious diseases spread further and become more resistant, the development of new types of medications becomes more urgent, but on the other hand the need to conserve resources while doing so is at an all-time high. This paradox of increasing the scientific output while reducing the negative environmental impact and the associated costs can be tackled in different ways, such as green chemistry, computational chemistry or miniaturization. This work focuses on the application of miniaturization in high-throughput experimentation to expand the scope of its abilities while decreasing the amounts of consumed materials to achieve a more sustainable way of doing so. This approach is enabled by the droplet microarray (DMA), an array of hydrophilic spots on a superhydrophobic background. The platform is compatible with volumes down to single-digit nanoliters of liquid and is compatible with various different experimentation approaches, such as cell culture, solid-phase- or solution chemistry or materials preparation.

This work is separated into three parts, all of them revolving around the application of the DMA on the interface of different scientific disciplines such as biology, chemistry and material science. The first part shows the application of the DMA as a platform to generate and analyze materials on a nanoliter scale. Approximately 1000 different materials are prepared on a scale of 130 nL per sample and then their photodegradation curves are recorded using fluorescence microscopy. By combining the high-throughput platform with machine learning approaches, a potentially more efficient way of discovering new materials for the application in different fields is achieved. A final experiment compares the nanoscale materials properties with properties gained from bulk materials and shows good translation of the materials degradability between the two scales.

The subsequent two parts show approaches for the synthesis of novel molecules bearing therapeutically interesting structural motifs together with their chemical and biological characterization in an *in-situ* screening pipeline. The two approaches shown allow the synthesis and evaluation of molecules resembling inhibitors or proteolysis-targeting chimeras (PROTACs) that are applied to treat mitogen-activated protein kinase kinase (MEK) overactivation in human cancer cells. Both pipelines are chemically characterized using LC-MS to gain precise control over the released amount of target molecules for a subsequent biological screening and to quantify the average purity of the released compounds. The synthetic success of the library preparation is then quantified using MALDI-TOF-MS. The characterized chemical workflows are applied to screen the compounds against HT-29 human colon cancer cells in a fluorescence microscopy-based assay using propidium iodide staining to identify potent drug candidates. Finally, selected compounds are used for dose-response measurements using a luciferase-based viability assay in 384 well plates to confirm the activity of the identified compounds and to compare it to standard FDA-approved drugs.

Preface

This Thesis is based on results of my research in the group of Prof. Dr. Pavel Levkin between February 2021 and February 2024 at the INSTITUTE OF BIOLOGICAL AND CHEMICAL SYSTEMS – FUNCTIONAL MATERIAL SYSTEMS (IBCS-FMS) at KARLSRUHE INSTITUTE OF TECHNOLOGY (KIT).

Parts of the results presented in Chapter 2.1 were obtained in collaboration with Dr. PATRICK REISSER (KIT) and Prof. PASCAL FRIEDERICH and were published in *small methods*.[1] Those parts are marked as such in the text.

The results shown in chapter 2.2 were obtained in close collaboration with JULIUS HÖPFNER (KIT). The preparation of the substrates as well as the amidation steps and the biological on-chip screening were performed by MAXIMILIAN SEIFERMANN (KIT). All SUZUKI-couplings on-chip and in bulk, as well as the preparation of the on-chip MALDI samples after the final step of the synthesis were performed by JULIUS HÖPFNER (KIT). The experimental planning, the preparation of LC-MS samples and the dose-response measurements were performed together. The analysis of the entire raw data was done independently. Experimental work performed by JULIUS HÖPFNER is indicated as such in the text.

The raw materials for the miniaturized synthesis in chapter 2.3 were synthesized and provided by Dr. YE TIAN (KIT). Those parts are marked as such in the text. Parts of this chapter were published in *small.*[2]

MALDI-MS and MALDI-MSI measurements in chapter 2.2 and 2.3 were performed in collaboration with Dr. STEFAN SCHMIDT and Prof. CARSTEN HOPF, CENTER FOR MASS SPECTROMETRY AND OPTICAL SPECTROSCOPY, UNIVERSITY OF APPLIED SCIENCE in Mannheim. LC-MS measurements took place at the INSTITUTE OF NANOTECHNOLOGY (INT) in the laboratory of DR. FLORIAN FEIST. HT-29 cells were initially cultured by CHARLOTTE LUCHENA (KIT).

Affidavit

Hiermit versichere ich, diese Arbeit selbstständig verfasst zu haben, dass ich keine anderen als die angegebenen Quellen und Hilfsmittel benutzt habe, dass ich die wörtlich oder inhaltlich übernommenen Stellen als solche kenntlich gemacht habe und die Satzung des KIT zur Sicherung guter wissenschaftlicher Praxis in der jeweils gültigen Fassung beachtet habe.

Karlsruhe, den 05.01.2024

Table of Contents

Kurzfassung .... **ii**

Abstract .... **iv**

Preface .... **vi**

Affidavit .... **vii**

Table of Contents .... **ix**

List of Figures .... **xi**

List of Tables .... **xxi**

List of Abbreviations .... **xxiii**

1 General Introduction **1**

- 1.1 Application of Miniaturization in Research 1
  - 1.1.1 Miniaturization of Standard Chemical Procedures 1
  - 1.1.2 Integrated Synthesis and Screening Platforms 4
- 1.2 The Droplet Microarray as a High-Throughput Platform 5
  - 1.2.1 Description of Surface Wettability 5
  - 1.2.2 Surface Chemistry of the Droplet Microarray 7
  - 1.2.3 The Droplet Microarray as Biological Screening Platform 10
- 1.3 Miniaturized Chemical Synthesis on the Droplet Microarray 12

2 Results and Discussion **19**

- 2.1 High-Throughput Synthesis of Photodegradable Hydrogels 19
  - 2.1.1 Introduction 19
  - 2.1.2 Protocol Optimization 22
  - 2.1.3 Screening Procedure 29
  - 2.1.4 Validation and Proof-of-Concept Application 32
  - 2.1.5 Bayesian Optimization 34
  - 2.1.6 Summary 36
- 2.2 Cascade-Synthesis and Screening of MEK-Inhibitors on DMA 37

2.2.1 Introduction 37
2.2.2 Characterization of Surface Loading, Purity and Yield 42
2.2.3 Reaction Conformation through MALDI-TOF-MS 48
2.2.4 Optimization of Cell Culture 52
2.2.5 Biological Screening 55
2.2.6 Summary 62
2.3 High-Throughput Miniaturized Synthesis of PROTAC-like Molecules 64
2.3.1 Introduction and Motivation 64
2.3.2 Chemical Characterization 67
2.3.3 Biological Screening 72
2.3.4 Summary 74

3 Conclusion 77

4 Materials and Methods 81

5 References 97

6 Appendix 102

7 Acknowledgments 118

List of Figures

Figure 1: Schematic depiction of how the contact angle (θ)is defined as the angle between the liquid-solid- and the gas-liquid interfaces (left) and a representative image of a water droplet on a hydrophobic surface (right). 6

Figure 2: Schematic depiction of the surface modifications during the manufacturing steps of a HEMA-*co*-EDMA DMA. 8

Figure 3: Synthetic scheme for the synthesis of surface dendrons from the vinyl-functionalized surface to generation 1.5 (G1.5). R represents the silane-bond to the glass substrate. The dendrons are constructed by alternating the thiol-ene reaction between surface-bound alkenes and 1-thioglycerol with a STEGLICH-esterification using 4-pentenoic acid with Diisopropylcarbodiimide (DIC) and 4-Dimethylaminopyridine (4-DMAP) as coupling reagent and catalyst, respectively. 9

Figure 4: Mechanism behind the synthesis of lipid-like molecules through a combination of thiolactone-ring opening and disulfide-exchange. The driving force of the mechanism is the formation of the pyridine-2(1*H*)thione that prevents the reverse reaction. 12

Figure 5: Mechanism behind the Norrish type 2 cleavage reaction of the photolabile linker employed for solid-phase synthesis on DMA. R1 indicates the bond to the target molecule, R2 represents the surface of the DMA.[49] 14

Figure 6: One possible reaction pathway for the formation of bisimide products during *Ugi* four component reaction. All reaction steps are reversible until the *Mumm* rearrangement that yields the bisimide as final product.[53] 15

Figure 7: Catalytic cycle for the SUZUKI-cross coupling 16

Figure 8: Schematic depiction of the different reaction steps involved in the free radical polymerization of methacrylates. 17

Figure 9: Structure of four different photoresponsive groups employing different mechanisms for their photoresponse and their respective wavelengths of light used to initiate the response.[79-84] 20

Figure 10: Schematic depiction of an experimental workflow for the nanoliter-scale preparation and analysis of photodegradable hydrogels on DMA: (i) Dispensing solutions of initiator, monomers and crosslinkers, (ii) photopolymerization through UVA-light, (iii) fluorescence staining with Rhodamine 6G, (iv) cycles of UVC irradiation and fluorescence microscopy to monitor the photodegradation. The figure was adapted from SEIFERMANN *et al.*[1] 22

Figure 11: Reaction equation for the radical polymerization of crosslinked soft materials from methacrylic monomers. X resembles residual groups of the initiating or terminating species. 23

Figure 12: (A) Ratio of hydrogel area after 1 min of UVC irradiation (a) to the area of the same composition without UVC irradiation (a_0) for 4 different ratios of PEGMA to SAMA and under two different polymerization conditions. Fluorescence microscopy images of the 4 different compositions polymerized for 30 min at 5.41 mW/cm2 stained (B) directly after polymerization or (C) after 1 min of additional UVC irradiation. Figure adapted from SEIFERMANN *et al.*[1] 24

Figure 13: Measured fluorescence area of a series of different hydrogel pads consisting of poly(ethylene glycol) methacrylate (Mw=500 Da) (PEGMA) and [2-(methacryloyloxy)-ethyl]dimethyl-(3-sulfopropyl) ammonium hydroxide(SAMA) with different PEGMA:SAMA ratios and different amounts of poly(ethylene glycol) dimethacrylate (Mw=750 Da) (PEGDMA) as crosslinker through the course of 20 min irradiation with UVC light. After swelling in Rhodamine 6G overnight, the gels were irradiated with UVC light (11.5 mWcm−2, 200–280 nm) and measured by fluorescence microscopy successively. Values were acquired by continuous measurements on the same slide. Error bars show the standard deviation between 10 replicates each. Figure adapted from SEIFERMANN *et al.*[1] 25

Figure 14: (A) Evaluation of gel stability under the influence of rhodamine 6G as a possible photosensitizer, to make sure the staining does not induce degradability. Nondegrading hydrogels made from poly(ethylene glycol) acrylate (Mw=480 Da) and different amounts (in mol%) of poly(ethylene glycol) diacrylate (Mw=700 Da) were irradiated for 10 min after incubation with rhodamine 6G overnight and afterward the change in fluorescence area was compared to check for degradation. Error bars are the standard deviation between 24 replicates. (B) Fluorescence microscopy images of nondegradable hydrogels on 1 mm spots stained with rhodamine 6G before and after UVC irradiation. Figure adapted from SEIFERMANN et al[1] 27

Figure 15: The two extreme degradation modes possibly occurring when irradiating the nanoliter sized hydrogels. Upon irradiation the gels can undergo symmetric degradation, thereby reducing the gel pads size in all directions comparably which leads to reduced fluorescence area as well as intensity (Isotropic degradation). Alternatively, the gels can degrade anisotropically along with the angle of incidence of the UV irradiation, reducing the overall fluorescence intensity without significantly reducing the fluorescence area (Top-Down degradation). This can lead to differences in the degradation curves measured from fluorescence intensity and from fluorescence area. Figure created with Biorender.com. 28

Figure 16: Fluorescence Area and integrated intensity throughout the course of irradiation for two different types of hydrogels in three independent experiments (blue, red, black) with 6 replicates each. (A) mono(2-acryloyloxyethyl) succinate crosslinked with 9.5 mol% glycerol dimethacrylate, (B) α-methylene-γ- butyrolactone crosslinked with 7.5 mol% glycerol dimethacrylate. Error bars show the standard deviation of six replicates. Figure adapted from *Seifermann* et al[1] 29

Figure 17: The course of degradation for two different sets of nanoliter sized hydrogel pads throughout UVC irradiation. Each row shows the 6 repetitions for each hydrogel after the given irradiation time together with their relative position on the slide (white number, Row/Column). The graphs show the relative fluorescence area and integrated fluorescence area of each repetition over the course of 20 min UVC irradiation. Given values are the mean value of the individual spots values (I) normalized to the starting value of the respective spot (I_0). Error bars are the standard deviation between the 6 replicates. Hydrogels consist of (A) 2-Hydroxyethyl Methacrylate, crosslinked with 8.5 mol% 1,4-Butandiol Diacrylate and (B) 2-Hydroxy-3-phenoxypropyl Acrylate crosslinked with 6.5 mol% *N,N*-Methylenebiscralyamide. Figure adapted from SEIFERMANN *et al.*[1] 30

Figure 18: Predictions of a multi-task Gaussian process regressor trained on a 7-fold split of the data. The colors indicate each fold. Figure adapted from SEIFERMANN *et al.*[1] 31

Figure 19: Degradation curves measured from fluorescence area on nanoliter scale, fluorescence intensity on nanoliter scale and mass loss on microliter scale, together with their respective exponential fits. Four types of hydrogels were investigated: (A) mono-2-

(methacryloyloxy)ethyl phthalate, crosslinked with 6.5 mol% poly(propylene glycol) dimethacrylate, (B) poly(ethylene glycol) methyl ether methacrylate, crosslinked with 6.5 mol% glycerol dimethacrylate, (C) 4-hydroxybutyl acrylate, crosslinked with 7.5 mol% trimethylolpropane ethoxylate methyl ether diacrylate, and (D) N-(2-acryloyloxyethyl)-N-benzyl-N,N-dimethylammonium chloride, crosslinked with 7.5 mol% trimethylolpropane ethoxylate methyl ether diacrylate. Fluorescence area and integrated intensity are measured from six different 130 nL sized hydrogel pads on DMA, mass loss was measured from three 150 µL sized hydrogel pads polymerized in a PTFE mold. Values in the graphs are the average of the individual repetition's values normalized to the respective repetition value at 0 s irradiation. Error bars show the standard deviation of all replicates. Adapted from SEIFERMANN *et al.*[1] 33

Figure 20: Encoded pattern on an array of nanoliter hydrogels, created from three different hydrogel types: Non-Degradable hydrogel based on 4-Hydroxybutyl acrylate and N,N-Methylenbisacrylamide, a slowly degradable hydrogel made of Furfuryl Methacrylate and Pentaerythritol triacrylate and a rapidly degradable hydrogel consisting of Poly(ethylene glycol)methyl ether acrylate (Mw = 500) and Glycerol Dimethacrylat. Images have been edited with Adobe Photoshop Lightroom Classic to increase Contrast for better visualization. (B) According degradation curves of the non-degradable composition, slowly degrading hydrogels and the rapidly degrading hydrogels. Values shown are measured in a miniaturized screening process and calculated as average of 6 repetitions normalized to their respective starting value. Error bars shown represent the standard deviation between these six repetitions. Adapted from SEIFERMANN *et al.*[1] 34

Figure 21: Distribution of all the different hydrogel properties (intensity/size) versus the degradation lifetime before and after Bayesian optimization. (A) 2D histogram of the square root of the initial measured average intensity or initial size (C) versus the fitted log-lifetime of the hydrogel under UV-irradiation. The 2D histogram after Bayesian optimization of the square root of the initial measured average intensity (B) or initial size (D) versus the fitted log-lifetime of the hydrogel. Brighter colors represent higher density indicated by a colorbar legend. On the left, the distributions of the initial, randomly selected hydrogels are shown. On the right, the distribution of experimentally measured suggestions from Bayesian optimization (both multiobjective and extremal property search) are shown (with the initial distributions in the background). Red circles in B and D highlight areas of high lifetime and intensity with multiple compositions. Adapted from SEIFERMANN *et al.*[1] 35

Figure 22: Schematic depiction of the ERK-signaling cascade starting from activation of RAS through EGFR, followed by subsequent phosphorylation of RAF, MEK and ERK, leading to an effect on the transcription. Figure was created with Biorender.com. 38

Figure 23: Chemical structures of the three FDA approved inhibitors SELUMETINIB, BINIMETINIB and COBIMITINIB as well as the structure of designated orphan drug MIRDAMETINIB. Red indicates the binding region for the hydrophobic pocket of MEK, blue shows the part binding the K97-residue.[119, 120] 40

Figure 24: Synthetic route for the preparation of novel MEK-inhibitors through solid-phase using a combination of amidation and SUZUKI-coupling... 41

Figure 25: Preparation of intermediate 1 and final compound 2 through solid-phase synthesis on DMA: (i) 3,4-difluoro-2-(2-fluoro-4-

iodophenylamino)benzoic acid (4), HOBT, DIC in NMP, 18 h; (ii) Sodium tetrachloropalladate, dibenzyl-N,N-diisopropylphosphoramidite, phenylboronic acid, sodium carbonate in NMP/Water, 18 h; (iii) UV irradiation, 40 min. 42

Figure 26: LC-MS chromatograms of intermediate 1 (left) and product 2 (right), obtained after solid-phase synthesis. The peak for the corresponding product is marked with a red star. 43

Figure 27: Surface attachment of Fmoc-alanine and release of Fmoc-alanine amide (3) for the calculation of the amino acid loading: (i) Fmoc-alanine (100 mM), DIC, HOBT in NMP, 18 h; (ii) UV irradiation, 7-42 min. 43

Figure 28: (A) Released amount of Fmoc-alanine amide (3) from a surface modified with Fmoc-alanine (100 mM) with respect to the irradiation time. (B) Purity of amidation product between 3,4-difluoro-2-(2-fluoro-4-iodophenylamino)benzoic acid (4) and eight different amino acids immobilized on the hydrophilic surface of a DMA after UV-induced cleavage. Purity was calculated *via* LC-MS as integration value of the product peak divided by the sum of all peak integration values. Measurements were performed in triplicates, error bars show the standard deviation. 44

Figure 29: Preparation of standard compounds 1 and 2 in flask: (i) Alanine amide hydrochloride, *N*-ethyl-*N'*-3-dimethylaminopropyl carbodiimide, *N*-Methylmorpholine, HOBT in DMSO, 16 h at rt; (ii) Phenyl boronic acid, palladium acetate, triphenylphosphine, sodium carbonate in THF/Water, 16 h at 80 °C. 45

Figure 30: Surface loading of 1 and theoretical assay concentration of 2 depending on the concentration of the photolinker modification solution. Error bars show the standard deviation of three independent experiments. 48

Figure 31: Exemplary MALDI-mass spectra recorded on a ground steel target plate and respective structures for two compounds synthesized on 1.4 mm spots of a DMA. 49

Figure 32: MALDI-MS imaging of an ITO-DMA modified with 900 µm spots in which solid-phase synthesis was carried out. Colors indicate the intensity of the [M-H]- ion for 7 different chemical formulas. Target structures with the color of their [M-H]- peak are given. 50

Figure 33: One Example of the five recorded MS/MS fragmentation spectra. The target compound's structure is given in the spectrum, the numbers in the spectrum reflect the respective fragments. Their exact mass and structure are given in the table on the right........ 52

Figure 34: Cell mediated reduction of the tetrazolium salt in cell counting kit-8 to the colored formazan dye through NADH/NADPH dehydrogenation. 53

Figure 35: (A) Scanning image of a DMA modified with different amounts of photolinkers after culture of HT-29 cells for 72 and CCK8 assay. The layout was randomized. (B) Color Intensity of HT-29 cells seeded onto the hydrophilic spots of a DMA, modified with oxidized photolinker surface-groups in a CCK8 assay. A linear increase can be observed in the beginning, reaching a plateau at around 300 cells per spot. Error bars show the standard deviation of 6 replicates randomly placed over the whole slide................ 54

Figure 36: (A) Brightfield microscopy images of HT-29 cells seeded with the same density on a DMA modified with oxidized photolinker surface groups after incubation for 72 h with *Mirdametinib* (+) or without addition of an inhibitor (-). (B) Boxplot of the number of PI-positive HT-29 cells per spot seeded on a DMA modified with oxidized photolinker surface groups after incubation for 72 h with *Mirdametinib* (+) or without addition of an inhibitor (-). Each experiment contains the information of 120 replicates.............. 55

Figure 37: Absolute number of dead cells per spot for the primary screening of 300 different MEK-Inhibitors tested on DMA against HT-29 human colon cancer cells. Values are the average of three replicates, error bars show the standard deviation...................... 58

Figure 38: Normalized Cell Death of 325 compounds as ratio of reduced average dead cells per sample spot to reduced average dead cells per positive control spot on DMA. Values are average values of three replicates, error bars show the standard deviation. 59

Figure 39: Normalized Cell Death of 75 different compounds as ratio of reduced average dead cells per sample spot to reduced average dead cells per positive control spot on DMA for two independent experiments (screening and reproduction). A clear increase is observed for the groups containing A2 (Compound 26-50) and A3 (Compound 51-75) while no increase is visible for compounds containing A1 (Compound 1-25). The value for the individual compounds, however, shows moderate to high relative deviation between the two experiments. Values are average values of three replicates, error bars show the standard deviation. Red stars indicate the compounds chosen for the first dose-response measurements. 60

Figure 40: The four selected compounds for the validation measurement......... 60

Figure 41: Results of the dose-response measurements of HT-29 human colon cancer cells against 4 different compounds. Experiments were conducted using 384 well plates, cells were seeded at 5000 cells per well and incubated with the different compounds 72 h prior to analysis using a CELL TITER-GLO® luminescence assay. Values are the average of three replicates, error bars show the standard deviation. 61

Figure 42: Schematic depiction of the catalytic cycle by which PROTACs induce target protein degradation through ubiquitin transfer and the proteasome. Figure was created with Biorender.com. 65

Figure 43: Reaction Scheme for the preparation and release of PROTAC-like molecules on the DMA *via Ugi*4CR. Example structures for all reagents as well as a possible product are given. The figure was adapted from TIAN *et al.*[2] 67

Figure 44: Synthetic route for the preparation of aldehydes containing a thalidomide warhead and various aliphatic linkers for the UGI reaction: (i) PCC, DCM, N_2, 3h at rt; (ii). AcONa, AcOH, 12 h at 110°C; (iii). KI, KHCO3, DMF, 12 h at 60°C. The figure was adapted from TIAN *et al.*[2] 67

Figure 45: Model reaction for the characterization of product loading and release kinetics of the solid-phase UGI-reaction on DMA: (i) Acid 14, Aldehyde 15, Isocyanide 16 on DMA in ethylene glycol/γ-butyrolactone (1:9, v/v), 18 h at rt; (ii) UV-irradiation............... 68

Figure 46: Released amount of compound 17 after solid-phase UGI-reaction on DMA with three different final reagent concentrations (10, 20, 50 mM). Values are calculated based on a calibration done with compound 18 as standard. Error bars show the standard deviation of three independent repetitions. The figure was adapted from TIAN *et al.*[2] 69

Figure 47: Results of a primary screening of randomly selected 22 PROTAC-like molecules against HT-29 colon cancer cells. Each graph represents an independent experiment with the average number of PI-positive cells versus the compound identifier. Error bars show the standard deviation of 10 replicates. The figure was adapted from TIAN *et al.*[2] 74

List of Tables

Table 1: Conversion rates and purity of the final products obtained by the reaction sequence involving 8 different amino acids and 2 different boronic acids. Purity is calculated as ratio of the product peak integral to the total integration value of all peaks. Conversion rate is calculated as ratio of the product peak integral to the sum of product peak integral and starting material peak integral. 46

Table 2: Identification rate of final products in MALDI-TOF-MS regarding each tested building block for measurements on ground steel target plate (MTP) and ITO-DMA, respectively. 51

Table 3: Identifiers of all possible MEK-inhibitor molecules with the respective amino acid (A) and boronic acid (B) used for the preparation of the compound on DMA. 57

Table 4: Identification rate of different PROTAC-like molecules as product of solid-phase synthesis on DMA, regarding each component of UGI reaction. The figure was adapted from TIAN *et al.*[2] 70

Table 5: Purity of selected PROTAC-like molecules 1-25, prepared on 2.8 mm spots of a DMA modified with 20 mM photolinker solution. The figure was adapted from TIAN *et al.*[2]........ 71

Table 6: Building blocks used in the preparation of 22 different PROTAC-like molecules for a primary screening against HT-29 human colon cancer cells. 73

List of Abbreviations

°C	Degree Celsius
µM	10^{-6} Mol/L
AC	Acid
ACN	Acetonitrile
AH	Aldehyde
CCK8	Cell Counting Kit 8
DHB	2,5-Dihydroxybenzoic Acid
DI	Deionized
DIC	*N*,*N*‘-diisopropyl carbodiimide
DMA	Droplet Microarray
DMEM	Dulbecco’s Modified Eagle Medium
DMF	*N*,*N*-Dimethylformamide
DMSO	Dimethyl sulfoxide
EDC·HCl	*N*-(3-Dimethylaminopropyl)-*N’*-ethylcarbodiimide hydrochloride
EDMA	Ethylendimethacrylate
ESI	Electrospray Ionization
Fmoc	Fluorenylmethylcarbonyl
HEMA	2-hydroxyethylmethacrylate
HOBT	Hydroxybenzotriazole
HT	High Throughput
IC	Isocyanide
ITO	Indium Tin Oxide
LAP	Lithium phenyl-2,4,6-trimethylbenzoylphosphinate
LC-MS	Liquid chromatography coupled mass spectrometry
M	Mol/L

MALDI	Matrix assisted laser desorption ionization
MEK	Mitogen-activated protein kinase kinase
mM	10^{-3} Mol/L
MS	Mass spectrometry
MSI	Mass spectrometry imaging
NMP	*N*-methyl-2-pyrrolidon
NMR	Nuclear magnetic resonance spectroscopy
P/S	Penicillin-Streptomycin Mixture
PBS	Phosphate buffered saline
PDMS	Poly(dimethylsiloxane)
PEG	Poly(ethylene glycol)
PEGA	Poly(ethylene glycol)acrylate
PEGDA	Poly(ethylene glycol)diacrylate
PEGDMA	Poly(ethylene glycol)dimethacrylate
PEGMA	Poly(ethylene glycol)methacrylate
PI	Propidium iodide
PROTAC	Proteolysis-targeting chimera
PTFE	Poly(tetrafluorethene)
TOF	Time of flight
UV	Ultra violet
Vis	Visible

1 General Introduction

Due to the global accumulation of carbon dioxide over the recent years, society and industry are facing the challenge of reducing CO_2 emission. This has a severe impact on many factors of daily life but also on scientific research. There are many different approaches to this problem, some of the most prominent examples being CO_2-upcycling, CO_2-capture or the implementation of green chemistry methods.[3-5] While these research fields offer a perspective for an almost-zero or even a negative CO_2-balance, their broad application is still not fully possible in all fields of life or research yet. One concept that has developed from pharmaceutical and medical research that offers to at least reduce the material consumption compared to standard workflows is miniaturization. While the driving force behind miniaturization is mostly not just sustainability but also the cost aspect, the reduced amount of chemicals or resources have an innate advantage when looking at the CO_2 emission of individual experiments. Additionally, miniaturization is often combined with parallelization to achieve not only a cost- and emission efficient process, but to facilitate an increased scientific progress not achievable in individual experiments.

1.1 Application of Miniaturization in Research

1.1.1 Miniaturization of Standard Chemical Procedures

One of the biggest challenges researchers are facing when applying miniaturized methods is the forced deviation from the classical protocols. Standard procedures such as simple chemical synthesis or cell cultures become more challenging and less predictable when the volume in which it is conducted is reduced. Classical analysis methods that are otherwise widely applied become inaccessible due to insufficient sensitivity. Loss of sample during transfer steps, which can be deemed irrelevant on a gram scale, is now a significant portion of the whole sample, thereby reducing the sensitivity even further. Due to this, miniaturization required a different set of synthetic strategies, purification techniques, analytics, and handling steps.

For chemical synthesis one of the most elegant ways to avoid a majority of the problems mentioned above is the use of solid-phase synthesis (SPS) strategies. In these, the desired compounds are synthesized using a linker that is attached on a solid anchor. The linker part possesses a reactive sight that can be utilized to construct the molecules in a single reaction or in a reaction cascade. Reagents are typically applied in excess to compensate for the poor kinetics of reactions on interfaces and the remaining starting materials, reagents and side products can be easily removed together with the solvent once the reaction is completed after which the linker is cleaved, and the target compound is released. This yields comparably high purities without the use of further purification steps, but often requires careful planning to avoid side reactions that include the linker unit. As solid support serve usually beads of porous polymer or crystalline porous glass.[6, 7]

A common approach for the creation of compound libraries using SPS is the so-called “split and pool” method. Here, a set of beads is separated into groups and each group is modified with a distinct building block. Afterwards they are pooled together and separated into different groups again, each containing different beads modified with the different building blocks of the first step. These groups are then subverted to a second reaction step where each group is again modified with a distinct building block, thereby increasing the number of compounds to $n_1 \cdot n_2$, where n_i is the number of building blocks in reaction step i. This means, if the same reaction with the same building blocks is repeated over and over, the number of compounds achievable grows exponentially with the number of reaction cycles, while the number of steps grows linear. This makes it a highly efficient process for the creation of combinatorial libraries. Since the yield of the reaction sequence and therefore the purity of the final compound, is also exponentially related to the number of steps, sufficient purity requires a high conversion rate in every reaction step. Ideally, the beads modified through this method each contain only one compound, which is why these libraries are called one bead one compound (OBOC) libraries.[8] Their application ranges widely and it is very popular for the synthesis of compounds resembling naturally occurring structures such as peptides or carbohydrates.[9-11]

In contrast, there is a lot of research dedicated to increasing the performance of chemistry in solution on nanoscale. A major issue here is the restriction in terms of solvents that can be applied. Most processes, such as cross-couplings, have been optimized with respect to solvent systems to yield good to excellent conversion rates on a gram scale. However, the restrictions of miniaturization often do not allow the use of these optimized solvent systems. Due to the low volumes applied, evaporation proceeds very fast, which is why only high boiling point solvents can be applied if the concentration of the reagents is to be maintained. Additionally, high-throughput experimentation often relies on the use of liquid handlers or dispenser, which comes with additional requirements to the solvents such as low viscosity. This means in turn, that all the previously reported reaction conditions need to be reoptimized to compatible solvents. GESMUNDO *et al.* recently reported a study opting to do exactly this, optimizing reaction conditions for the most commonly used reactions in medicinal chemistry such as SUZUKI-coupling, HARTWIG-BUCHWALD-coupling or reductive amination in commonly applied solvents for miniaturized chemistry such as DMSO to translate them to high-throughput experimentation.[12]

SANTANILLA *et al.* showed an inverted approach, optimizing the reaction conditions for substrates that show poor conversion on large scale on a nanomolar scale in a 1536 well plate. In this, they applied a set of 96 different reaction conditions with 16 different catalysts and five bases to optimize the Hartwig-Buchwald coupling of eight electrophiles with 12 nucleophiles. The reaction conditions were then translated back to micromole scale and showed good to excellent yields, showcasing the potential of high-throughput experimentation.[13]

DÖMLING and coworkers showed a combinatorial approach for the preparation of libraries containing indole-derivatives as a biologically interesting core structure on nanomolar scale. Using an acoustic droplet ejector and a 384 well plate, they combined an interrupted Fischer indole synthesis with UGI-3 component reactions to synthesize 192 differently substituted indolines. The analysis of all these components was carried out using supercritical fluid chromatography (SCF) coupled with mass spectrometry and consumed only around 4 mg of starting materials.[14]

In general, with the establishment of adapted reaction protocols, new solvent systems, as well as the development of better high-throughput analytics such as high performance liquid chromatography (HPLC), ultra-high performance liquid chromatography, supercritical fluid chromatography (SFC), and matrix assisted laser desorption ionization mass spectrometry (MALDI-MS), high-throughput chemistry is advancing fast and is steadily losing more and more of its former limitations.[15-18]

1.1.2 Integrated Synthesis and Screening Platforms

As a means to an end, chemical reactions are only as useful as the goal of what they are applied for. Due to this, the application of miniaturized chemistry is an important question. Since the beginning of high-throughput experimentation, the majority of the platforms was designed for biological experiments such as drug screenings.[19] Therefore, the obvious choice for the application of miniaturized chemistry is in the combination with already existing biological procedures in the same format, thereby creating a platform that allows the preparation and purification of compounds, directly followed by the biological evaluation of their key parameters. The combination of different miniaturized processes without format changes is summarized under the term “integration” and is of utter importance to efficiently connect different fields of high-throughput (HT) experimentation.

AGNEW *et al.* used a split-and-mix approach to achieve this and created OBOC libraries of modified polypeptides to identify potent antibody-like alternative to real antibodies. They prepared their compounds on the solid phase *via* CuAAC of modified random sequence oligopeptides. The immobilized compounds were then directly tested on-bead for their binding affinity. For this, a biotinylated version of the target protein was added, the excess was removed and the biotinylation was selectively stained with a fluorophore and evaluated through fluorescence microscopy [20]

Utilizing the same chemical reaction, GEHRTZ *et al.* synthesized libraries of small-molecule MMK7 inhibitors through CuAAC on a nanoscale using an acoustic dispenser.[21] The reaction mixtures were used for an in-cell western assay to directly test the potency of the inhibitor derivatives and could identify hits with up to twentyfold increase in activity compared to their control. However, for the assay only a small part of the sample was transferred and diluted, increasing the material consumption drastically compared to fully integrated systems.

SUTANTO *et al.* combined HT synthesis with HT X-ray crystallography to identify novel inhibitors for the protease 3CLpro. They applied multicomponent reactions such as the UGI- or PASSERINI-reaction to create libraries of acrylamides in 96- or 384-well plates in volumes of 500 and 10 µL, respectively.[22] They were able to identify single-digit micromolar binders, showcasing the advantages of HT experimentation in primary screenings.

Other possible approaches to achieve integration are usually modular reaction and analysis stations connected through liquid handlers or microfluidic devices within a closed environment.[23] The use of microfluidic devices generally allows for a more efficient sample transport between different reaction vessels and therefore a more efficient miniaturization.[24] However, the transport of sample is always accompanied with at least a minimal loss, reducing the efficiency and increasing the risk of cross contamination compared to transportless platforms.

1.2 The Droplet Microarray as a High-Throughput Platform

1.2.1 Description of Surface Wettability

A feature of surfaces that has gained and maintained its popularity over the last years in research and material design is the surface wettability. Wettability describes the spreading behavior of a liquid on a surface, how strong does it attach and how much contact area does it maintain. The simplest way to describe wettability is the so-called contact angle θ, the angle that is formed between the liquid-solid and the air-liquid interfaces (Figure 1).[25] If the liquid is water, the surface can be described as hydrophilic ($\theta < 65°$), hydrophobic (θ > 65°), superhydrophilic (θ < 10°) or superhydrophobic (θ > 150°, contact angle hysteresis < 10°).

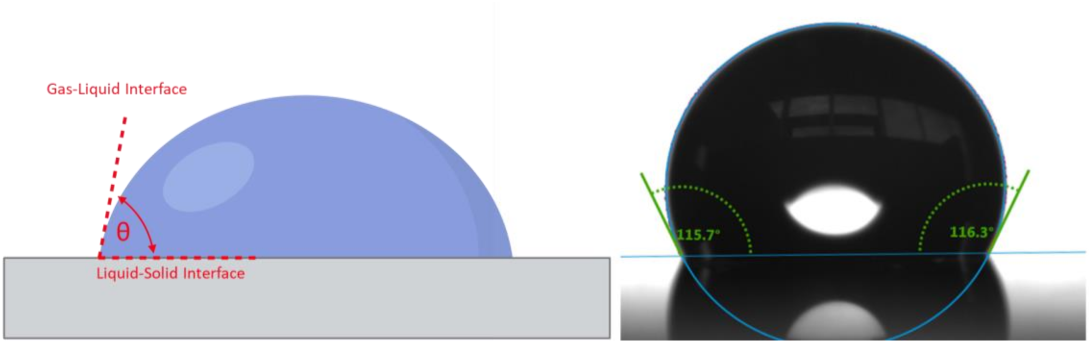

Figure 1: Schematic depiction of how the contact angle (θ)is defined as the angle between the liquid-solid- and the gas-liquid interfaces (left) and a representative image of a water droplet on a hydrophobic surface (right).

The wetting behavior is governed by a variety of factors such as the energy for the three different interfaces liquid-vapor (γ_{lv}), liquid-solid- (γ_{lS}) and solid-vapor (γ_{sv}) and was firstly described in a mathematical equation by T. Young in 1805 for an ideal flat surface:[26]

$$\cos(\theta) = \frac{\gamma_{sv} - \gamma_{ls}}{\gamma_{lv}}$$

As real surfaces are rarely perfectly smooth, additional descriptions including the surface roughness needed to be developed. Here two distinct wetting states were to be differentiated, the so called Cassie-Baxter and the Wenzel states, named after A. Cassie, S. Baxter and R. Wenzel who described the respective wetting states mathematically.[27] In the case of Wenzel wetting, the cavities of a rough surface are fully penetrated by the wetting liquid leading to a homogeneous interface that can be described as

$$\cos\,(\theta') = \cos\,(\theta) * r$$

with the corrected contact angle θ' and the surface roughness r.[28] In the case of Cassie-Baxter wetting, there are gas inclusions between the surface cavities and the wetting liquid, reducing the effective liquid-solid interface. With ϕ_s as the fraction of the solid-liquid interface of the whole interfacial area, this leads to the following description:[29]

$$\cos(\theta') = \phi_s * [\cos(\theta) + 1] - 1$$

Both these equations indicate a severe impact on the wettability not only through the interfacial energy, but through the microstructure of the surface. This can be observed in nature on the highly hydrophobic leaves of the lotus flower. The microstructured leaves create a rough substrate and the covering hydrophobic wax creates a poor liquid-solid interaction, leading to a superhydrophobic surface, which in turn allows for self-cleaning properties known as lotus effect.[30] This discovery led to the formation of many bioinspired microstructured materials through means such as electro deposition, electro spraying or laser texturing to achieve antifouling, self-cleaning or anti-corrosive properties.[31-33]

A different application for this was shown by JOKINEN *et al.* in 2008. They combined polymer deposition and plasma lithography on a nanostructured silicon wafer to create confined superhydrophobic and superhydrophilic areas next to each other. In this study, they demonstrated that a high difference in static contact angles between two defined parts of a surface area can be used to confine a droplet.[34]

GEYER *et al.* used this effect for the creation of a microarray that became the predecessor of the droplet microarray (DMA).[35] The idea was to overcome classical limitations of microtiter plates caused by the walls, such as high adsorption and capillary effects, that get more and more problematic the smaller the wells become, while maintaining the benefits of an array format. For this, they modified a glass substrate with a thin film of a porous copolymer consisting of 2-hydroxyethyl methacrylate (HEMA) and ethylene dimethacrylate (EDMA) to create a superhydrophilic surface. By use of photolithography in a grafting-from approach, they polymerized a superhydrophobic copolymer consisting of 2,2,3,3,3-pentafluoropropyl methacrylate (PFPMA) and onto the hydrophilic polymer to create hydrophobic borders without changing the surface morphology.

1.2.2 Surface Chemistry of the Droplet Microarray

From this starting point, the DMA developed as an array of hydrophilic spots on a superhydrophobic background. While there are different types of DMAs with varying surface properties and manufacturing procedures, they all share some common attributes.

They are prepared from microscopy glass slides that are modified to exhibit either a high density of surface functional groups, a high roughness, or both. The creation of the hydrophilic and superhydrophobic areas happens in the final step of the preparation process through UV-induced radical addition of hydrophilic thiols such as 2-mercaptoethanol and cysteamine or hydrophobic thiols such as 1H,1H,2H,2H-perfluorodecanthiol (PFDT) to C-C-double- or triple-bonds present on the surface. Due to the use of photolithography and the accompanying high resolution and precision, the density of confined experimental vessels creatable is enormous and can go up to 2187 vessels on a 75 x 25 mm^2 glass slide.[36]

The first reported DMA was, as a direct successor of the grafting-from approach, also based on porous HEMA-*co*-EDMA polymers. FENG *et al.* modified the surface hydroxy-groups of the polymer with pentynoic acid in an esterification reaction to convert the terminal groups into alkynes. These alkynes were then reacted with hydrophilic and hydrophobic thiols in a thiol-yne reaction to yield the patterned substrate (Figure 2).[37] This yields surfaces with static water contact angles θ_{St} of 169° and 4.4° for the superhydrophobic and superhydrophilic regions, respectively.

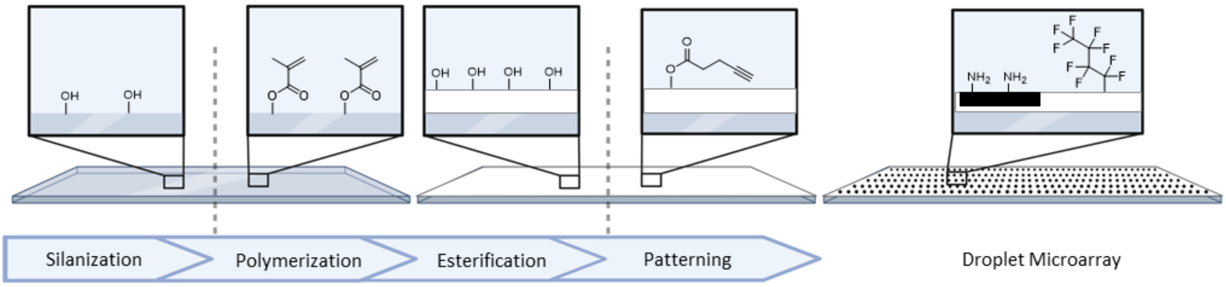

Figure 2: Schematic depiction of the surface modifications during the manufacturing steps of a HEMA-*co*-EDMA DMA.

These arrays confine both aqueous and organic solvents well and exhibit a high density of functional groups that are especially useful for further surface functionalization or solid-phase synthesis. Major drawbacks of this type of DMA were the inhomogeneous polymer surface and the strong adsorption of molecules to the highly polar polymer surface in the hydrophilic spots, which were especially detrimental for purely biological applications.

To overcome those limitations, the Z-Slide was developed, a DMA where the roughness was introduced through a coating with silica nanoparticles. The nanoparticles are prefunctionalized with trimethoxyvinylsilane in a polycondensation reaction and then spincoated onto the glass surface. The vinyl-groups can then be used for UV-induced thiol-ene reaction to attach different thiols and create superhydrophobic and hydrophilic areas. This creates a surface that highly stabilizes aqueous droplets with a reduced adsorption compared to the polymer, but the stabilization of organic liquids is drastically reduced.[38] Additionally, due to the limited degree of covalent attachment of the silanized nanoparticles to the glass surface, the coating layer exhibits poor mechanical stability.

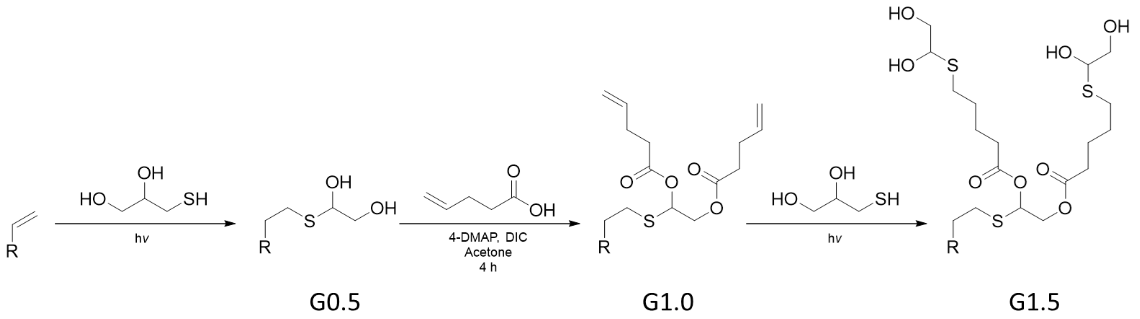

Figure 3: Synthetic scheme for the synthesis of surface dendrons from the vinyl-functionalized surface to generation 1.5 (G1.5). R represents the silane-bond to the glass substrate. The dendrons are constructed by alternating the thiol-ene reaction between surface-bound alkenes and 1-thioglycerol with a Steglich-esterification using 4-pentenoic acid with Diisopropylcarbodiimide (DIC) and 4-Dimethylaminopyridine (4-DMAP) as coupling reagent and catalyst, respectively.

In order to improve the mechanical stability, a fully covalent modification of the surface was developed based on dendritic growth.[39] Here, the surface of the glass substrate is modified with a vinyl-silane layer by chemical vapor deposition. This layer serves as anchor point for the construction of surface-dendrons. For this, a combination of previously employed chemical reactions is applied, being surface esterification and thiol-ene click reactions. The vinyl-surface is converted into a glycol by UV-induced reaction with thioglycerol to form generation 0.5. This reaction step serves as introduction of the branching point. The hydroxy-groups are then converted to esters through *Steglich*-esterification using 4-pentenoic acid as reaction partner. This reintroduces the double bonds to form generation 1.[40] From here on, the reaction sequence is repeated to construct generation 3 surface-dendrons that are used for the hydrophilic-hydrophobic patterning with thioglycerol and PFDT as described before.

As this is a completely different approach without any type of coating, the major downside here is that the surface morphology is still resembling the one of the original glass slides which is very smooth. This low roughness leads to lower hydrophobicity (θ_{St} = 104.3°) and hydrophilicity (θ_{St} = 55.9°) of the respectively patterned areas and, therefore, to an overall lower confinement. While the confinement in general is worse, it makes up for this with its ability to at least partially confine organic liquids with low surface-tension such as acetonitrile, that are not usable on the other types of DMA. On top of that, the covalent modification means a high binding energy that cannot be overcome easily, thus rendering the slide able to withstand thorough cleaning procedures necessary for reuse.

1.2.3 The Droplet Microarray as Biological Screening Platform

By now, the DMA has been applied for a variety of biological methods that have been previously reserved for microtiter plates with volumes that were at least in the microliter range. Its ability to easily handle volumes in the double-digit nanoliter range reduces the material consumption and thereby expands the number of different experiments possible from a limited amount of starting material. This can be very beneficial for materials such as patient-derived cells, when the amount that can be taken without a significant risk for the patient is minute. *POPOVA et al.* have shown that the DMA is a viable alternative in this case by performing drug sensitivity and resistance testing of primary chronic lymphocytic leukemia. The required amounts for one single experiment here were only 100 cells, 0.03 nmol of compound and 50 nL of medium, thereby reducing the amount of material consumed compared to experiments in a 384-well plate by a factor of 200.[41]

In cancer research, a well-known problem is the difference between behavior in 2D cell cultures and tissue, organs, or tumors, making it difficult to translate all insights gained from 2D cell culture directly to a patient. 3D cell culture is an emerging tool to reduce those difficulties, providing more complex model systems and bridging the gap between 2D cell culture and animal models such as xenografts.[42] CUI *et al.* developed a method to apply 3D cell culture on DMA by creating spherical cell structures (spheroids). These spheroids are created using the “hanging droplet” method, in which the cell suspension is seeded onto the hydrophilic spots of the DMA and afterwards turned upside down. Gravity leads to sedimentation and the cells form spheroids.[43] Since the confinement of the droplets is only based on the positive interaction between the liquid and the hydrophilic spots and not on walls of any sort, the suspension will adhere to the surface without any additional measures and can be turned back around as soon as the spheroids are formed. By controlled merging of different liquid containing spots, multi-spheroidal architectures can be created to further enhance the model and its resemblance of actual tissue.[38]

LIU *et al.* showed the applicability of the DMA beyond cancer research and investigated the differentiation of human induced pluripotent stem cells (hiPSCs). For this, they developed a seeding and immunostaining workflow with an experimental volume of 200 nL to analyze the effect of recombinant human-derived proteins or protein mixtures coated onto the hydrophilic spots.[44] By quantifying the expression level of several pluripotency markers, they identified 10 different conditions that achieved better results than Matrigel. Two of these coatings were used to demonstrate long term culture of hiPSCs on the DMA and subsequent differentiation. Those promising results show good control over the differentiation of hiPSCs without the use of undefined, animal-derived materials and are therefore a promising advance in the direction of clinical application for hiPSCs.

Microbiological experiments are also possible on the DMA. LEI *et al.* have demonstrated a workflow to culture different types of bacteria on the hydrophilic spots of the DMA and used this to investigate the bacterial response to treatment with different drugs.[45] In their research, they treated carbapenem-resistant *Klebsiella pneumoniae* and methicillin-resistant *Staphylococcus aureus* with a library of 2000 different compounds to identify new types of antibiotics for the treatment of infections caused by resistant pathogens. By combining this with a colorimetric assay based on the metabolization of the tetrazolium dye in cell counting kit 8 they could achieve a simple and straightforward analysis pipeline that can readily be adjusted to various types of bacteria.

1.3 Miniaturized Chemical Synthesis on the Droplet Microarray

Besides the application of the DMA as a versatile platform for purely biological screening experiments, a key point of interest is the development of an integrated platform combining chemistry and biology. The research highlighted in the last chapter relies mostly on the addition of compounds that were prepared in a completely different setup to find new types of drugs or materials. However, to create a platform that utilizes the advantages of miniaturization fully, optimizing the chemistry to both be compatible with the miniaturized format and with biological assays is mandatory. BENZ *et al.* therefore developed the concept of ChemBIOS utilizing the dendrimer DMA (see chapter 1.2.2).[39] They highlighted the compatibility of the chip with chemical reactions in solution and their analysis using a one-pot synthesis of lipid-like structures through a multicomponent reaction. (Figure 4)

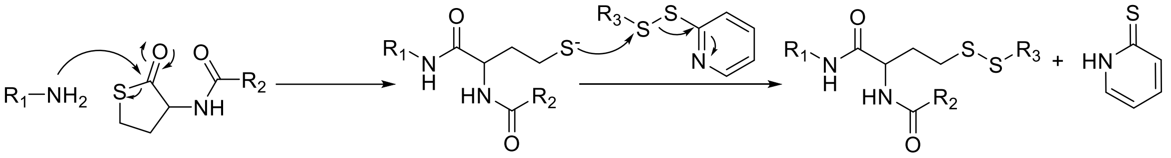

Figure 4: Mechanism behind the synthesis of lipid-like molecules through a combination of thiolactone-ring opening and disulfide-exchange. The driving force of the mechanism is the formation of the pyridine-2(1*H*)thione that prevents the reverse reaction.

The reaction process could be monitored through UV/Vis-spectroscopy and the product formation was confirmed through matrix assisted laser desorption ionization time of flight mass spectrometry (MALDI-TOF-MS). For this, the surface modification was applied to an indium tin oxide (ITO) coated glass slide as conductive substrate which allowed direct measurement from the DMA without sample transfer. To prove the general biocompatibility, it was demonstrated that the dendritic surface allows for the culture of both adherent and suspension cell lines with viabilities exceeding 97 % for three different cell lines. In a different report, they utilized the same platform and the same reaction scheme to prepare a library of lipidoids and screen them on-chip for their transfection efficiency.[46]

However, even though the surface is biocompatible, a major issue with miniaturized chemistry in solution is often the lack of purification techniques. As an approach to solve this problem, WIEDMANN *et al.* miniaturized the classical approach of liquid-liquid extraction (LLE) to be compatible with the microarray format.[47] In order to achieve this, the extractant droplet is dispensed onto the hydrophobic border between the sample spot and an empty neighboring spot. This way, the extractant gets in contact with both the sample containing liquid and the empty neighboring spot. At this point, the typical LLE approach requires mixing of the extractant with the sample solution to create an increased interfacial area for an increased extraction speed, a different driving force was required. By choosing 1-octanol as extractant, a solvent with lower vapor pressure than water, it was possible to evaporate the aqueous droplet to create a faster extraction process, thereby transferring the extracted compounds efficiently to the previously empty spot. They also showed pH-controlled separation of binary mixtures to showcase the selectivity of the method.

Even though LLE is a powerful tool to purify chemical compounds, chemical reactions often require more complex separation techniques, such as chromatography, to achieve sufficient purity for a reliable screening. To avoid complicated purification processes, a solid-phase synthesis approach was adapted to the DMA by ROSENFELD *et al.* in which they utilized the high density of surface-functionalities of the HEMA-*co*-EDMA DMA.[48] They modified the surface's amino groups of the hydrophilic spots with a photolabile linker as starting point for the solid-phase synthesis. The linker core motif is a *o*-nitrobenzylalcohol or -amine, the hydroxy- or aminogroup can be used for reversible attachment of starting materials to the solid phase. Once the synthesis is conducted, the linker can be irradiated with UV light (λ = 365 nm) which leads to a *Norrish* type 2 reaction that releases the product by cleavage of the C-X bond in the benzylic position (Figure 5).[49] The controlled release through light instead of reagents allows for increased purity of the released compounds as well as a precise control of the releaser compounds not only through the overall product loading, but also through the dosage of UV-irradiation applied.

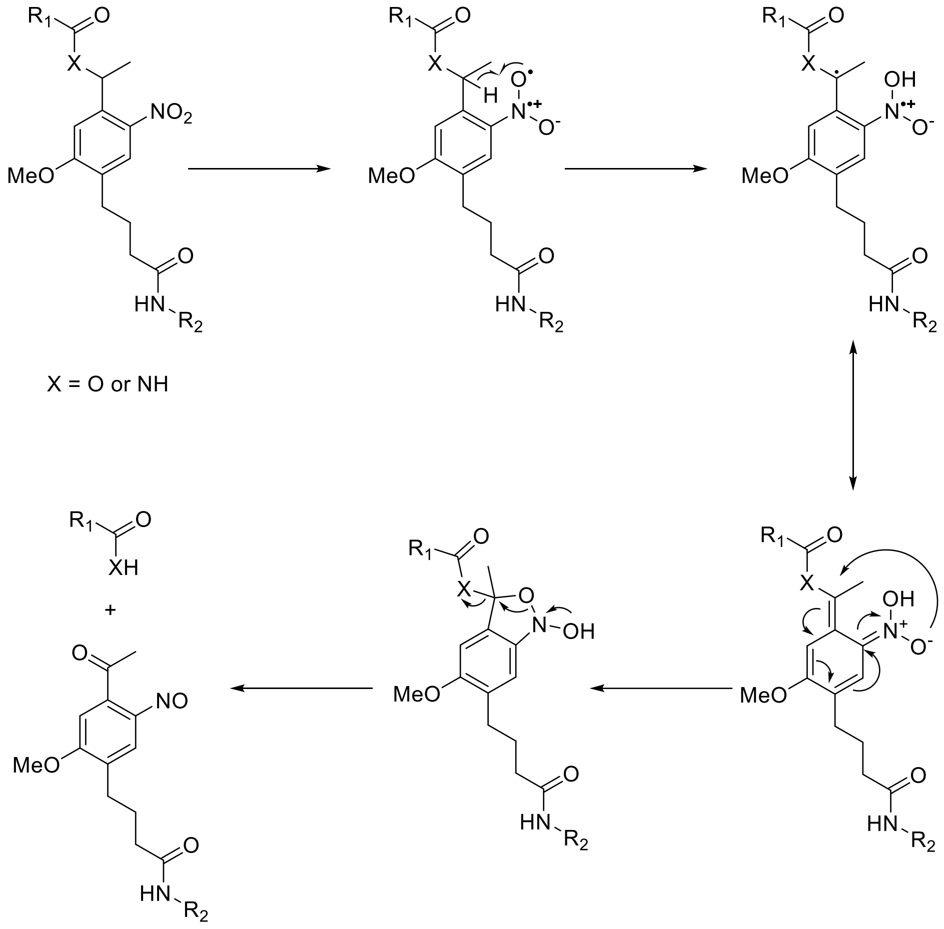

Figure 5: Mechanism behind the Norrish type 2 cleavage reaction of the photolabile linker employed for solid-phase synthesis on DMA. R1 indicates the bond to the target molecule, R2 represents the surface of the DMA.[49]

As a first proof-of-concept, ROSENFELD *et al.* showed in the same report a synthetic route to a combinatorial library of tripeptides in the array format. Therefore, they applied a combination of *Steglich* esterification to attach an Fmoc-protected amino acid to the photolabile linker followed by the classical solid-phase peptide synthesis sequence of Fmoc-deprotection and carbodiimide-mediated 1-hydroxybenzotriazole (HOBT) catalyzed amide coupling.[50, 51] This showed for the first time, that the DMA was compatible with classical solid-phase synthesis techniques that are widely applied, such as the shown strategy for the sequence-controlled preparation of polypeptides.

Following a similar approach, BREHM *et al.* used the same solid-phase concept to adapt a multicomponent reaction protocol for the preparation of combinatorial libraries in one step. They applied immobilized amino acids on the surface as well, utilizing the surface-amines for UGI four component reaction.[52] This reaction is initiated by the condensation of an amine with an aldehyde to form an iminium ion intermediate that reacts with a carboxylic acid and an isocyanide to form bisamides, the mechanism is not finally clarified (Figure 6).[53] As for all multicomponent reactions, the number of product molecules from a certain number of starting materials is greatly increased compared to reactions with only two reaction partners, making it prominent reaction for library construction.

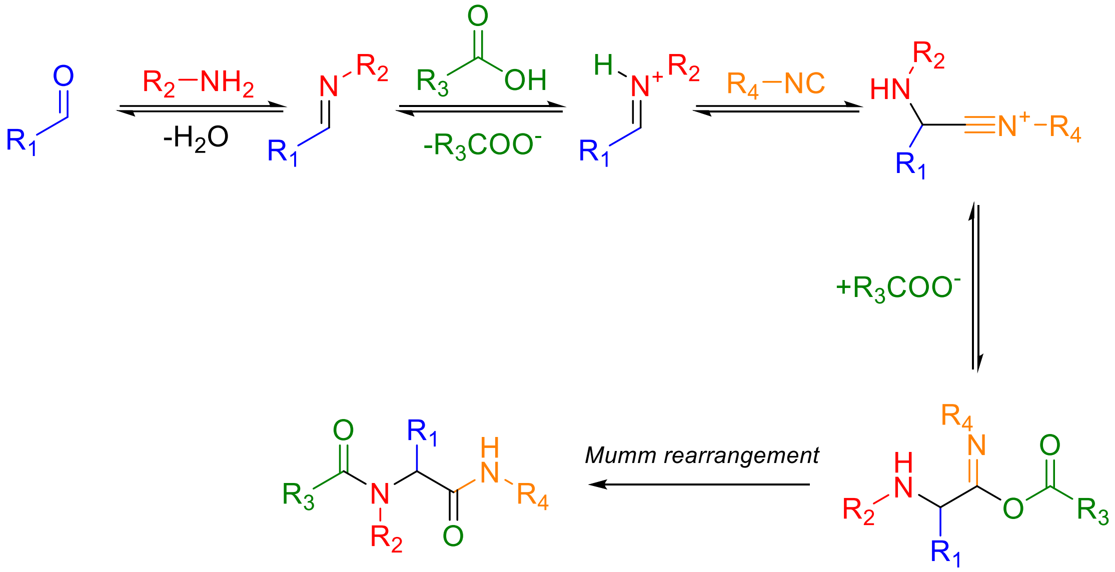

Figure 6: One possible reaction pathway for the formation of bisimide products during *Ugi* four component reaction. All reaction steps are reversible until the *Mumm* rearrangement that yields the bisimide as final product.[53]

The most prominent side reaction to the UGI reaction is the PASSERINI reaction, that involves only three components: an acid, an aldehyde and an isocyanide.[54] By choosing to attach the product through surface amines, the contamination of the target compound with the PASSERINI side product can be avoided.

Another important addition to the chemical toolbox of the DMA was the addition of cross-coupling reactions, in particular one of the most applied reactions in medicinal chemistry, the SUZUKI-reaction (Figure 7).[55] A major limitation of palladium-catalyzed coupling reactions is the frequent requirement of heating to achieve good conversions and the sensitivity of many catalysts towards oxygen.[56] HÖPFNER *et al.* developed an adjusted protocol that works efficiently without protective gas at ambient temperature and that allows the preparation of the respective C-C-coupled products from surface-bound bromides with purities of up to 97 % after cleavage.[57]

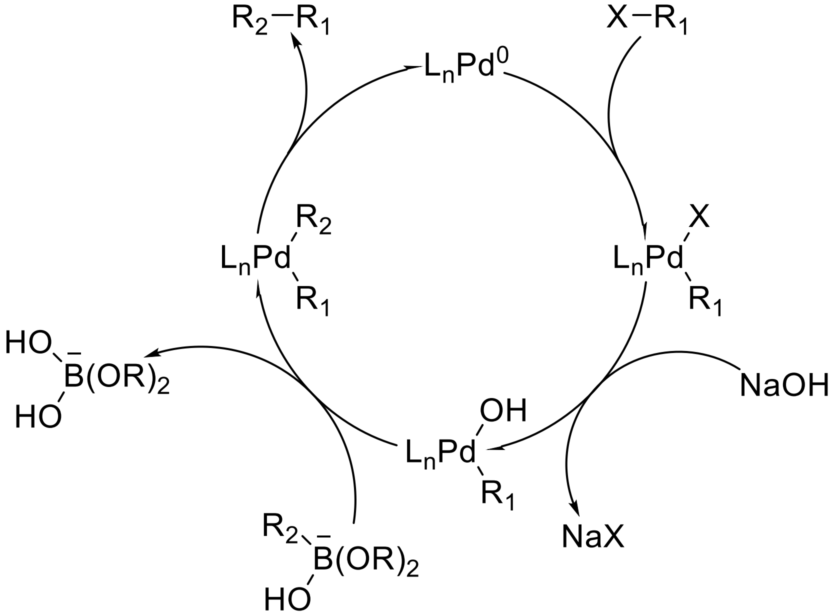

Figure 7: Catalytic cycle for the SUZUKI-cross coupling.

The key aspect in palladium-catalyzed cross-coupling reactions is the formulation of the catalytic species. The properties of the catalyst affect the activation energy for the oxidative addition of the organo-halide as well as the tendency of Pd(0) species to precipitate during the reaction, reducing the amount of available catalyst in solution. Therefore, the choice of the ligand determines the efficacy of the reaction under given conditions. By incorporating dibenzyl-*N*,*N*-diisopropylphosphoramidite as ligand, HÖPFNER et al. were able to achieve a catalyst system that was able to perform efficiently at room temperature and under oxygen atmosphere.

All the above reactions were shown to work efficiently, delivering the desired compounds with good yields and purities in their respective model systems, making them suitable for subsequent biological evaluation to identify compounds with desired properties.

But not just small molecules can be prepared on the DMA, as ROSENFELD et al. demonstrated that the DMA can be further used to fabricate and analyze polymeric materials.[58] They applied radical polymerization of methacrylic monomers and crosslinkers to obtain hydrophilic, three-dimensional polymer networks. Radical polymerization is very susceptible to termination induced by the Prescence of oxygen, so called oxygen inhibition, which leads to the formation of hydroperoxides. The impact of oxygen inhibition is even more severe for small droplets due to the increased surface-volume ratio and the reduced diffusion pathways for oxygen. To overcome this, they applied a simple biochemical oxygen scavenger system consisting of glucose oxidase and glucose. They could demonstrate that this system yields homogeneous networks in a reproducible fashion. By this, they created a proof-of-principle library which contained 18 different materials made of two different monomers and one crosslinker at different molar ratios of all three components. By applying additional UV-irradiation of higher energy after the polymerization process, they were able to degrade those hydrogels and analyze their photostability.

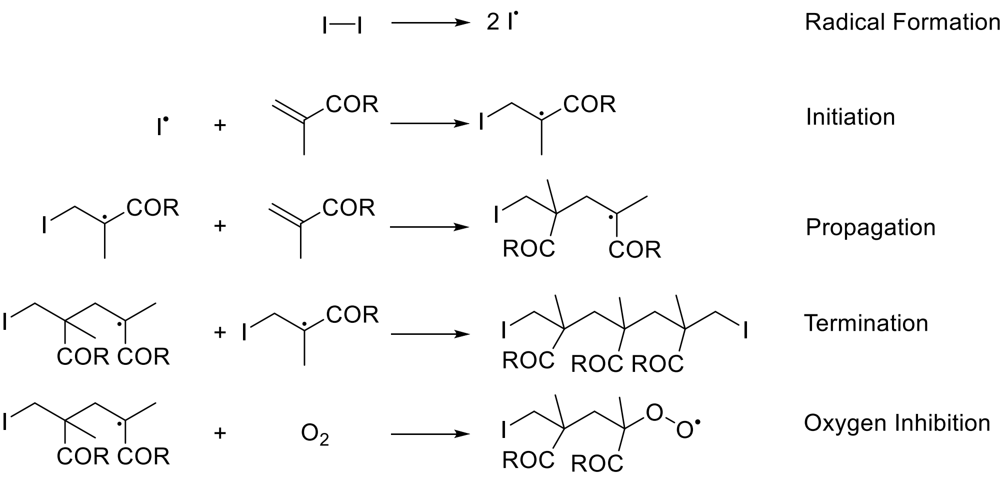

Figure 8: Schematic depiction of the different reaction steps involved in the free radical polymerization of methacrylates.

Since the DMA was therefore shown to not just be compatible with chemical workflows, but biological experimentation and material preparation as well, this opened the opportunity to create integrated screening pipelines that would allow to perform combinations of these experimentation techniques in the same confined space in a miniaturized and high-throughput fashion.

2 Results and Discussion

2.1 High-Throughput Synthesis of Photodegradable Hydrogels

2.1.1 Introduction

2.1.1.1 Smart Materials and Materials Design

Smart materials or stimuli-responsive materials are a very broad class of materials that respond to a certain external stimulus in a defined way. These stimuli as well as the respective response can be of various natures and are generally sought to be applied in a variety of different scenarios when trying to control dynamic processes, for example in sensors or biomedical devices.

Since responsiveness is one of the key features all living things share, it is safe to assume that naturally occurring biological systems often served as model systems for the designed systems. As such, temperature plays the role of one of the most important if not the most important stimuli applied in responsive materials. One of the earliest examples of such temperature responsiveness was discovered in 1967 by *Scarpa et. al.* when working with poly(*N*-isopropylacrylamide) (poly(NIPAM)).[59] They observed an inverse relation between solubility of the polymer and the temperature, leading to the so called “lower critical solution temperature” (LCST) as the temperature above which the polymer precipitates from the solution. For poly(NIPAM) this occurs due to the competition between intermolecular hydrogen-bonding between the polymer and the solvent, and the intramolecular hydrophobic interactions of the polymer residual groups.[60] When the temperature rises, the intermolecular interactions are disrupted and the intramolecular ones are favored leading to an aggregation and finally to phase-separation. This phenomenon was extensively studied and largely applied in fields such as biomedical applications[61-64], drug delivery[65-67] or as soft actuators.[68-70]

Besides temperature, another stimulus of key importance is light. Light offers an additional degree of control both regarding the localization as well as the dosage and is therefore a promising alternative for additional precision. Light-responsiveness usually relies on the implementation of different photoresponsive chemical motifs, such as *o*-nitrobenzene[71], coumarin[72], azobenzene[73], diarylethene[74], spiropyranes[75] or donor-acceptor Stenhouse adducts (Figure 9).[76] These photoresponsive units can be generally categorized into three types based of the processes occurring upon irradiation: isomerization, dimerization and single bond cleavage. The motifs that undergo cleavage of a single bond upon irradiation (e.g. *o*-nitrobenzyl-groups, coumarin) usually serve as photocages and are applied to restrict the reactivity of specific functional groups until desired. This can be used in different ways, for example for the spatially controlled covalent functionalization of networks after the network formation.[77] Even though this approach offers no reversibility due to the underlying mechanism, it is widely used in combination with techniques such as photolithography to generate 2D- or 3D-structued networks. On the other hand, there are the isomerization and dimerization processes. These processes often exhibit an equilibrium between the two distinct states, making it possible to gain dynamic control over the materials properties. For the equilibrium between spiropyran and the respective merocyanine, this control is often achieved through a combination of light-induced ring opening, followed by thermal relaxation (Figure 9).[78] In general, the stimulus to initiate the back reaction is highly dependent on the specific motif used and can therefore be tuned to the needs of the situation in both initiation and kinetics by variation of the photoresponsive group.

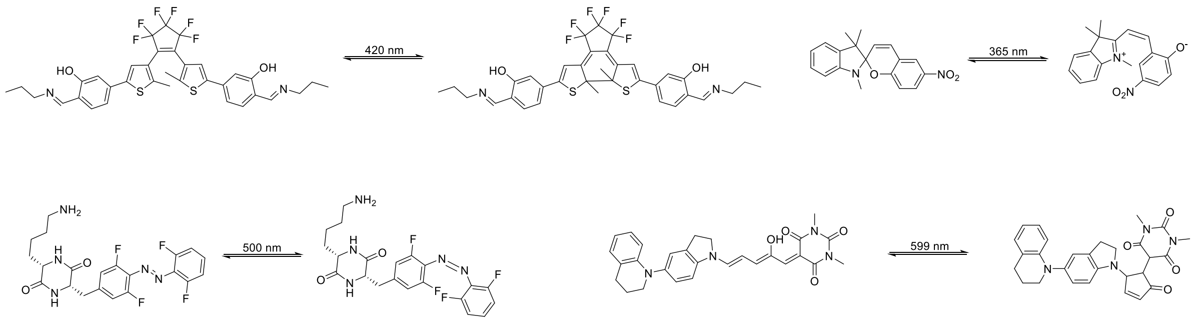

Figure 9: Structure of four different photoresponsive groups employing different mechanisms for their photoresponse and their respective wavelengths of light used to initiate the response.[79-84]

One major aspect that highly distinguishes the mentioned systems from biological systems is their ability to respond to a cascade of different stimuli at once. To address this, so-called multi-responsive systems are being developed. These systems can respond to different stimuli at once with different reactions, giving a higher amount of control over the materials properties and therefore allowing the regulation of more complex processes as is required e.g., for the controlled growth of cells or tissue.[85] Since chemical groups that respond to multiple external stimuli in a controlled way are scarce, the most common approach for the generation of multi-responsive systems is the combination of different single-responsive materials.[86] The main requirement for this multimaterial approach is the availability of materials that possess the desired response to choose from. Due to this, there is a demand for huge amounts of data about the behavior of different materials. While theoretically possible, the generation of this amount of data in traditional one-by-one fashion is neither feasible nor sustainable due to the sheer amount of resources required for this process. A possible alternative to speed up the discovery process is the application of machine learning (ML) which has been extensively shown over the last years in fields such as chemistry[87-89], biology[90-92], drug discovery[93-95] and material science.[96-98] ML models generally allow for a faster processing of data and the prediction of unknown properties based on available data, therefore speeding up optimization processes[99-101] and revealing hidden relations within data sets.[102-105] The immense amount of data that is required to ensure a reliable prediction is currently mostly being derived from individual data sets generated in traditional one-by-one fashion. To keep up with the rising demand and reduce the material consumption at the same time, high-throughput techniques and miniaturization are becoming more and more essential in general research.

2.1.1.2 Motivation and Aim

The aim of this work was to develop and apply an experimental pipeline that allows to create soft materials on a nanoliter scale and evaluate their physical properties in a high throughput fashion. Since light is a convenient stimulus and can be broadly applied, it was decided to further study the inherent photosensitivity of methacrylate-based hydrogels that has been investigated by SCHEIGER *et al.* previously.[106] Methacrylate-based hydrogels and organogels exhibit a photodegradability without the use of any additional photosensitive-residue, making them potential candidates for the fabrication of multi-material scaffolds as vehicles for drug or cell release.[107]

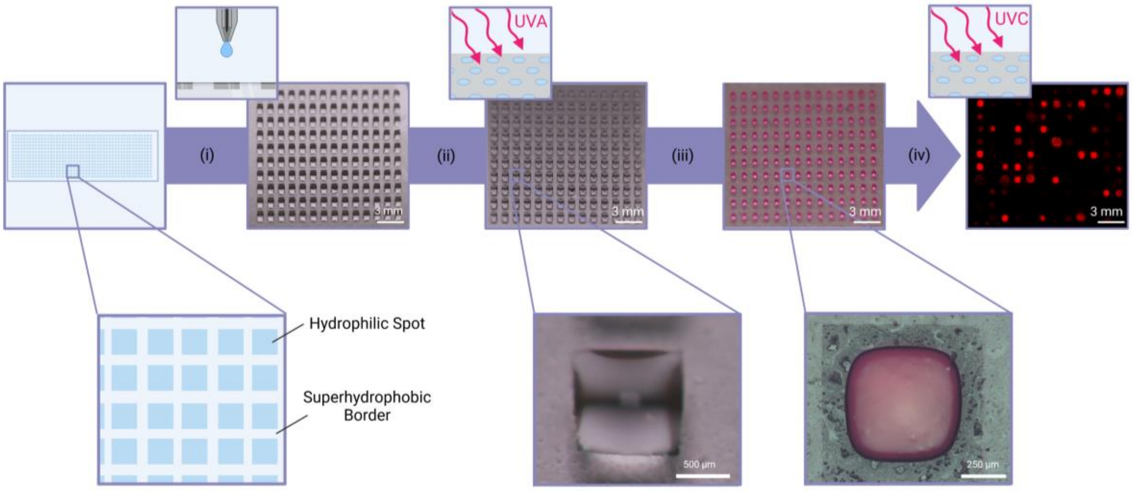

Figure 10: Schematic depiction of an experimental workflow for the nanoliter-scale preparation and analysis of photodegradable hydrogels on DMA: (i) Dispensing solutions of initiator, monomers and crosslinkers, (ii) photopolymerization through UVA-light, (iii) fluorescence staining with Rhodamine 6G, (iv) cycles of UVC irradiation and fluorescence microscopy to monitor the photodegradation. The figure was adapted from SEIFERMANN *et al.*[1]

Based on a workflow by ROSENFELD *et al.*, an experimental setup was developed that would generate enough data with enough parameter-variance to apply ML in order to predict a variety of untested compositions and expand the availability of materials with characterized properties rapidly (Figure 10).[58] The commercial availability of methacrylate, acrylate, methacrylamide and acrylamide monomers and crosslinkers would allow for the generation of a comparably large library of materials even with the use of just binary material compositions. Due to the abundant use of acrylic monomers and crosslinkers in commonly applied materials, a variety of them is commercially available, which is why they were regarded as perfect candidates for an exemplary study.

2.1.2 Protocol Optimization

In order to develop suitable conditions for the preparation of hydrogels on a nanoliter scale, a model system of hydrogels published by ROSENFELD *et al.* consisting of ternary mixtures was used and prepared on a DMA.[58] These hydrogels are copolymers of poly(ethylene glycol) methyl ether methacrylate (Mn approx.. 500 g/mol) (PEGMA), 2-(N-3-sulfopropyl-N,N-dimethyl ammonium)ethyl methacrylate (SAMA) with poly(ethylene glycol) dimethacrylate (Mn approx. 750 g/mol) (PEGDMA) as crosslinker at different ratios. To negate the impact of oxygen on the polymerization, the final polymerization solutions were all supplemented with glucose (0.1 M) and glucose oxidase (40 µM). Lithium phenyl-2,4,6-trimethylbenzoylphosphinate (LAP) was chosen as the photo initiator at a final concentration of 5 mg/mL with an irradiation wavelength of 380 nm due to sufficient absorbance in the respective UV/Vis spectrum.

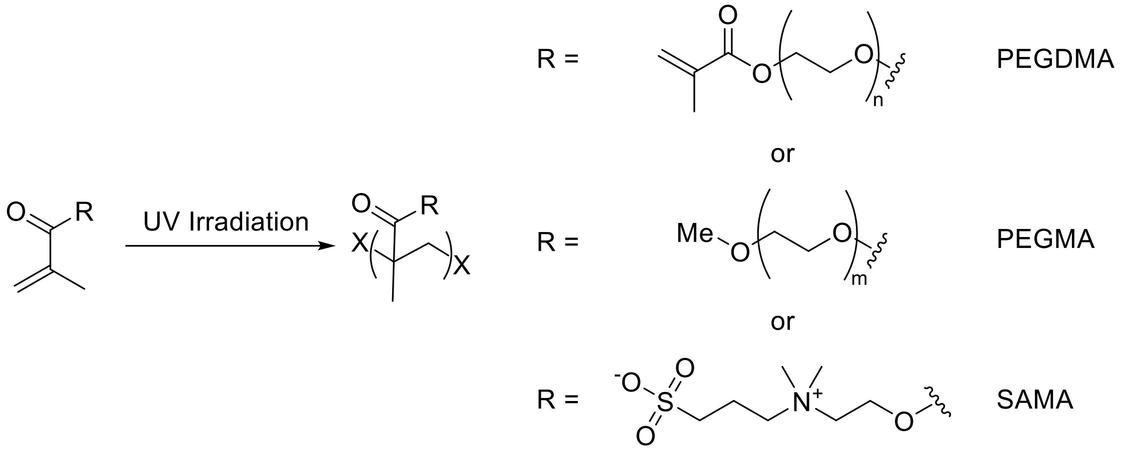

Figure 11: Reaction equation for the radical polymerization of crosslinked soft materials from methacrylic monomers. X resembles residual groups of the initiating or terminating species.

To fabricate the hydrogels with a total volume of 130 nL (prior to swelling), stock solutions of the respective monomers (0.83 M), the crosslinker (0.206 M for 10 mol% crosslinker or 0.103 M for 5 mol% crosslinker w.r.t Monomers) and the initiator solution containing LAP (22 mg/mL), glucose (0.44 M) and glucose oxidase (173 µM) were prepared in PBS buffer. The liquids were then dispensed onto the spots of a DMA using a *Certus Flex* liquid dispensing system (Fritz Gyger AG, Gwatt, Switzerland). The DMA used for the following experiments contained 672 spots (14 columns x 48 rows, 1 x 1 mm^2 spot size). For the final composition, 30 nL initiator solution, 30 nL crosslinker solution and 70 nL in total of the two monomer solutions were added to each spot. From here, the polymerization could be carried out as radical photopolymerization, with the most important parameters being the duration and the intensity of the irradiation step. To optimize these conditions, four different hydrogel compositions consisting of the two monomers and the crosslinker were fabricated under different polymerization conditions (Figure 11).

The combinations tested were containing different PEGMA:SAMA ratios (6:1, 5:2, 4:3, 3:4) with 10 mol% crosslinker and the three different combinations of irradiation settings were 15 min irradiation at 18.0 mW/cm^2, 25 min at 9.01 mW/cm^2 and 30 min at 5.41 mW/cm^2.

The polymerization at 18.0 mW/cm^2 did not yield homogeneous pads and was therefore disregarded. The other two settings delivered transparent and homogenous pads. To determine if the polymerization is complete, an indirect method was chosen. Since the materials are known to be photodegradable under UVC light, irradiation with such should induce a reduction in the pad size. To measure this, hydrogel pads were produced under the same polymerization conditions on two different slides with 10 replicates each. One of the slides was directly afterwards subjected to 60 s of UVC irradiation, then both slides were stained and swelled by submerging in an aqueous solution of Rhodamine 6G (10 mg/mL).

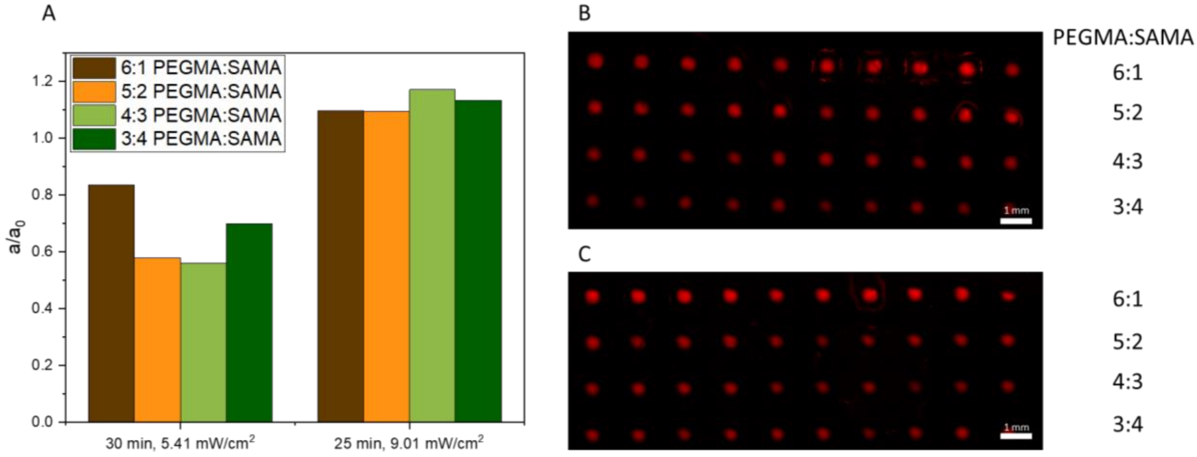

Figure 12: (**A**) Ratio of hydrogel area after 1 min of UVC irradiation (a) to the area of the same composition without UVC irradiation (a_0) for 4 different ratios of PEGMA to SAMA and under two different polymerization conditions. Fluorescence microscopy images of the 4 different compositions polymerized for 30 min at 5.41 mW/cm2 stained (B) directly after polymerization or (C) after 1 min of additional UVC irradiation. Figure adapted from SEIFERMANN *et al.*[1]

After staining overnight, the slides were analyzed through fluorescence microscopy and the gel size was calculated. If the gel size of the UVC irradiated slide was reduced compared to the unirradiated one, degradation was initiated, if the size was the same or higher, it was assumed that remaining monomer and crosslinker underwent additional polymerization during the second irradiation step. For 25 min irradiation, no reduction in gel area or even an increase was observed, whereas for 30 min a clear reduction for all 4 compositions was visible (Figure 12). Thus, 30 min at 5.41 mW/cm^2 were deemed suitable and used as the polymerization conditions for all subsequent experiments.

To see if these conditions are suitable to monitor the degradation course on the DMA, another six different compositions were prepared with ten replicates on 130 nL-scale, thereby tested were three different ratios of PEGMA:SAMA ratio (6:1, 3:4, 2:5) with two different amounts of crosslinker (5 mol% and 10 mol% w.r.t Monomer). The sample preparation was done with a liquid dispenser from 5 different stocks as described before to yield 130 nL droplets of prepolymerization mixture. These were then polymerized with 30 min irradiation at 5.41 mW/cm^2 to yield 60 hydrogel pads on DMA. These pads were submerged overnight in Rhodamine 6G solution to fully swell them, remove residual initiator and other remains and to stain them.

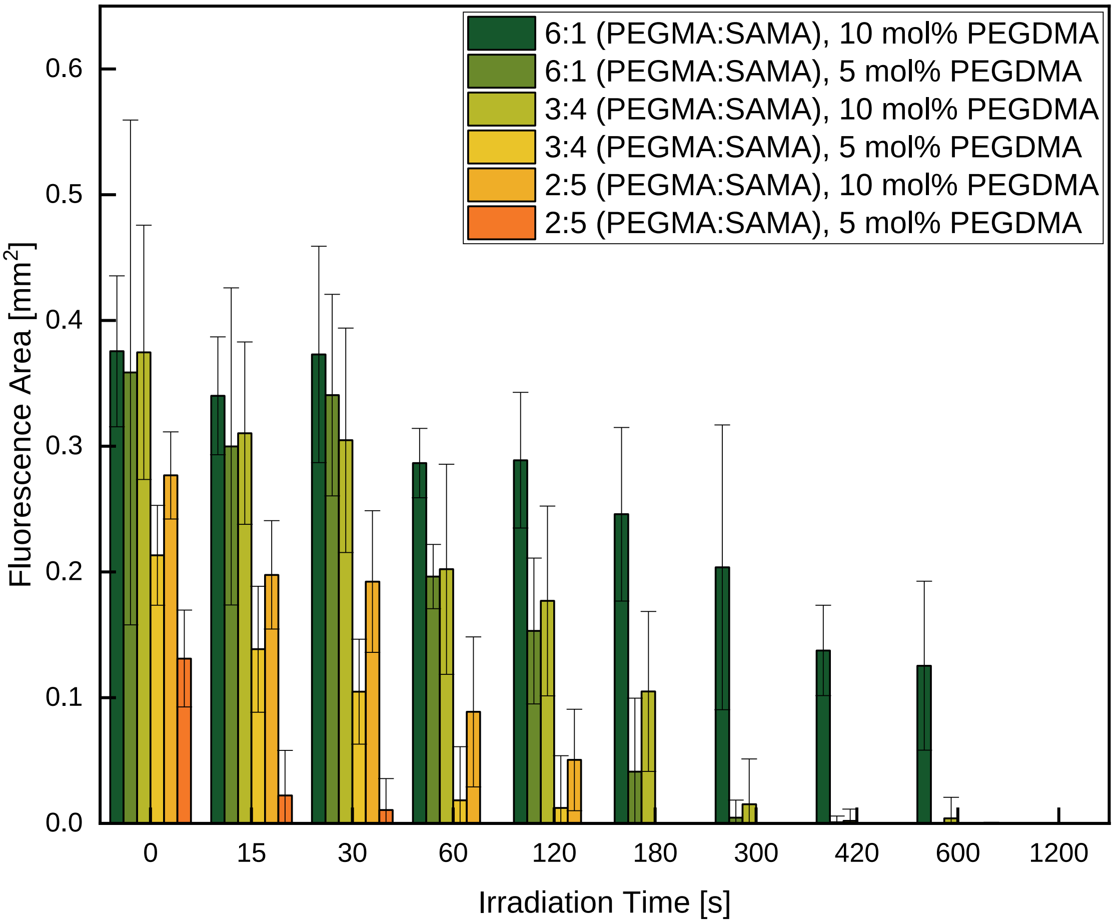

Figure 13: Measured fluorescence area of a series of different hydrogel pads consisting of poly(ethylene glycol) methacrylate (Mw=500 Da) (PEGMA) and [2-(methacryloyloxy)-ethyl]dimethyl-(3-sulfopropyl) ammonium hydroxide(SAMA) with different PEGMA:SAMA ratios and different amounts of poly(ethylene glycol) dimethacrylate (Mw=750 Da) (PEGDMA) as crosslinker through the course of 20 min irradiation with UVC light. After swelling in Rhodamine 6G overnight, the gels were irradiated with UVC light (11.5 mWcm−2, 200–280 nm) and measured by fluorescence microscopy successively. Values were acquired by continuous measurements on the same slide. Error bars show the standard deviation between 10 replicates each. Figure adapted from SEIFERMANN *et al.*[1]

Afterwards, the slide containing these pads was enclosed in a petri dish containing 2 mL of PBS in the bottom to increase the humidity and prevent the pads from drying. These stained gels were imaged *via* fluorescence microscopy, then the lid was replaced with a quartz glass plate and the slide was subjected to UVA irradiation for 15 s. Afterwards the dish was sealed again, and the slide was imaged using fluorescence microscopy again. This cycle was repeated over and over to obtain images for 0, 15, 30, 60, 120, 180, 300, 420, 600 and 1200 s of total UVA irradiation time. For the analysis of the fluorescence area, a python-based edge detection code was used, provided by *Dr. PATRICK REISSER*. This delivered 600 total measurement points to describe the degradation of 6 different materials in parallel (Figure 13). The observable trend was that all those gels exhibited photodegradation, where the materials with high content of crosslinker or less polar monomer (PEGMA) showed a generally slower decay compared to those with low content of crosslinker or higher amount of highly polar monomer (SAMA). This was in accordance with the already published degradation behavior and was thus regarded as confirmation that the fabrication protocol was working and delivering good results for known compositions.

To assure that the reduction in size was an inherent property of the material and not induced by side effects of the miniaturization e.g., evaporation, or by side-reactions of the dye, such as formation of reactive oxygen species or photobleaching, a set of non-degrading gels was tested on nanoliter scale as well. These gels consisted of poly(ethylene glycol) methyl ether acrylate (Mw approx. 480 Da) (PEGA) crosslinked with 1, 2 or 3 mol% of poly(ethylene glycol) diacrylate (Mw approx. 700 Da) (w.r.t monomer). For each of the three gel types, 24 replicates were prepared from 130 nL prepolymerization mixture per pad using the previously established protocol on DMA. After staining them overnight by submerging in Rhodamine 6G solution, the gels were imaged *via* fluorescence microscopy, then subjected to 10 min UVC irradiation and imaged again. The fluorescence area prior to irradiation and after irradiation was compared and no significant decrease in gel size could be observed, indicating stability of the gel under these conditions (Figure 14). Thus, it was demonstrated that it is possible to differentiate between degradation behaviors using the method and that the behavior of already characterized materials obtained from this workflow is in accordance with previous findings.

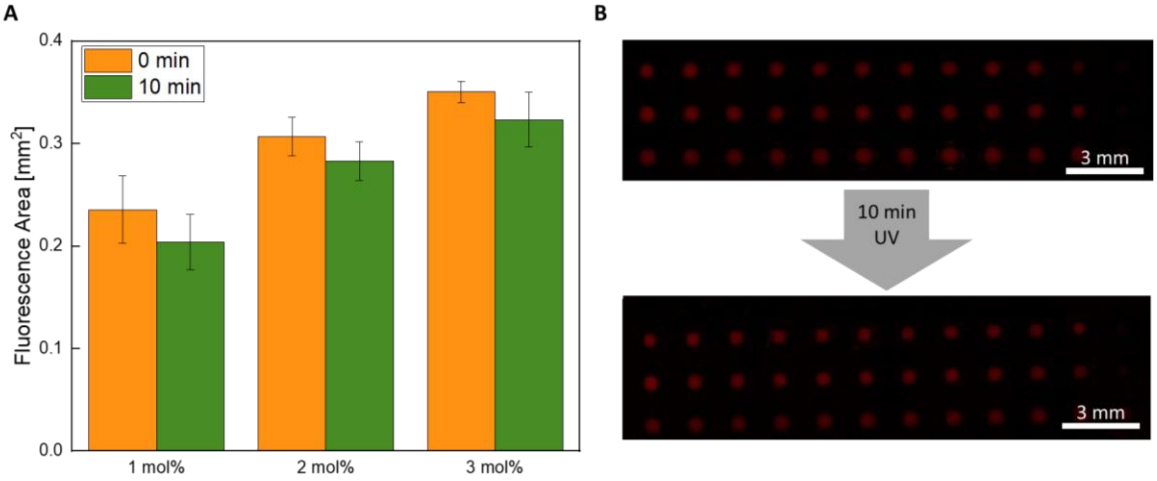

Figure 14: (A) Evaluation of gel stability under the influence of rhodamine 6G as a possible photosensitizer, to make sure the staining does not induce degradability. Nondegrading hydrogels made from poly(ethylene glycol) acrylate (Mw=480 Da) and different amounts (in mol%) of poly(ethylene glycol) diacrylate (Mw=700 Da) were irradiated for 10 min after incubation with rhodamine 6G overnight and afterward the change in fluorescence area was compared to check for degradation. Error bars are the standard deviation between 24 replicates. (B) Fluorescence microscopy images of nondegradable hydrogels on 1 mm spots stained with rhodamine 6G before and after UVC irradiation. Figure adapted from SEIFERMANN et al[1]

With the most important parameters set, the next step was to prepare a small library of novel materials followed by their characterization. In order to reduce the environmental effect on the measurement, the spots directly next to the edge of the slide were not used for experiments and instead filled with pure solvent to prevent concentration changes in the sample spots. This reduced the number of available reaction-vessels per slide to 552. On top of that, to reduce environmental bias caused by the position of the gel pad on the slide, all layouts were randomized. By spreading the replicates of every material throughout the entire slide, the layout and readout get more complicated and the standard deviation between all replicates is expected to increase, but the experimental bias is reduced, making the values more comparable. By this, a total of 92 different materials with six replicates could be prepared and analyzed per slide, consuming 72 µL of stock solutions in total. In this first experiment, 23 different monomers and 4 different crosslinkers were used to produce 92 different binary materials. To get an additional variable in the data set for later application in machine learning, the crosslinker content was varied between 5 to 15 mol% for the different materials. The dispensing procedure for the fabrication of these hydrogels consisted of 2328 printing steps per slide from 29 different stock solutions. Afterwards, these gels were polymerized as described earlier and stained with rhodamine 6G overnight.

As an additional measure against evaporation, the slide was sealed after the staining. For this, the slide with the polymerized gels was taken out of the staining solution and excess liquid was removed. Afterwards, a quartz glass slide was attached as a cover which was sealed with a PDMS on top of the hydrophobic edge of the DMA slide. The sealed slide was then subjected to cycles of UVC irradiation (0-1200 s) followed by fluorescence microscopy. To monitor the degradation more precisely, the fluorescence area of each gel pad as well as the integrated pixel intensity was then extracted to obtain the final degradation curves. The combination of these parameters allowed to evaluate the gel stability more independent from their respective mode of degradation. (Figure 15)

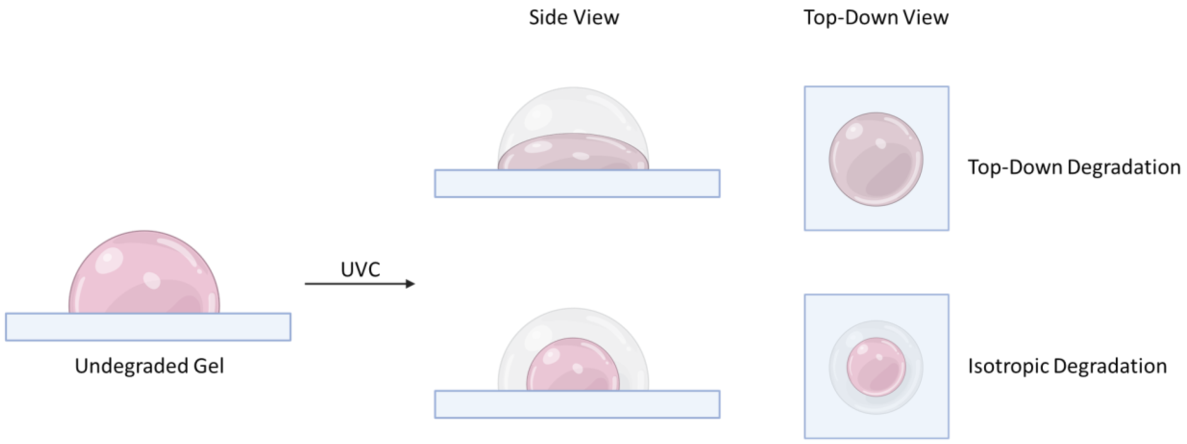

Figure 15: The two extreme degradation modes possibly occurring when irradiating the nanoliter sized hydrogels. Upon irradiation the gels can undergo symmetric degradation, thereby reducing the gel pads size in all directions comparably which leads to reduced fluorescence area as well as intensity (Isotropic degradation). Alternatively, the gels can degrade anisotropically along with the angle of incidence of the UV irradiation, reducing the overall fluorescence intensity without significantly reducing the fluorescence area (Top-Down degradation). This can lead to differences in the degradation curves measured from fluorescence intensity and from fluorescence area. Figure created with Biorender.com.

The preparation of the same library was repeated in two more independent experiments under the same conditions. These showed high standard deviations within the experiment for some compositions, indicating a severe environmental impact at least for some materials, but confirmed a good reproducibility of the synthetic and analytic workflow in general (Figure 16).

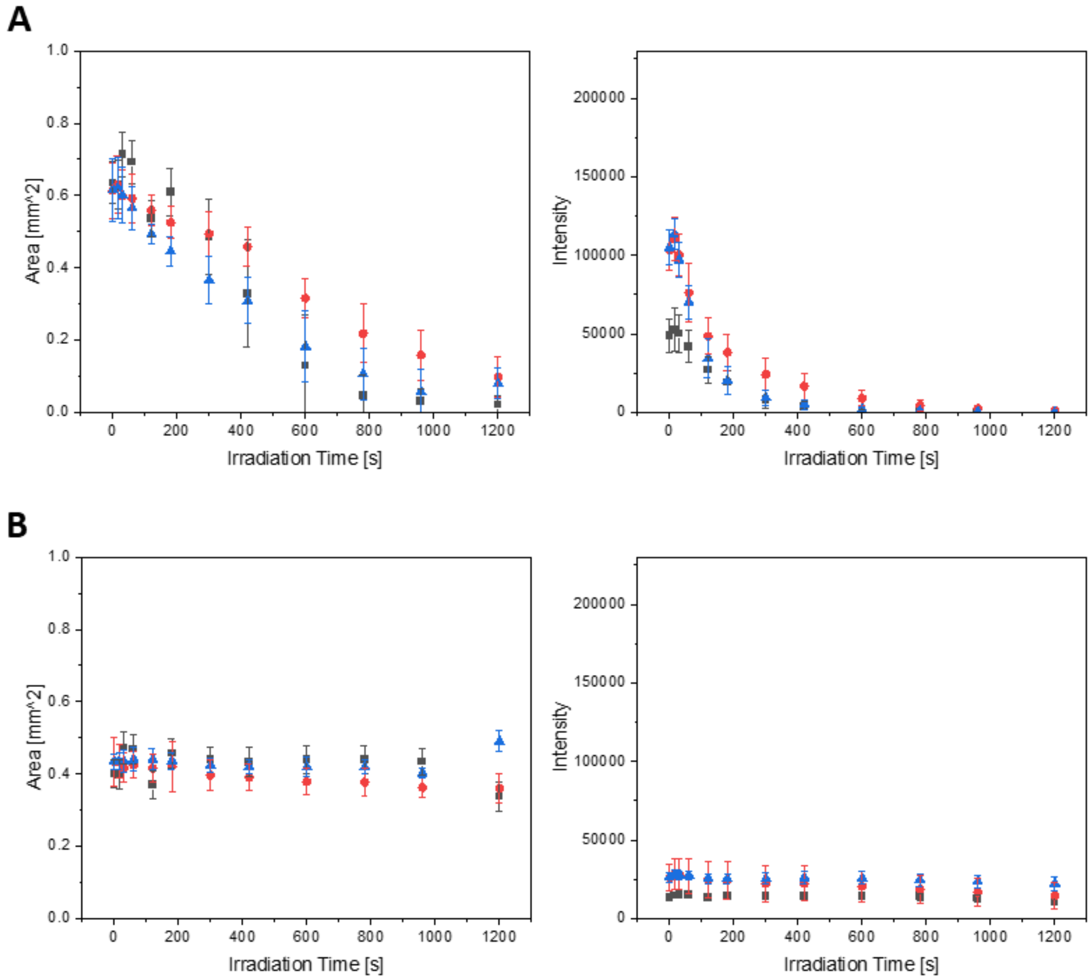

Figure 16: Fluorescence Area and integrated intensity throughout the course of irradiation for two different types of hydrogels in three independent experiments (blue, red, black) with 6 replicates each. (A) mono(2-acryloyloxyethyl) succinate crosslinked with 9.5 mol% glycerol dimethacrylate, (B) α-methylene-γ- butyrolactone crosslinked with 7.5 mol% glycerol dimethacrylate. Error bars show the standard deviation of six replicates. Figure adapted from *Seifermann* et al[1]

2.1.3 Screening Procedure

With the confirmation of the reproducibility, the next step was the preparation of a full library. The aim was to prepare and analyze approximately 1000 different materials in the same fashion. For this, 56 different monomers and 20 crosslinkers were chosen. These compounds were selected to cover a large chemical space, including various different chemical functionalities such as alcohols, amines, carboxylic acids, sulfonic acids, ethers and halides as well as aromatic and saturated cycles. On top of that, a broad range of molecular weights was chosen, ranging from 70 to 750 Da. The polymerizable groups used were either acrylates, methacrylates, acrylamides or methacrylamides and the number of polymerizable groups in the crosslinker varied between 2 and 3.

From this set of compounds, 11 slides containing over 1000 different materials were prepared. The materials were produced following the same procedure described in chapter 2.1.2 from 130 nL precursor mixture for each gel pad with fully randomized layouts. The slides were then irradiated and analyzed to yield over 66.000 measurement points. The results showed already a broad distribution in both the initial size and intensity of the different gel pads as well as in their degradability. (Figure 17)

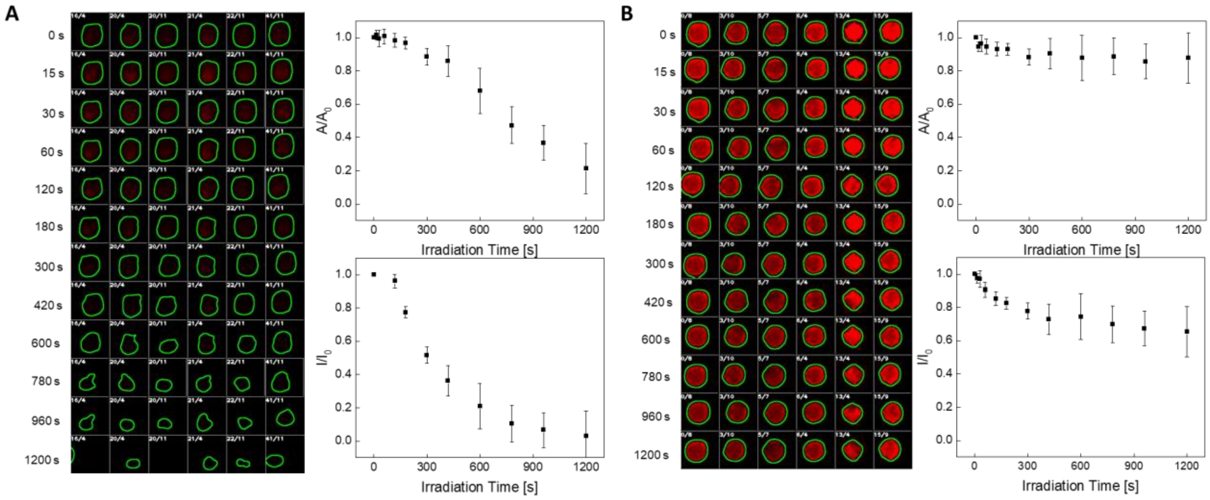

Figure 17: The course of degradation for two different sets of nanoliter sized hydrogel pads throughout UVC irradiation. Each row shows the 6 repetitions for each hydrogel after the given irradiation time together with their relative position on the slide (white number, Row/Column). The graphs show the relative fluorescence area and integrated fluorescence area of each repetition over the course of 20 min UVC irradiation. Given values are the mean value of the individual spots values (I) normalized to the starting value of the respective spot (I_0). Error bars are the standard deviation between the 6 replicates. Hydrogels consist of (A) 2-Hydroxyethyl Methacrylate, crosslinked with 8.5 mol% 1,4-Butandiol Diacrylate and (B) 2-Hydroxy-3-phenoxypropyl Acrylate crosslinked with 6.5 mol% *N,N*-Methylenebiscralyamide. Figure adapted from SEIFERMANN *et al.*[1]

The generated data points were further analyzed and used to develop a machine learning model by *Dr.* *PATRICK REISSER* (ITI). For this, the degradation measurements for each material were fitted to the formula:

$$N(t) = N_0 e^{\frac{-t}{\tau}}$$

In this, N is defined as the fluorescence area or integrated fluorescence intensity at the time t, N_0 the respective value prior to irradiation and τ as the lifetime, the key parameter describing the degradation behavior.

With the square root of N_0 for both the initial size and intensity and the natural logarithm of τ as learnable targets, the data was used to train to gaussian process regression models to predict the combined square root of the intensity plus the logarithm of the lifetime and the combined square root of size plus the logarithm of the lifetime. These values were then compared to the ground truth to assess the quality of the fit *via* R^2 and the mean absolute error (MAE).

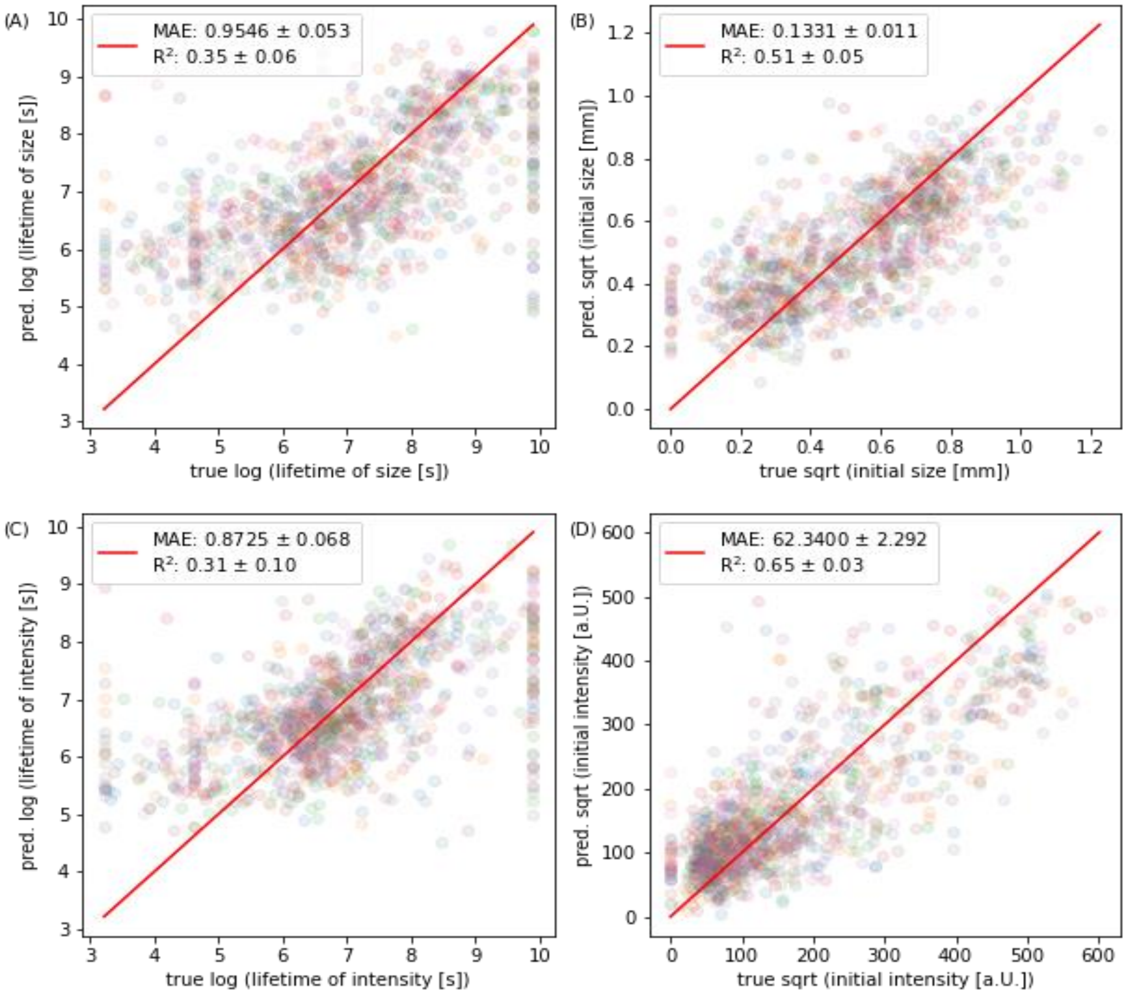

Figure 18: Predictions of a multi-task Gaussian process regressor trained on a 7-fold split of the data. The colors indicate each fold. Figure adapted from SEIFERMANN *et al.*[1]

2.1.4 Validation and Proof-of-Concept Application

One important parameter to test was how well the degradation behavior of these unknown materials characterized on the nanoliter scale translates back to bulk material. In order to investigate this, four different materials were produced in an upscaled experiment: mono-2-(methacryloyloxy)ethyl phthalate, crosslinked with 6.5 mol% poly(propylene glycol) dimethacrylate, poly(ethylene glycol) methyl ether methacrylate, crosslinked with 6.5 mol% glycerol dimethacrylate, 4-hydroxybutyl acrylate, crosslinked with 7.5 mol% trimethylolpropane ethoxylate methyl ether diacrylate and N-(2-acryloyloxyethyl)-N-benzyl-N,N-dimethylammonium chloride, crosslinked with 7.5 mol% trimethylolpropane ethoxylate methyl ether diacrylate.

For each of these materials, three gels polymerized from 150 µL prepolymerization mixture were prepared through UV-induced polymerization in a PTFE mold. The prepolymerization mixture contained the same compounds at the same concentrations and ratios as in the nanoliter experiment, but without the addition of glucose and glucose oxidase. Instead, the mixtures were all degassed for 15 min using nitrogen flow. After the polymerization, the gels were submerged in PBS for 7 days to assure full swelling. Excess water was removed from the gels, and they were weighed to define the starting point. After the initial weighing, the gels were sealed in a petri dish with a quartz glass lid at high humidity and exposed to UVC irradiation. After each irradiation step, the liquified parts were removed and the gel was weighed again. This procedure was repeated over and over to generate degradation curves similar to the ones generated on the DMA.

Each individual gels values were normalized to the respective starting value to calculate a relative decay. The three relative degradation curves were combined to yield the average and then compared to the respective relative degradation curves generated for the same materials on DMA. The curves showed a good comparability in the trends for three of the four composites and a modest accordance for on them. This reflects in the standard deviation for the individual lifetimes of the different materials calculated from the different measurements of weight, area, and intensity (Figure 19).

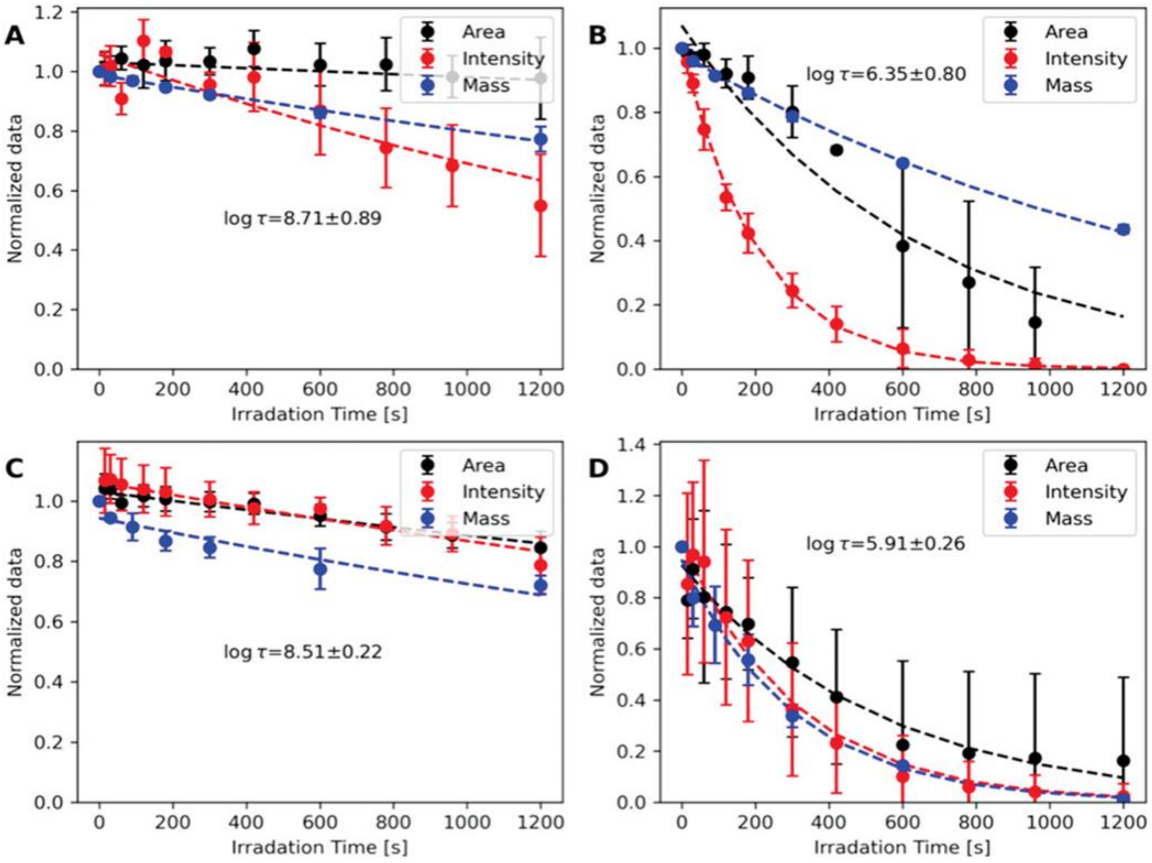

Figure 19: Degradation curves measured from fluorescence area on nanoliter scale, fluorescence intensity on nanoliter scale and mass loss on microliter scale, together with their respective exponential fits. Four types of hydrogels were investigated: (A) mono-2-(methacryloyloxy)ethyl phthalate, crosslinked with 6.5 mol% poly(propylene glycol) dimethacrylate, (B) poly(ethylene glycol) methyl ether methacrylate, crosslinked with 6.5 mol% glycerol dimethacrylate, (C) 4-hydroxybutyl acrylate, crosslinked with 7.5 mol% trimethylolpropane ethoxylate methyl ether diacrylate, and (D) N-(2-acryloyloxyethyl)-N-benzyl-N,N-dimethylammonium chloride, crosslinked with 7.5 mol% trimethylolpropane ethoxylate methyl ether diacrylate. Fluorescence area and integrated intensity are measured from six different 130 nL sized hydrogel pads on DMA, mass loss was measured from three 150 µL sized hydrogel pads polymerized in a PTFE mold. Values in the graphs are the average of the individual repetition's values normalized to the respective repetition value at 0 s irradiation. Error bars show the standard deviation of all replicates. Adapted from SEIFERMANN *et al.*[1]

As a proof-of-concept and to show that the information gained from this allows to create multi-material constructs that exhibit an irradiation time-dependent structure, three different materials were selected with rapid, slow and no visible degradation, respectively. Additionally, the materials were chosen to have both a very similar intensity and fluorescence area prior to irradiation. Utilizing the same procedure for the preparation of hydrogels on DMA, 672 hydrogels were polymerized on the DMA. The different materials thereby encoded for a hidden pattern. After polymerization, the gels were stained with Rhodamine 6G and imaged with fluorescence microscopy. The pattern was well hidden, and the different materials seemed very alike. After the first 20 min of UVC irradiation, the rapidly degrading hydrogels were completely gone, revealing the first part of the hidden message:” LONG”. Upon 40 more minutes of irradiation, the slowly degrading hydrogels were almost completely gone, too, leaving only the non-degradable gels and thereby changing the message to the second part:” LONGER” (Figure 20). This very simple experiment proves that the different degradation behavior of the materials that were discovered here can be used for simple information encoding, making them potential candidates for different applications such as the development of multi-layer, photodegradable 3D scaffolds.

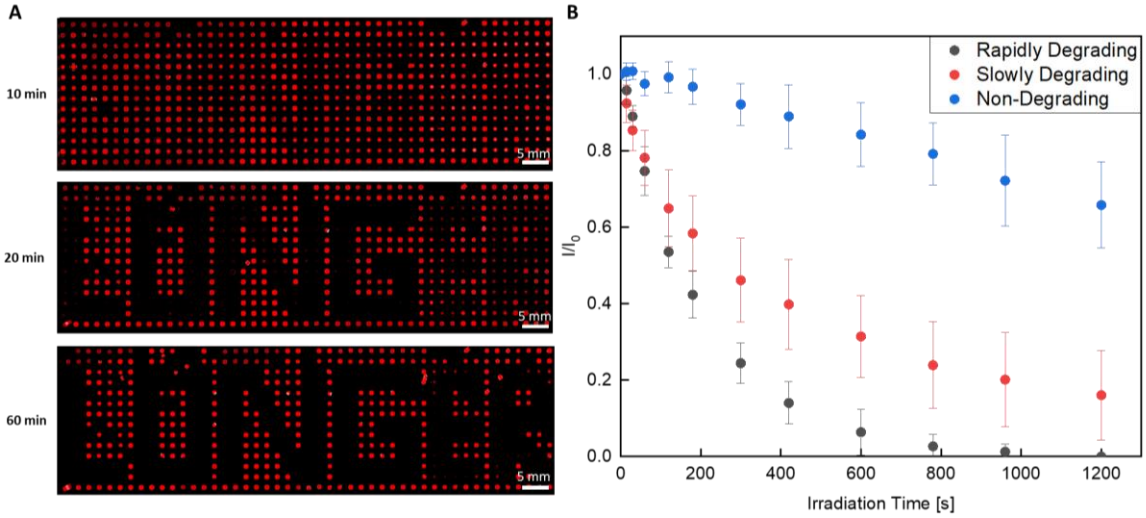

Figure 20: Encoded pattern on an array of nanoliter hydrogels, created from three different hydrogel types: Non-Degradable hydrogel based on 4-Hydroxybutyl acrylate and N,N-Methylenbisacrylamide, a slowly degradable hydrogel made of Furfuryl Methacrylate and Pentaerythritol triacrylate and a rapidly degradable hydrogel consisting of Poly(ethylene glycol)methyl ether acrylate (Mw = 500) and Glycerol Dimethacrylat. Images have been edited with Adobe Photoshop Lightroom Classic to increase Contrast for better visualization. (B) According degradation curves of the non-degradable composition, slowly degrading hydrogels and the rapidly degrading hydrogels. Values shown are measured in a miniaturized screening process and calculated as average of 6 repetitions normalized to their respective starting value. Error bars shown represent the standard deviation between these six repetitions. Adapted from SEIFERMANN *et al.*[1]

2.1.5 Bayesian Optimization

A major advantage of the application of machine learning for the interpretation of huge data sets over manual interpretation is the ability to rapidly identify correlations. This can be used to further optimize desired properties based on previous experiments. A very potent tool to perform feature optimization within the given model is the so called Bayesian optimization (BO).[108] Usually, BO is carried out iteratively, each time improving the precision of the model and filling the gaps in the data set. Applying BO, Dr. *Patrick Reisser* predicted a series of 54 new materials to further expand the property space covered within our data set. 11 different monomers and 15 different crosslinkers with varying amount of crosslinker were suggested and tested accordingly. Based on the outcome of this first optimization cycle, a second optimization run was started. Due to the broad coverage of the original screening and the first round of BO, only 25 more combinations of 8 monomers and 11 crosslinkers were proposed by the model. These two measurement cycles were added to the training set and the effect on the property space showed an increase in both high- and low populated areas of the map (Figure 21). This final application of ML in the material design once again showed the vast potential offered by the combination of ML with HT experimentation.

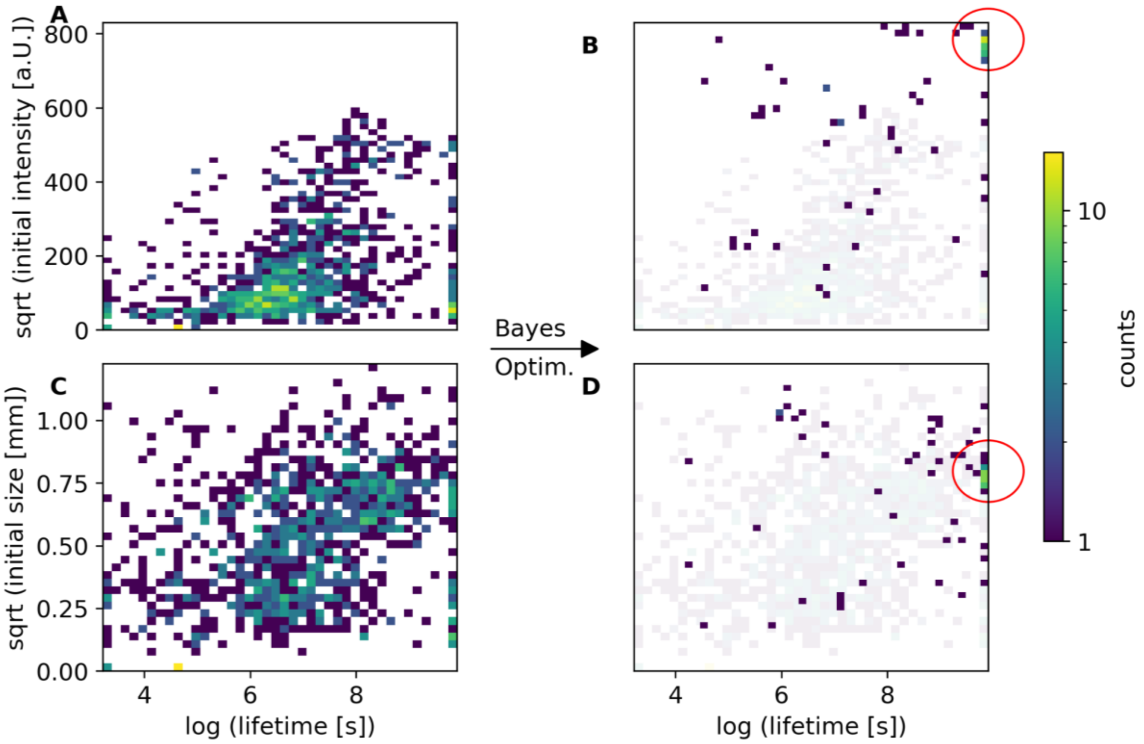

Figure 21: Distribution of all the different hydrogel properties (intensity/size) versus the degradation lifetime before and after Bayesian optimization. (A) 2D histogram of the square root of the initial measured average intensity or initial size (C) versus the fitted log-lifetime of the hydrogel under UV-irradiation. The 2D histogram after Bayesian optimization of the square root of the initial measured average intensity (B) or initial size (D) versus the fitted log-lifetime of the hydrogel. Brighter colors represent higher density indicated by a colorbar legend. On the left, the distributions of the initial, randomly selected hydrogels are shown. On the right, the distribution of experimentally measured suggestions from Bayesian optimization (both multiobjective and extremal property search) are shown (with the initial distributions in the background). Red circles in B and D highlight areas of high lifetime and intensity with multiple compositions. Adapted from Seifermann *et al.*[1]

2.1.6 Summary

In this chapter it was shown that the DMA is suitable to produce various soft materials based on radical polymerization with a sample volume of 130 nanoliter. The fabrication process is reproducible and allows the characterization of the photodegradability in a fast and parallelized fashion through fluorescence microscopy-based imaging. It has a high tolerance in terms of applicable monomers and can cover a large chemical space in a short time frame, allowing for the analysis of ~1000 different materials' photodegradability, consuming less than 800 µL of diluted stock solutions in total. The precision of the method has been assessed by comparison of values generated from a miniaturized screening of various materials with the respective materials values on a microliter scale and was shown to be very good with a relative deviation in the fitted lifetime between 2-12 %. On top of that, the miniaturized method was not only faster than the microliter approach, but also consumed roughly 574 times less material than the upscaled workflow, making it a more sustainable alternative that highly facilitates the material discovery process.

The discovered materials herein were used in a proof-of-principle experiment to show that the discovered photodegradation behaviors can be used for the encoding of information into multimaterials scaffolds. This makes them applicable in various fields, such as information storage or the creation of 3D scaffolds for cell culture or tissue engineering. The property investigated here was only exemplary and the workflow can be adjusted to include various other types of readouts such as nanoindentation for mechanical properties, cell assays for biocompatibility or fluorescence microscopy for swellability measurements.

Additionally, it was shown that the combination of the experimental workflow with ML and BO can increase the discovery speed and decrease the material consumption even further, thereby setting the path for a fast and efficient future of material science.

This proof-of-principle project, shows that the DMA is suitable for the preparation of materials and the reliable characterization of them. Continuation of this could allow design and testing of more complex materials systems, as they are required for example in tissue engineering

2.2 Cascade-Synthesis and Screening of MEK-Inhibitors on DMA

2.2.1 Introduction

2.2.1.1 Targeted Therapy and the ERK-Pathway

In 2022, a total of 9.96 million people died from cancer, globally, making it the second leading cause of death after cardiovascular diseases.[109] The disease and the accompanying need for a treatment were relevant throughout the history of humanity, but of central importance for chemical research since at least the early twentieth century when *Paul Ehrlich* started coining the term *Chemotherapy* for treatment of different infectious diseases as well as cancer using chemical compounds.[110] While in the beginning stages of modern medicine radiotherapy and surgery were the applied practice, it did not take too long for chemotherapy to become of similar or even higher relevance in treatment of different cancers. In 2018, there were estimated 17.0 million new cases of cancer of which roughly 9.8 million (58 %) required chemotherapy alone or in combination with other therapy approaches.[111] But nowadays, due to the advances in omics and personalized medicine, the development in research is moving away from non-specific therapeutics towards the use of targeted therapy.[112] In targeted therapy, the fundamental differences of seemingly alike diseases play a crucial role, as such it is important to understand the dysregulations that lead to the formation of a specific type of cancer and target that specific molecule or group of molecules to stop the tumor’s growth. This requires both a detailed insight into the mechanisms at play for the individual patient as well as a set of tools that can specifically stop the respective biological target. This leads to one of the major advantages of targeted therapy, the promise of specificity, leading to a more effective treatment of the disease as well as a reduction in abundance and severity of side effects.[113] In order to achieve the application of targeted therapy widely, an extensive set of compounds possessing the right affinity towards each potential target is required, which is an ongoing task for medicinal chemists.

There is a variety of signaling cascades and pathways that are essential for the regulation and survival of cells or organisms that all involve various different proteins. Mutations on proteins involved in these cascades can lead to dysregulation and cause various diseases, involving tumor formation, which makes those proteins potential targets. While there are many potential target proteins or signaling cascades, one of the best understood ones is the ERK-Pathway. This pathway contains a variety of prominent target proteins such as EGFR, RAS, RAF, MEK and ERK. Several receptors on the cell's surface, such as EGFR, activate RAS GTPases (KRAS, NRAS, HRAS) which leads to phosphorylation of RAF kinases (ARAF, BRAF, CRAF). These kinases' main substrates are MEK1 and MEK2 which in return phosphorylate ERK. The activation of ERK influences the gene expression, therefore interfering with cell cycle progression, differentiation, survival, apoptosis, migration and invasion (Figure 22).[114] Additionally, ERK activation causes an upregulated expression of EGFR ligands, creating an autocrine loop, promoting tumor growth.[114] The strong influence of the pathway on the survival of cells reflects in its major importance in the proliferation and phenotyping of tumors, which is further confirmed by the abundance of its dysregulation in roughly one third of all types of human cancers.[115] Due to this, the ERK-pathway has high-priority in the development of targeted therapeutics.

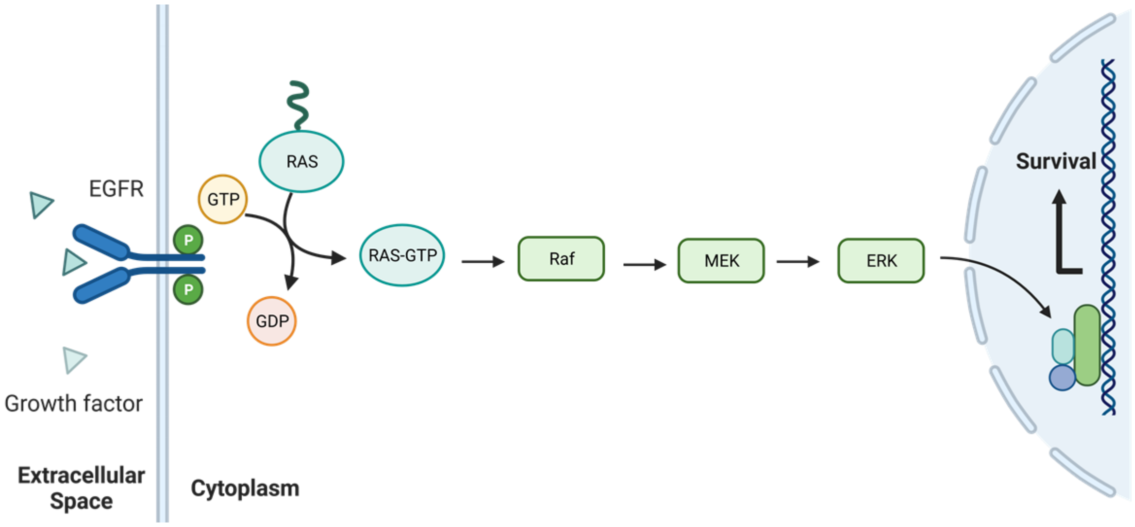

Figure 22: Schematic depiction of the ERK-signaling cascade starting from activation of RAS through EGFR, followed by subsequent phosphorylation of RAF, MEK and ERK, leading to an effect on the transcription. Figure was created with Biorender.com.

The most common approach to suppress the functionality of the enzymes involved in the cascade is the use of small-molecule inhibitors. There are several therapeutic approaches that seem promising, as a study has shown that treatment of BRAF-mutant melanoma with RAF inhibitor *Vemurafenib* could lead to a partial or total regression in the majority of all their cases.[116, 117] However, targeting upstream regulators such as RAF bears the risk of negative feedback loops, as it was observed in the treatment of BRAF-mutant colorectal cancer. Here, the inhibition of BRAF lead to an excessive activation of CRAF and RAS through the increased amounts of phosphor-EGFR, preventing the levels of phosphorylated ERK from dropping.[118] Through combination of both BRAF and EGFR inhibitors, such feedback loops could be suppressed and reduction in phosphorylated ERK could be observed, causing a positive reaction to the treatment for non-small cell lung cancer.[119] This again highlights both the advantages and challenges in the application of personalized medicine, since most of these signaling cascades are interconnected, shutting down a single protein can cause drastic changes. When the disease is fully understood those interactions can be controlled or even used for the patients benefit. For this to work, there is a dire need for a large toolbox of inhibitors to target every part of the chain specifically, to control all parts of it.

2.2.1.2 Motivation and Aim

Due to the abundance of mutations on the mitogen-activated protein kinase kinase (MEK) and its severe impact on the formation of cancer, there is a lot of research going into the development of potent inhibitors. However, in the beginning of 2021 there were only 4 MEK-inhibitors available that have FDA approval.[119] There is a common core motif for three of those inhibitors that is also present in the orphan drug MIRDAMETINIB, another potent MEK-inhibitor. (Figure 23) There are two distinct regions important for the binding in the allosteric pocket of MEK: The halogenated aniline-fragment (red) is responsible for binding in the hydrophobic pocket consisting of the four amino acids L115, L118, V127 and M143; the amide and its substituents (blue) are the part responsible for the hydrophilic interaction with K97.[120]

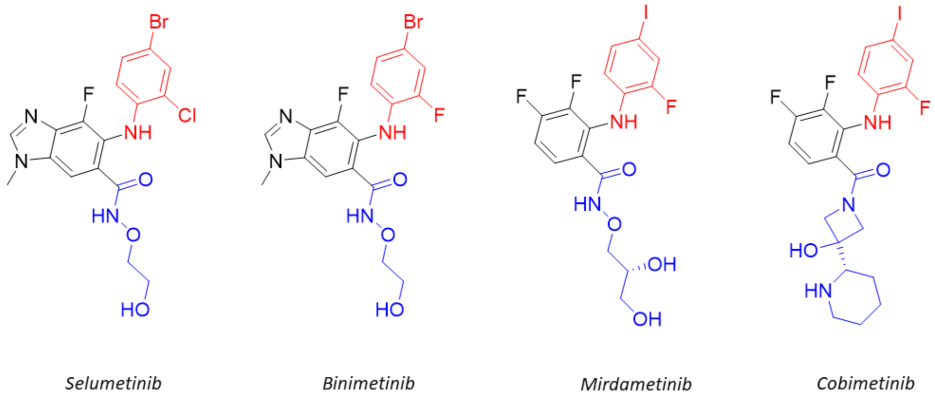

Figure 23: Chemical structures of the three FDA approved inhibitors SELUMETINIB, BINIMETINIB and COBIMITINIB as well as the structure of designated orphan drug MIRDAMETINIB. Red indicates the binding region for the hydrophobic pocket of MEK, blue shows the part binding the K97-residue.[119, 120]

These two regions can therefore be regarded as the most important parts when it comes to affinity of the ligand towards the protein, making them responsible for the potency of the inhibitor. Since MEK is known to possess a high degree of flexibility within its allosteric binding pocket, a tolerance towards slight increase or decrease in size of the substituents was assumed and a chemical scheme for the derivatization of this common core motif could be designed.[121] A solid-phase synthesis approach was chosen combining amide-coupling reactions with SUZUKI-couplings (see chapter 1.3) to achieve the derivatization of both positions of interest in a reaction cascade. This would allow to introduce non-polar substituents to the region of the molecule responsible for binding the hydrophobic pocket and additional residual groups to the carbonyl that binds K97. To conduct this, the HEMA-*co*-EDMA DMA was chosen and the spots were modified with the photolabile linker (see chapter 1.3) containing an aminogroup as anchor point. From here, the surface-amines could be converted into amides by reaction with Fmoc-protected amino acids. Upon deprotection of the Fmoc-group, the core motif of the inhibitors was to be introduced by amide-coupling of the new surface-amines with 3,4-difluoro-2-(2-fluoro-4-iodophenylamino)benzoic acid (**4**). From here, different aromatic substituents could be introduced through SUZUKI-coupling using the aryl iodide fragment and various aromatic boronic acids (Figure 24). The so generated new derivatives could be cleaved of the surface and used for a direct cell assay utilizing a cell line susceptible to MEK-inhibition to screen for their anticancer activity.

The results shown in this chapter were obtained in close collaboration with Julius Höpfner (KIT). The preparation of the substrates as well as the amidation steps and the biological on-chip screening were performed by Maximilian Seifermann (KIT). All Suzuki-couplings on-chip and in bulk, as well as the preparation of the on-chip MALDI samples after the final step of the synthesis were performed by Julius Höpfner (KIT). The experimental planning, the preparation of LC-MS samples and the dose-response measurements were performed together. The analysis of the entire raw data was done independently. Experimental work performed by Julius Höpfner is indicated as such in the following text.

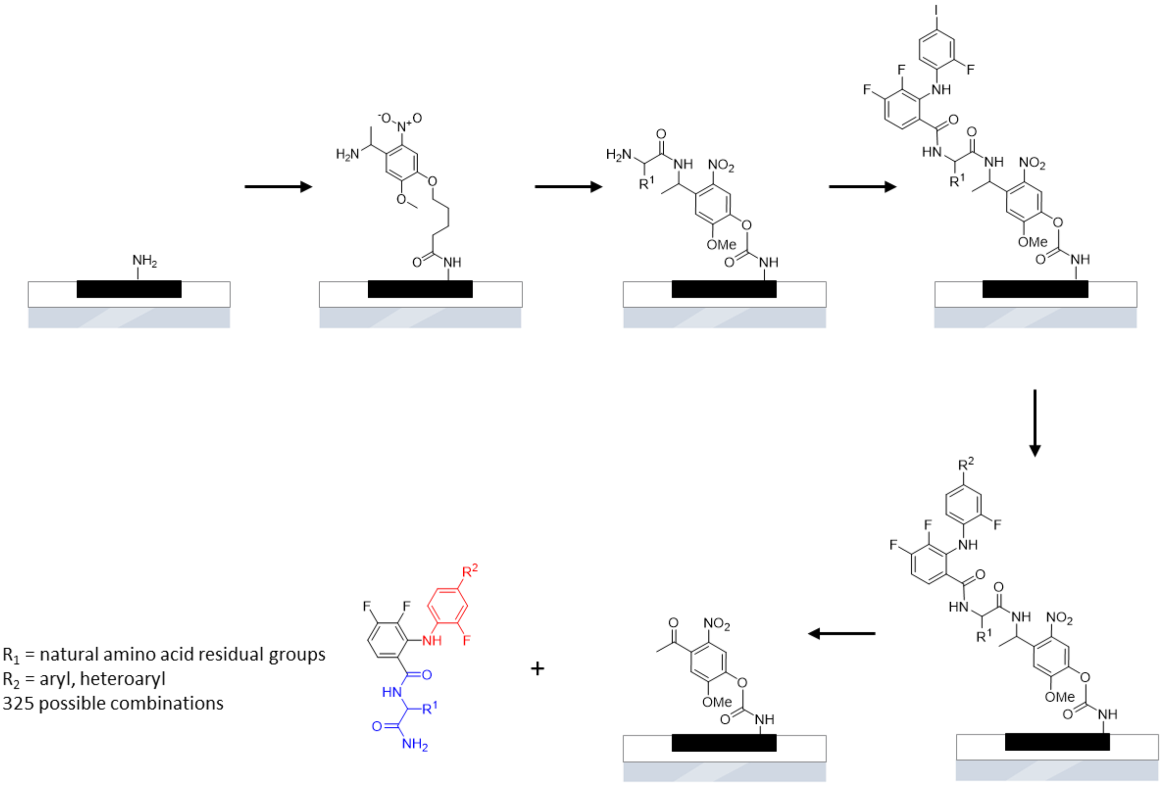
R_1 = natural amino acid residual groups
R_2 = aryl, heteroaryl
325 possible combinations

Figure 24: Synthetic route for the preparation of novel MEK-inhibitors through solid-phase using a combination of amidation and Suzuki-coupling.

2.2.2 Characterization of Surface Loading, Purity and Yield

To validate the synthetic concept, a model reaction was conducted and analyzed on a DMA with 80 round spots (diameter 2.8 mm). For this, the spot surface of the DMA was modified with an amino-group bearing photolinker, followed by the subsequent attachment of alanine and 3,4-difluoro-2-(2-fluoro-4-iodophenylamino)benzoic acid (**4**) in two separate amidation steps.

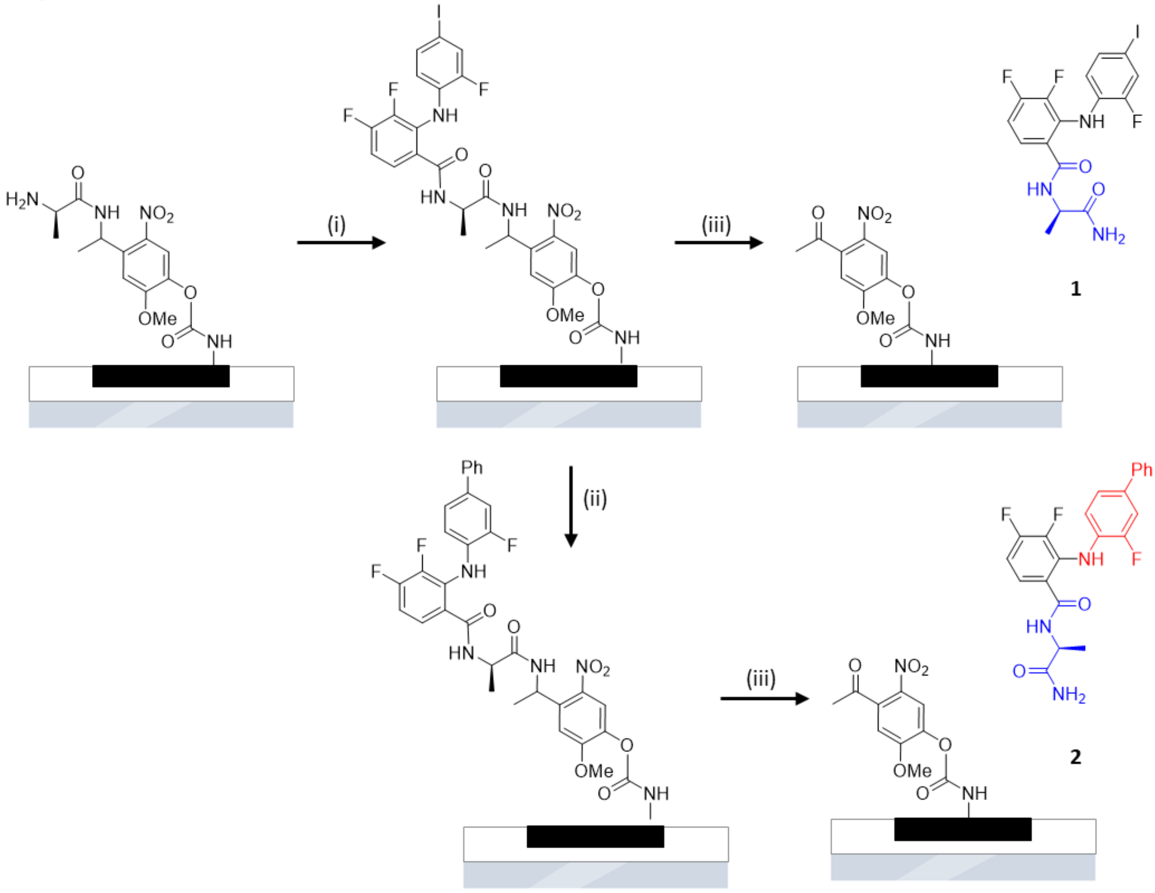

Figure 25: Preparation of intermediate **1** and final compound **2** through solid-phase synthesis on DMA: (i) 3,4-difluoro-2-(2-fluoro-4-iodophenylamino)benzoic acid (4), HOBT, DIC in NMP, 18 h; (ii) Sodium tetrachloropalladate, dibenzyl-N,N-diisopropylphosphoramidite, phenylboronic acid, sodium carbonate in NMP/Water, 18 h; (iii) UV irradiation, 40 min.

From here, the iodide is replaced with a phenyl-group through a Suzuki-coupling (Figure 25). The Suzuki-coupling step was performed by Julius Höpfner. Two samples were prepared and irradiated, one before and one after the final coupling step and both the formation of intermediate **1** and the final product **2** could be validated through LC-MS (Figure 26). As the products could be identified as clear main peak within the respective runs using the previously reported protocols, these protocols and the shown model reaction were fully adapted and used for a full characterization of the synthetic workflow.

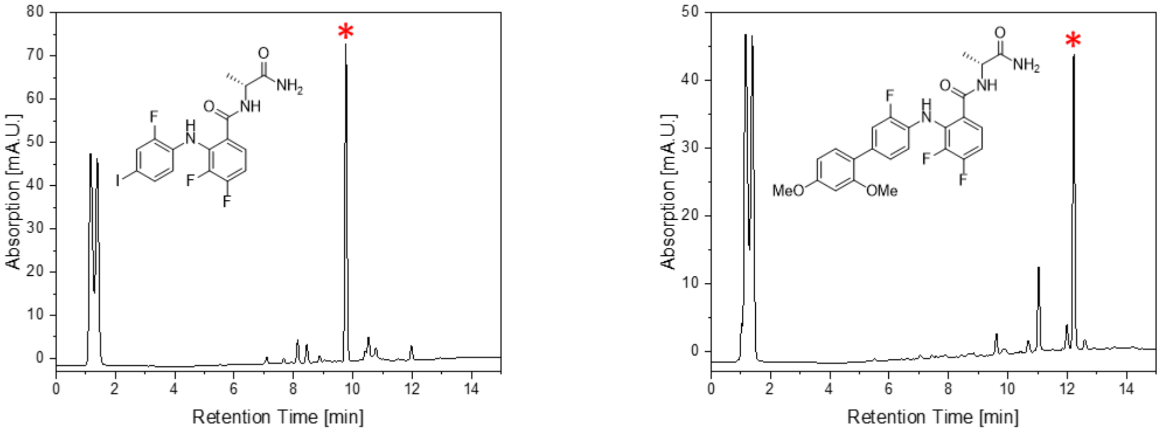

Figure 26: LC-MS chromatograms of intermediate **1** (left) and product **2** (right), obtained after solid-phase synthesis. The peak for the corresponding product is marked with a red star.

The first step to characterize was the attachment of Fmoc-protected amino acids to the photolinker, in particular the purity of the released compounds and the overall surface loading. Therefore, the surface of the DMA was first modified with the amino-photolinker, then amidated with Fmoc-alanine using DIC and HOBT as coupling reagents. After washing, the spots were irradiated for different times (7-42 min) and the amount of released Fmoc-alanine amide (**3**) was measured *via* LC-MS (Figure 27).

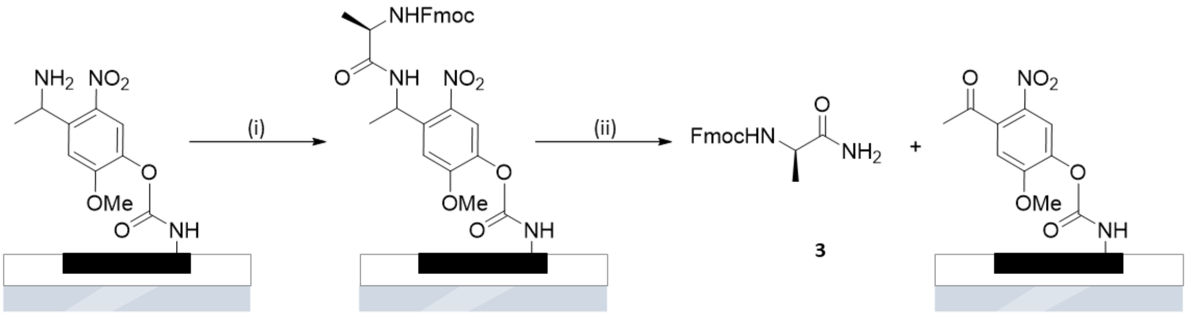

Figure 27: Surface attachment of Fmoc-alanine and release of Fmoc-alanine amide (3) for the calculation of the amino acid loading: (i) Fmoc-alanine (100 mM), DIC, HOBT in NMP, 18 h; (ii) UV irradiation, 7-42 min.

By comparison to Fmoc-alanine as standard compound the released amount of Fmoc-alanine amide was calculated. This delivered a good estimation of the cleavage progression and showed that a plateau was reached at around 35 min of irradiation (Figure 28A). For the calculation of conversion rates of the subsequent reaction steps, a product loading of 160 pmol/mm^2 was used. The observable purity under these conditions was calculated from the LC-MS chromatogram to be around 81%.

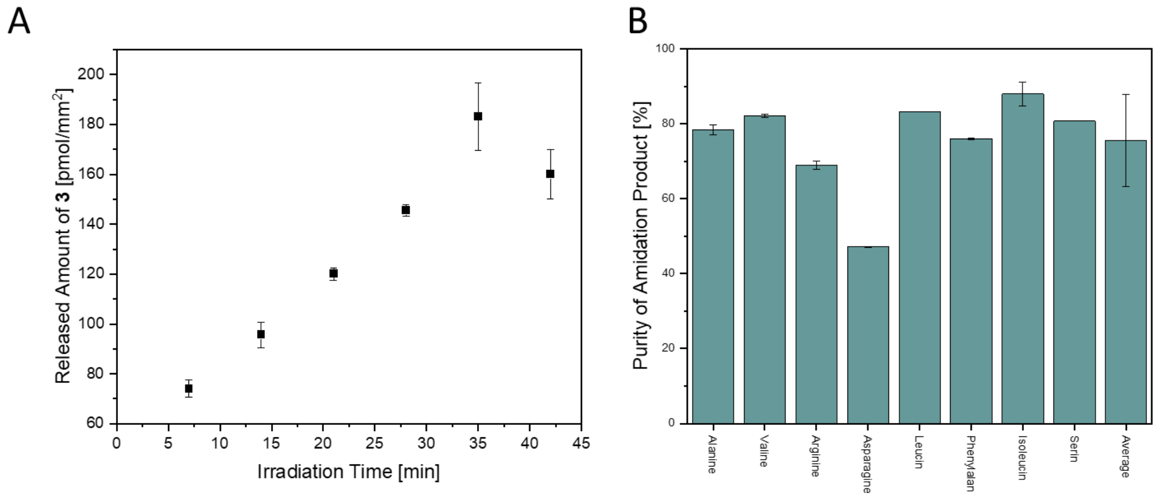

Figure 28: (A) Released amount of Fmoc-alanine amide (3) from a surface modified with Fmoc-alanine (100 mM) with respect to the irradiation time. (B) Purity of amidation product between 3,4-difluoro-2-(2-fluoro-4-iodophenylamino)benzoic acid (4) and eight different amino acids immobilized on the hydrophilic surface of a DMA after UV-induced cleavage. Purity was calculated *via* LC-MS as integration value of the product peak divided by the sum of all peak integration values. Measurements were performed in triplicates, error bars show the standard deviation.

The next step was to validate that the formation of the amidation product for the reaction of 3,4-difluoro-2-(2-fluoro-4-iodophenylamino)benzoic acid (**4**) occurred independently from the applied surface-bound amino acid. For this, spots modified with 8 different amino acids were prepared as described above. After Fmoc-deprotection with piperidine in DMF (20%, v/v) for 30 min, all immobilized amino acids were treated with a solution of 3,4-difluoro-2-(2-fluoro-4-iodophenylamino)benzoic acid (**4**) (100 mM), supplemented with HOBT (100 mM) in a mixture of DMF and DIC (9:1, v/v). After 18 h, the surface was cleaned and irradiated with UV light for 40 min. The released compounds were analyzed *via* LC-MS and the product formation could be proven for all amino acids. Additionally, the purity of each compound as well as the average purity were calculated (Figure 28B).

To calculate the conversion rates and the amount of formed product for subsequent reactions, compounds **1** and **2** were prepared in flask as standard compounds (Figure 29). Compound **2** was prepared by JULIUS HÖPFNER.

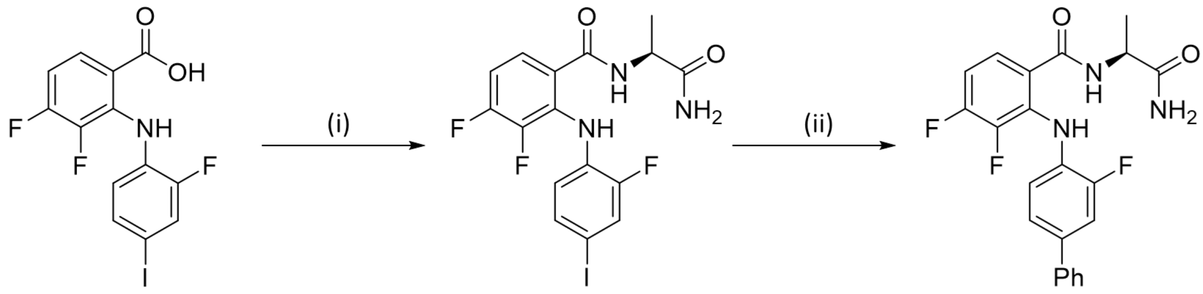

4 **1** **2**

Figure 29: Preparation of standard compounds 1 and 2 in flask: (i) Alanine amide hydrochloride, *N*-ethyl-*N'*-3-dimethylaminopropyl carbodiimide, *N*-Methylmorpholine, HOBT in DMSO, 16 h at rt; (ii) Phenyl boronic acid, palladium acetate, triphenylphosphine, sodium carbonate in THF/Water, 16 h at 80 °C.

Then, a DMA modified with photolinker (100 mM) and alanine (100 mM) was prepared according to the previously described conditions and then reacted with acid **4**. After the reaction was complete, the supernatant was washed off and the DMA was irradiated to release compound **1**. The released amount of compound **1** was measured *via* LC-MS and calculated to be 122±16 pmol/mm^2, leading to a conversion rate of about 76 % for the second amidation step.

For the characterization of the final step, the Suzuki-coupling, the same eight amino acids used for the purity measurements were bound to the surface and modified with acid **4**, afterwards they were coupled with two different boronic acids: phenylboronic acid and 2,5-dimethoxyphenyl boronic acid. The Suzuki-coupling step was performed by Julius Höpfner. After the reaction, precipitated palladium was dissolved using potassium cyanide solution and the surface-tethered product was again released through UV-induced cleavage. The released compounds were analyzed *via* LC-MS to identify the products and their purity as well as calculate a conversion rate (Table 1). The products of the reactions could be identified for all 16 combinations with mostly minor differences in purity and conversion rate for the two different boronic acids. However, the influence of the amino acids seems more impactful as the purity ranged between 35-68 %, depending on the reaction. The average conversion rate was calculated to be 86 %, the average purity 65 %, which both were deemed sufficient to proceed.

Table 1: Conversion rates and purity of the final products obtained by the reaction sequence involving 8 different amino acids and 2 different boronic acids. Purity is calculated as ratio of the product peak integral to the total integration value of all peaks. Conversion rate is calculated as ratio of the product peak integral to the sum of product peak integral and starting material peak integral.

Aminoacid	Boronic Acid	Purity [%]	Conversion [%]
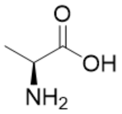	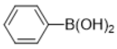	58	83
	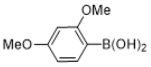	58	83
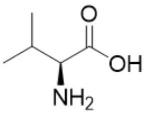	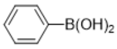	62	86
	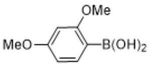	49	79
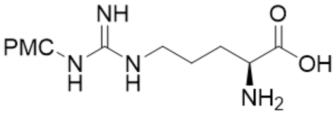	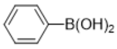	66	92
	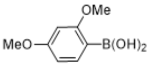	60	>99
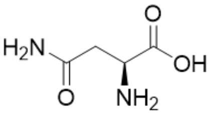	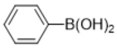	35	>99
	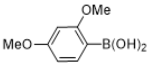	37	>99
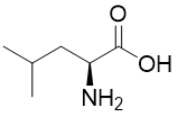	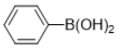	64	90
	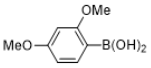	39	79
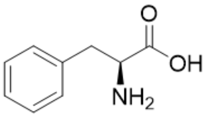	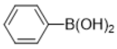	48	72
	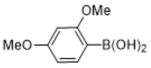	54	>99
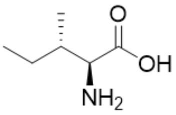	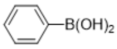	68	87
	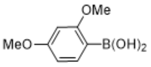	52	83
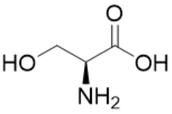	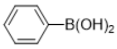	65	86
	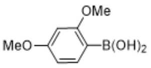	45	65
	Total	65	86

With the general performance of the synthesis being evaluated, the controlled product release needed to be optimized. As the aim was to develop a pipeline that allowed not only preparation of the compounds, but *in-situ* testing of these compounds as well, gaining control over the product release was crucial. For inhibitors, the relation between activity and concentration is very simple and is described by a dose-response curve. For too low concentrations, there is no visible effect on the enzyme and therefore on the cell, for too high concentrations there is the risk of general toxicity. To avoid both these cases, the desired concentration range was chosen to be at around 10 µM, which is generally regarded as a good concentration range for primary screenings.[122] To achieve this comparably low concentration, the amount of substance that was released in the end needed to be reduced. Since it was important not to increase the impurity through remaining intermediates, the only two ways to achieve this were to reduce the number of binding sites prior to the reaction sequence or to cleave only a fraction of the final products off the solid phase.

Since it is known that the number of binding sites is related to the concentration of the solution with which the photolinker is bound to the surface, a quick screening with a static irradiation time of 40 min was performed to see at which concentration range suitable amounts of product would be released. The formation of intermediate **1** was chosen as a model reaction again to screen for suitable conditions and the theoretical final concentration achievable in an assay at a volume of 1 µL per spot was calculated from that with the average SUZUKI conversion rate of 86 %. The photolinker modification solution was used at concentrations between 0.3 and 100 mM and the amount of product was calculated using LC-MS (Figure 30).

Noticeably, there was no significant difference in product formation between 2 and 100 mM, however, below 2 mM there was a rapid decrease. The lowest concentration tested, 0.1 mM, led to a final release of compound **1** at about 10 pmol/mm^2 and a corresponding assay concentration of 10 µM. To validate this, a control experiment was performed and the surface was again modified with 0.1 mM photolinker solution, then the full reaction cascade was conducted and the amount of final product **2** was measured.

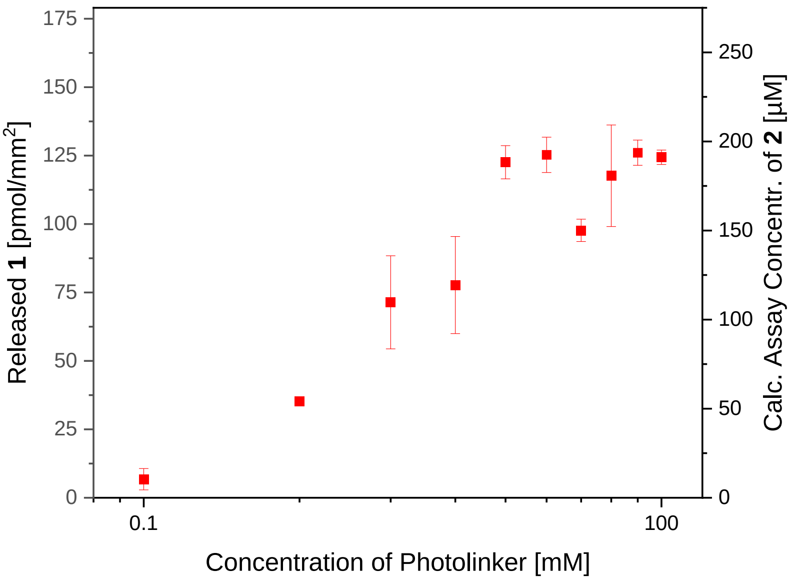

Figure 30: Surface loading of 1 and theoretical assay concentration of 2 depending on the concentration of the photolinker modification solution. Error bars show the standard deviation of three independent experiments.

The results showed a final release of **2** of about 6.31±0.14 pmol/mm^2 which leads to an assay concentration of **2** at about 9.71±0.22 µM. This confirmed that the synthetic conditions were suitable to achieve the desired final concentration.

2.2.3 Reaction Conformation through MALDI-TOF-MS

To confirm the product formation for a wide set of compounds, individual LC-MS analysis is not suitable under the applied conditions. An alternative approach was direct mass spectrometry of the crude mixture after release off the solid phase without chromatographic separation. An analysis often carried out in HT experimentation is MALDI-TOF-MS. To analyze a library of compounds with MALDI-TOF-MS, two HEMA-*co*-EDMA DMAs with 320 round spots (diameter 1.4 mm) were prepared and modified with 100 mM photolinker solution. On each of these DMAs the same 320 reactions were carried out using 13 different amino acids and 25 different boronic acids as reactants, with a total volume of 300 nL and 400 nL in the binding of acid **4** and the SUZUKI-coupling step, respectively. The SUZUKI-coupling reaction was performed by JULIUS HÖPFNER. Afterwards, the slides were cleaned and irradiated for 40 min to cleave the compounds off the solid phase. These compounds were manually redissolved in 1 µL of a DMF/Water mixture (3:1, v/v) and transferred to a ground steel target plate. The plate was spray coated with *N*-(1-naphthyl)ethylendiamine dihydrochloride (NEDC) as the matrix for the ionization and afterwards analyzed on a rapifleX MALDI-TOF system (Bruker, Bremen, Germany) by Dr. STEFAN SCHMIDT (CeMOS) in negative ion mode to record mass spectra of each individual spots content (Figure 31). These mass spectra were analyzed for the presence of the most characteristic adducts ([M-H]$^-$, [M+Cl]$^-$, [M-H$_3$O]$^-$, [M+Na-2H]$^-$). Out of the 320 analyzed compounds, 298 could be clearly identified, leading to a synthetic success rate of about 93 % (Table 1).

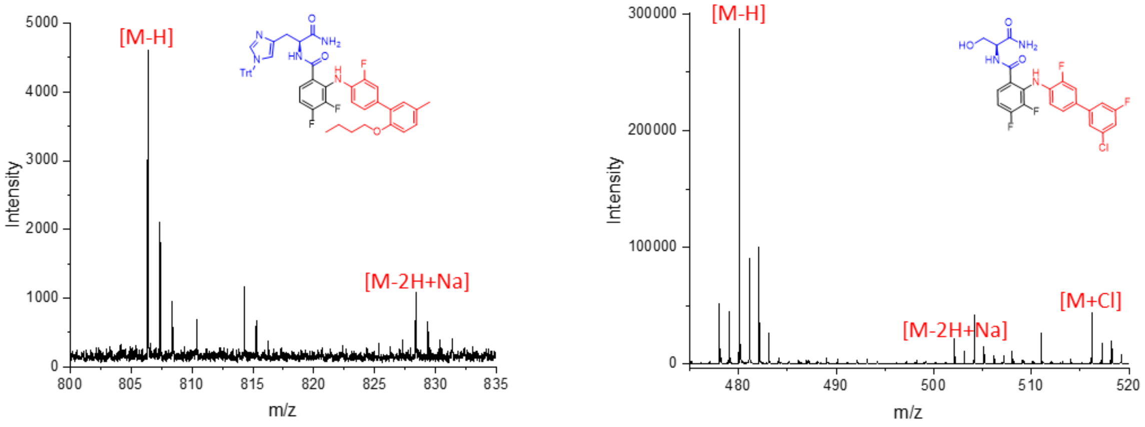

Figure 31: Exemplary MALDI-mass spectra recorded on a ground steel target plate and respective structures for two compounds synthesized on 1.4 mm spots of a DMA.

To increase the throughput of the method further, the synthesis and analysis could be conducted without an additional transfer step in between. Since MALDI-TOF-MS requires a conductive substrate, the standard DMA based on a glass substrate is not compatible. To overcome this, ITO-coated glass slides can be allowed to create a conductive foundation that can be functionalized in the same fashion as a common glass slide. Two of these ITO-DMAs were prepared and modified with 1152 round spots (diameter 900 µm). In these spots, the same reaction sequence was carried out using the same 13 amino acids and 25 boronic acids to generate 325 possible combinations in triplicates for a total of 975 reactions with a reaction volume of 100 nL and 200 nL in the attachment of acid **4** and the SUZUKI-coupling, respectively. The SUZUKI-coupling was performed by JULIUS HÖPFNER.

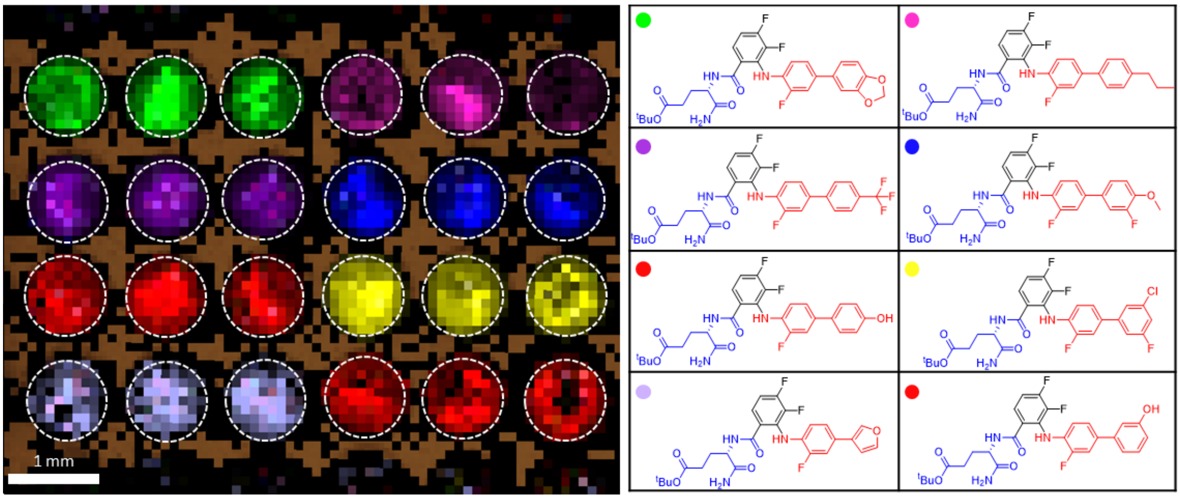

Figure 32: MALDI-MS imaging of an ITO-DMA modified with 900 µm spots in which solid-phase synthesis was carried out. Colors indicate the intensity of the [M-H]- ion for 7 different chemical formulas. Target structures with the color of their [M-H]- peak are given.

After cleavage off the solid phase, a solution of NEDC was added to each spot and the solvent was evaporated to co-crystalize the matrix with the sample. Afterwards, the sample was measured again with a rapifleX MALDI-TOF system (Bruker, Bremen, Germany) in imaging mode by Dr. STEFAN SCHMIDT (CeMOS, Mannheim) (Figure 32). In this experiment, 261 of 325 compounds (82 %) could be identified clearly (Table 2). Due to the polymer layer on top of the ITO-coating, the conductivity was reduced, leading to a weaker ionization and therefore a generally lower intensity. This affected especially the compounds containing larger building blocks (e.g., A4) or less ionizable building blocks (e.g., B17). However, as the identification rate was still high, the throughput was increased compared to the previous experiments and the imaging visualized the confinement of the target compounds to the individual spots.

Table 2: Identification rate of final products in MALDI-TOF-MS regarding each tested building block for measurements on ground steel target plate (MTP) and ITO-DMA, respectively.

No.	Structure	Found on MTP (%)	Found on DMA (%)	No.	Structure	Found on MTP (%)	Found on DMA (%)	No.	Structure	Found on MTP (%)	Found on DMA (%)
A1	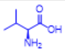	84	88	B1	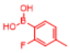	100	92	B14	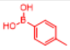	100	92
A2	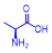	88	92	B2	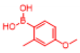	92	85	B15	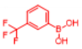	100	85
A3	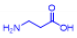	96	84	B3	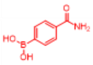	85	92	B16	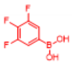	100	92
A4	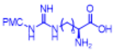	56	4	B4	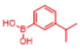	100	77	B17	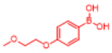	77	54
A5	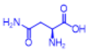	92	96	B5	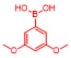	92	77	B18	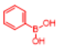	54	54
A6	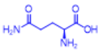	100	96	B6	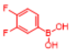	92	92	B19	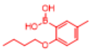	100	77
A7	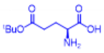	100	64	B7	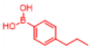	100	77	B20	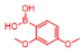	100	85
A8	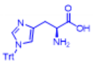	100	64	B8	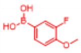	100	92	B21	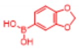	100	92
A9	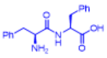	100	80	B9	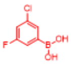	100	92	B22	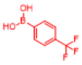	100	92
A10	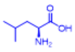	100	80	B10	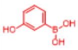	92	92	B23	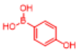	85	62
A11	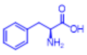	100	84	B11	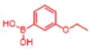	100	85	B24	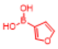	62	77
A12	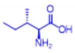	96	88	B12	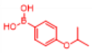	100	85	B25	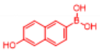	77	15
A13	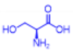	96	92	B13	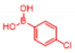	92	92	Total		93	81

To further prove that the identified signals in the mass spectra refer to the target compounds, an additional analysis step was required. Because standard analytics like nuclear magnetic resonance spectroscopy (NMR) require higher amounts of substance, tandem mass spectrometry (MS/MS) was chosen for this purpose to gain additional analytical information while not needing to increase the sample size. Out of the samples on the ground steel plate, 5 compounds were measured by Dr. STEFAN SCHMIDT (CeMOS) using a solariX Fourier-transform ion cyclotron resonance (FT-ICR) system (Bruker, Bremen, Germany). The identified [M-H]$^-$ peaks were isolated (± 2 Da) and fragmented with a fragmentation voltage of about 20 eV. The recorded spectra were compared with predicted spectra and were in good accordance, further confirming the formation of the target molecules (Figure 33).[123]

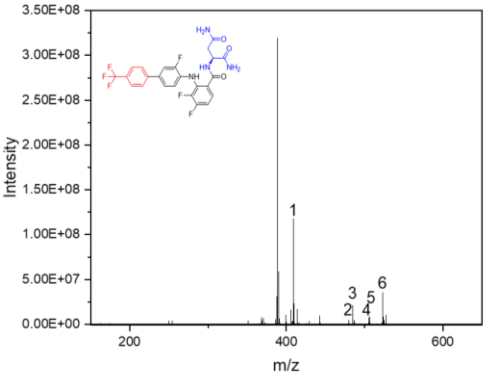

No.	m/z (Calc.)	m/z (Found)	Fragment	No.	m/z (Calc.)	m/z (Found)	Fragment
1	409.0781059	409.078106	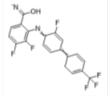	4	505.1104686	505.09857	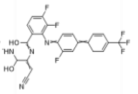
2	480.1152197	480.161571	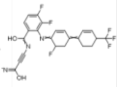	5	506.0944842	506.943538	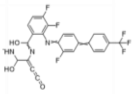
3	485.1042404	485.094032	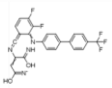	6	523.1210333	523.108686	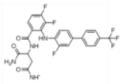

Figure 33: One Example of the five recorded MS/MS fragmentation spectra. The target compound's structure is given in the spectrum, the numbers in the spectrum reflect the respective fragments. Their exact mass and structure are given in the table on the right.

2.2.4 Optimization of Cell Culture

For the primary screening of inhibitors, cellular assays are widely applied. A cell line that is heavily affected by MEK-inhibition are human colon cancer cells HT-29, where inhibition through MIRDAMETINIB can induce cell cycle arrest and apoptosis.[124] To apply this, the culture of HT-29 cells on the modified surface of the DMA needed to be optimized and combined with a compatible readout. A possible readout that gives information about the number of living cells was the use of tetrazolium salts like in cell counting kit-8 (CCK8, Figure 34. These salts are mitochondrially metabolized into colorful formazan dyes that can be colorimetrically detected. Since this only gives information about the number of living cells in the sample, this inseparately contains both the information about proliferation of the cells as well as the cell death.

Using the absolute color intensity as a readout, the number of living cells in a sample can be calculated in a fast and parallel manner. To ensure that the readout works efficiently, the working range of initially seeded cells needs to be defined. For this, two criteria are important: the overall color intensity needed to be maximized in order to reduce the influence of noise on the signal, but also the overall intensity must not lead to signal saturation. In order to find those conditions, different DMAs with 320 round spots (diameter 1.4 mm) were prepared and modified with photolinker solution with the concentration between 0 and 100 mM.

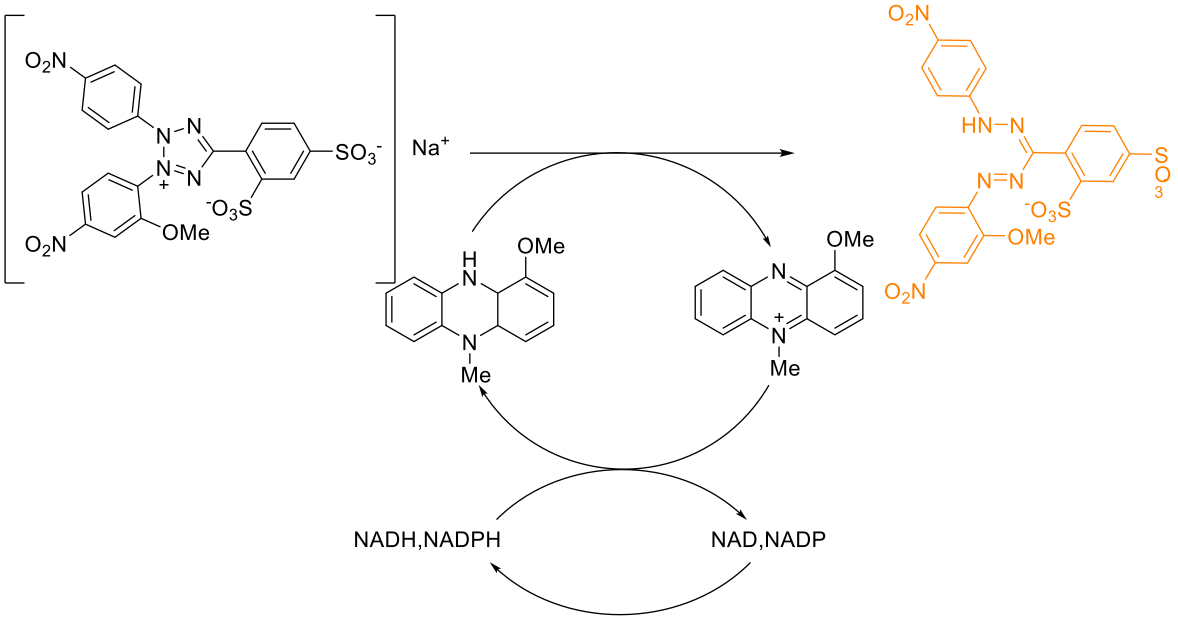

Figure 34: Cell mediated reduction of the tetrazolium salt in cell counting kit-8 to the colored formazan dye through NADH/NADPH dehydrogenation.

The slides were irradiated for 20 min with UV-light and then washed to remove any impurities. Then, 1 µL HT-29 cell suspension in *Dulbecco's modified eagle medium* (DMEM) (supplemented with Penicillin/Streptomycin, 0.1 % (v/v), and fetal bovine serum, 10 % (v/v)) was added to each spot with the number of cells per spot ranging from 0 to 400. These slides were incubated at 37 °C for 72 h, then 100 nL CCK8 were added, and the slide was again incubated at 37 °C for 1 h. The slides were then imaged using a photoscanner and the images were analyzed for the intensity of the orange color (Figure 35A). While there was a clear linear increase with a visible plateau for the moderately high concentrations of photolinker (Figure 35B), low concentrations of photolinker led to a rapid saturation, while high concentrations showed only very poor color development. This indicates that high photolinker content on the surface impacts the cellular proliferation. In addition to this, the absolute color intensity reached at the plateau showed a high variance, changing from 0.2 to 1.0 in different experiments. This is possibly due to the low number of cells initially seeded, which can lead to a non-statistical distribution of the cells to the different metabolic states, thereby impacting the metabolism of the dye. Due to this, this colorimetric readout was regarded as not suitable for a stable assay under the applied conditions.

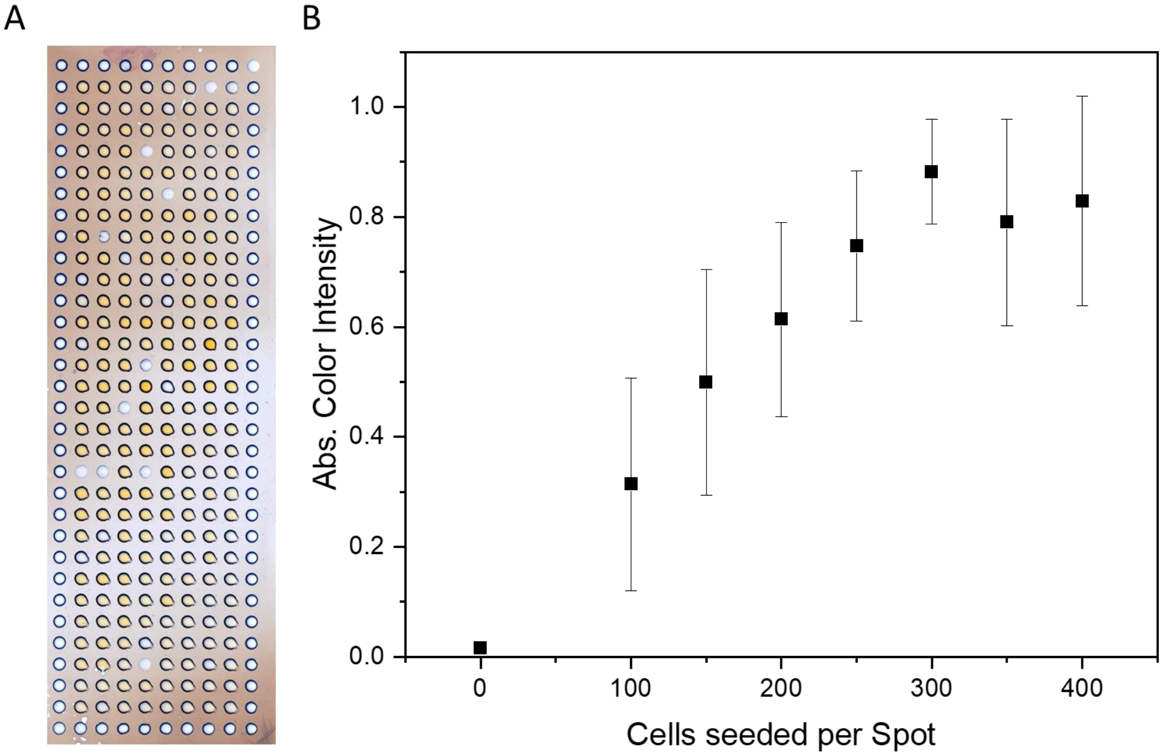

Figure 35: (A) Scanning image of a DMA modified with different amounts of photolinkers after culture of HT-29 cells for 72 and CCK8 assay. The layout was randomized. (B) Color Intensity of HT-29 cells seeded onto the hydrophilic spots of a DMA, modified with oxidized photolinker surface-groups in a CCK8 assay. A linear increase can be observed in the beginning, reaching a plateau at around 300 cells per spot. Error bars show the standard deviation of 6 replicates randomly placed over the whole slide.

As an alternative readout method that is less susceptible to changes in the cellular metabolism states, fluorescence microscopy was chosen. The focus was shifted from the number of cells alive to the number of cells dead and therefore to induced apoptosis. There are many widely used stains for this, and a common approach is to determine the cellular viability as the ratio of living cells to the total number of cells. Due to the growth behavior of the chosen cell type however, viability measurement is very difficult since the living cells grow in inseparable clusters making it difficult to determine the number of different cells embedded. To work around this problem, the number of dead cells was measured. These dead cells detach from the clusters and are present as isolated points which are easily quantified with fluorescence microscopy (Figure 36A). To visualize them, the cells were treated with propidium iodide (PI), a non-permeable dye that exhibits fluorescence upon intercalation into the DNA double strand and therefore selectively stains dead cells with a ruptured cell membrane.

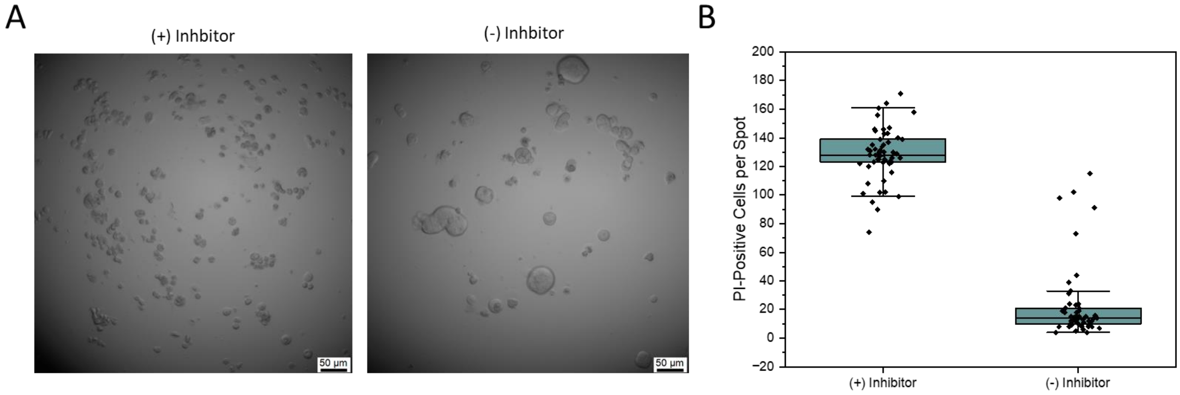

Figure 36: (A) Brightfield microscopy images of HT-29 cells seeded with the same density on a DMA modified with oxidized photolinker surface groups after incubation for 72 h with *Mirdametinib* (+) or without addition of an inhibitor (-). (B) Boxplot of the number of PI-positive HT-29 cells per spot seeded on a DMA modified with oxidized photolinker surface groups after incubation for 72 h with *Mirdametinib* (+) or without addition of an inhibitor (-). Each experiment contains the information of 120 replicates.

To assure that the PI-staining was a viable readout, the positive control containing HT-29 cells (300 cells per spot) and Mirdametinib (10 µM+0.1 v/v% DMSO) and the negative control containing HT-29 cells (300 cells per spot) and no inhibitor (+ 0.1 v/v% DMSO) were prepared on a DMA with 320 round spots. Each control was prepared with 120 replicates to see any statistical effects occurring. After 72 h incubation, the cells were stained with PI and imaged with fluorescence microscopy. The number of dead cells per spot was calculated and plotted as Boxplot (Figure 36B). The negative control showed an average number of dead cells per spot at around 20 with a narrow distribution and only 5-7 outliers, possibly caused by cross contamination during the printing step. The positive control showed an average value of around 130 PI-positive cells per spot and a wider distribution, however the difference between the controls should enable this method as a compatible readout for a primary screening. Therefore, PI-staining was regarded as method of choice and used for the actual screening.

2.2.5 Biological Screening

To conduct a primary screening of the potential MEK-inhibitors, the library was split into five parts and these were prepared on five DMAs with 320 spots (diameter 1.4 mm). The spots were modified with photolinker solution (0.1 mM) and the reaction was then carried out with a total volume of 300 nL and 240 nL per spot in the amidation and *Suzuki*-coupling steps, respectively. The Suzuki-coupling was performed by Julius Höpfner. For the preparation, a randomized layout was chosen, each slide contained 25 to 75 different compounds in triplicates as combinations of one to three amino acids and 25 boronic acids and a total of 20 spots without further modifications for positive and negative controls. After the reactions were carried out and the precipitated palladium was removed, the slides were washed and sterilized with an ethanol/water mixture (70:30) for 30 min. The slides were dried and 700 nL of DMEM (supplemented with Penicillin/Streptomycin, 0.1 % (v/v) and DMSO, 0.14 % (v/v)) were added to the compound containing spots and 10 of the empty spots. To the remaining 10 empty spots, 350 nL of DMEM (supplemented with Penicillin/Streptomycin, 0.1 % (v/v) and DMSO, 0.14 % (v/v)) were added. The slides were sealed in a petri dish containing 2 mL phosphate buffered saline (PBS) and then irradiated with UV-light for 40 min. To the spots containing only 350 nL medium, 350 nL of a solution of MIRDAMETINIB (28.6 µM) in DMEM (supplemented with Penicillin/Streptomycin, 0.1 % (v/v) and DMSO, 0.14 % (v/v)) were added. The slides were preincubated at 37 °C for 18 h to dissolve the compounds out of the polymer layer and then 300 nL HT-29 cell suspension ($1 \cdot 10^6$ cells/mL) in DMEM (supplemented with Penicillin/Streptomycin, 0.1 % (v/v) and FBS, 30 % (v/v)) were added to each spot. The slides were incubated for 72 h and then stained with PI and imaged with fluorescence microscopy.

Table 3: Identifiers of all possible MEK-inhibitor molecules with the respective amino acid (A) and boronic acid (B) used for the preparation of the compound on DMA.

Inhibitor-No.	A	B	Inhibitor-No.	A	B	Inhibitor-No.	A	B	Inhibitor-No.	A	B	Inhibitor-No.	A	B
1	1	1	71	3	21	141	6	16	211	9	11	281	12	6
2	1	2	72	3	22	142	6	17	212	9	12	282	12	7
3	1	3	73	3	23	143	6	18	213	9	13	283	12	8
4	1	4	74	3	24	144	6	19	214	9	14	284	12	9
5	1	5	75	3	25	145	6	20	215	9	15	285	12	10
6	1	6	76	4	1	146	6	21	216	9	16	286	12	11
7	1	7	77	4	2	147	6	22	217	9	17	287	12	12
8	1	8	78	4	3	148	6	23	218	9	18	288	12	13
9	1	9	79	4	4	149	6	24	219	9	19	289	12	14
10	1	10	80	4	5	150	6	25	220	9	20	290	12	15
11	1	11	81	4	6	151	7	1	221	9	21	291	12	16
12	1	12	82	4	7	152	7	2	222	9	22	292	12	17
13	1	13	83	4	8	153	7	3	223	9	23	293	12	18
14	1	14	84	4	9	154	7	4	224	9	24	294	12	19
15	1	15	85	4	10	155	7	5	225	9	25	295	12	20
16	1	16	86	4	11	156	7	6	226	10	1	296	12	21
17	1	17	87	4	12	157	7	7	227	10	2	297	12	22
18	1	18	88	4	13	158	7	8	228	10	3	298	12	23
19	1	19	89	4	14	159	7	9	229	10	4	299	12	24
20	1	20	90	4	15	160	7	10	230	10	5	300	12	25
21	1	21	91	4	16	161	7	11	231	10	6	301	13	1
22	1	22	92	4	17	162	7	12	232	10	7	302	13	2
23	1	23	93	4	18	163	7	13	233	10	8	303	13	3
24	1	24	94	4	19	164	7	14	234	10	9	304	13	4
25	1	25	95	4	20	165	7	15	235	10	10	305	13	5
26	2	1	96	4	21	166	7	16	236	10	11	306	13	6
27	2	2	97	4	22	167	7	17	237	10	12	307	13	7
28	2	3	98	4	23	168	7	18	238	10	13	308	13	8
29	2	4	99	4	24	169	7	19	239	10	14	309	13	9
30	2	5	100	4	25	170	7	20	240	10	15	310	13	10
31	2	6	101	5	1	171	7	21	241	10	16	311	13	11
32	2	7	102	5	2	172	7	22	242	10	17	312	13	12
33	2	8	103	5	3	173	7	23	243	10	18	313	13	13
34	2	9	104	5	4	174	7	24	244	10	19	314	13	14
35	2	10	105	5	5	175	7	25	245	10	20	315	13	15
36	2	11	106	5	6	176	8	1	246	10	21	316	13	16
37	2	12	107	5	7	177	8	2	247	10	22	317	13	17
38	2	13	108	5	8	178	8	3	248	10	23	318	13	18
39	2	14	109	5	9	179	8	4	249	10	24	319	13	19
40	2	15	110	5	10	180	8	5	250	10	25	320	13	20
41	2	16	111	5	11	181	8	6	251	11	1	321	13	21
42	2	17	112	5	12	182	8	7	252	11	2	322	13	22
43	2	18	113	5	13	183	8	8	253	11	3	323	13	23
44	2	19	114	5	14	184	8	9	254	11	4	324	13	24
45	2	20	115	5	15	185	8	10	255	11	5	325	13	25
46	2	21	116	5	16	186	8	11	256	11	6			
47	2	22	117	5	17	187	8	12	257	11	7			
48	2	23	118	5	18	188	8	13	258	11	8			
49	2	24	119	5	19	189	8	14	259	11	9			
50	2	25	120	5	20	190	8	15	260	11	10			
51	3	1	121	5	21	191	8	16	261	11	11			
52	3	2	122	5	22	192	8	17	262	11	12			
53	3	3	123	5	23	193	8	18	263	11	13			
54	3	4	124	5	24	194	8	19	264	11	14			
55	3	5	125	5	25	195	8	20	265	11	15			
56	3	6	126	6	1	196	8	21	266	11	16			
57	3	7	127	6	2	197	8	22	267	11	17			
58	3	8	128	6	3	198	8	23	268	11	18			
59	3	9	129	6	4	199	8	24	269	11	19			
60	3	10	130	6	5	200	8	25	270	11	20			
61	3	11	131	6	6	201	9	1	271	11	21			
62	3	12	132	6	7	202	9	2	272	11	22			
63	3	13	133	6	8	203	9	3	273	11	23			
64	3	14	134	6	9	204	9	4	274	11	24			
65	3	15	135	6	10	205	9	5	275	11	25			
66	3	16	136	6	11	206	9	6	276	12	1			
67	3	17	137	6	12	207	9	7	277	12	2			
68	3	18	138	6	13	208	9	8	278	12	3			
69	3	19	139	6	14	209	9	9	279	12	4			
70	3	20	140	6	15	210	9	10	280	12	5			

A primary screening round of all possible 325 compounds revealed a large portion of the tested molecules had no significant effect on the survival of HT-29 cells. However, for compounds containing alanine (**A2**) or beta-alanine (**A3**) showed a drastic increase in cell death (Figure 37).

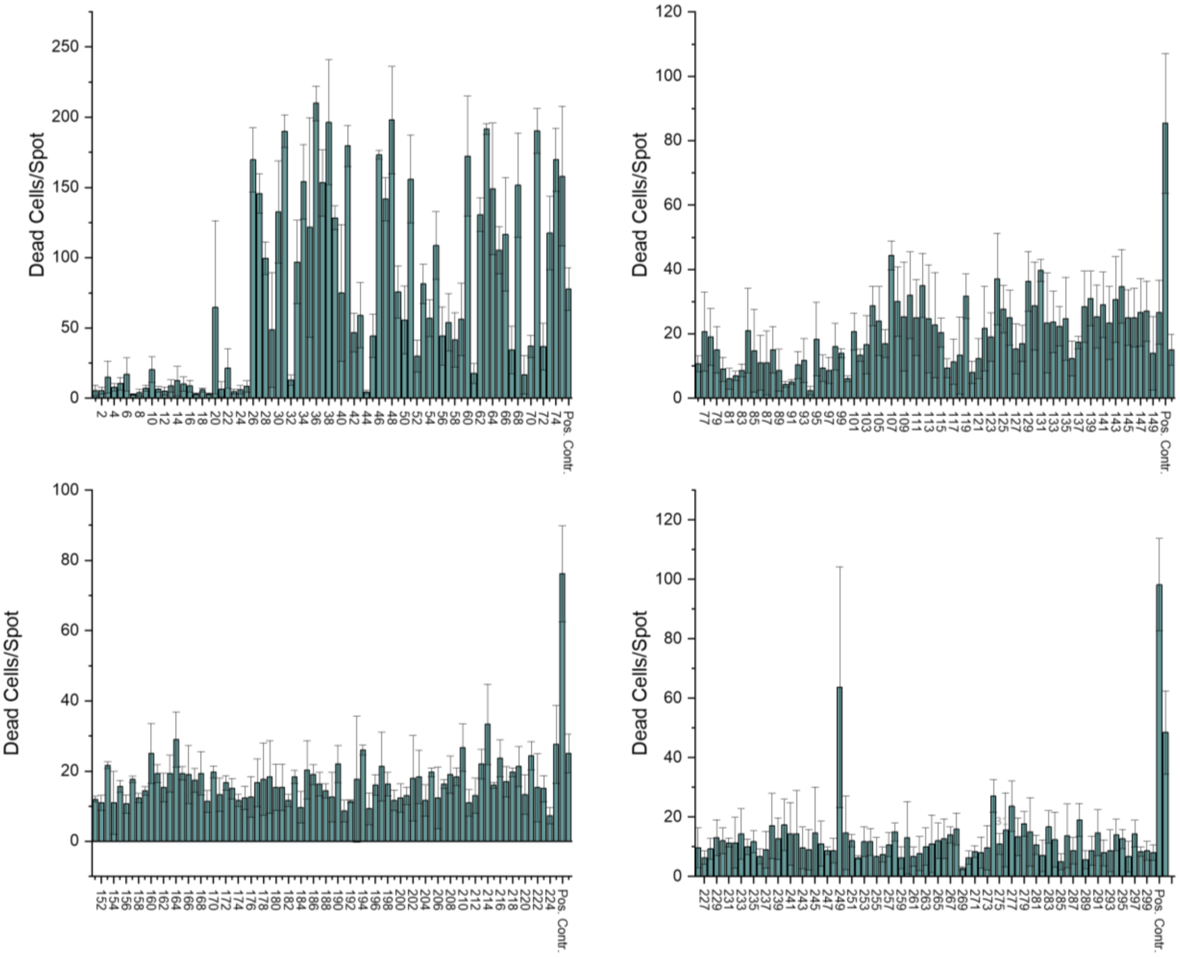

Figure 37: Absolute number of dead cells per spot for the primary screening of 300 different MEK-Inhibitors tested on DMA against HT-29 human colon cancer cells. Values are the average of three replicates, error bars show the standard deviation.

To get a better impression of the potency, the values were normalized. For this, the average number of dead cells per spot in the negative control was subtracted from all values, both the compounds as well as the positive control, to receive the reduced average values. Afterwards, the compounds reduced average values were normalized to the reduced average value of the positive control (Figure 38).

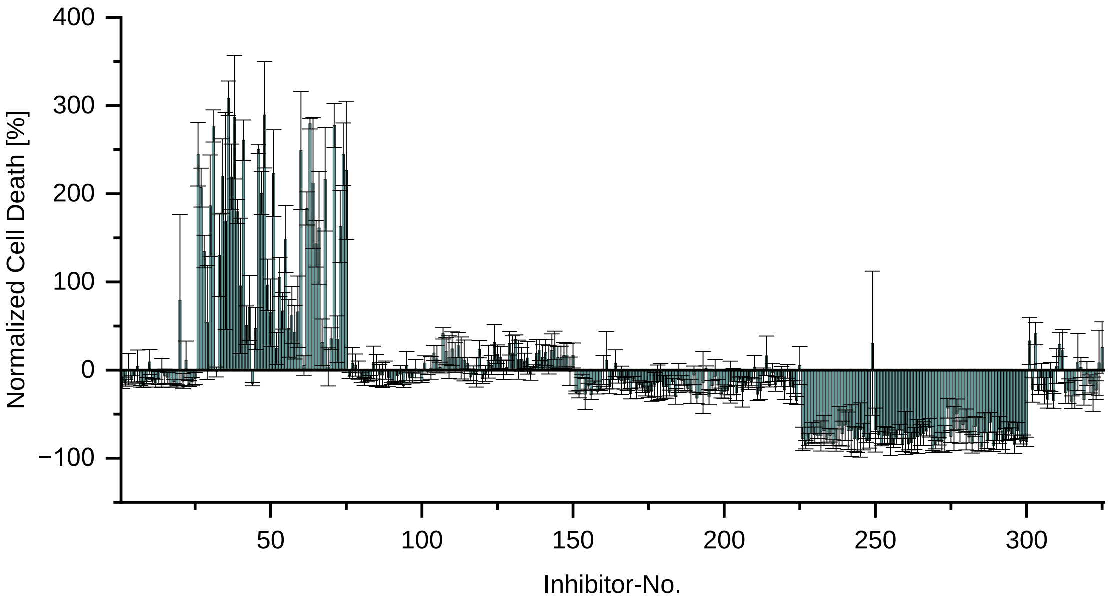

Figure 38: Normalized Cell Death of 325 compounds as ratio of reduced average dead cells per sample spot to reduced average dead cells per positive control spot on DMA. Values are average values of three replicates, error bars show the standard deviation.

The normalized values showed inactivity for compounds containing eight different amino acids, with only minor differences regarding the boronic acid used. However, the compounds containing **A2** and **A3** showed an increased cell death of up to 300 %, indicating a highly increased potency compared to the approved inhibitor MIRDAMETINIB. There was also an observable difference for different boronic acids, potentially indicating that the generally more impactful position in terms of potency was the carbonyl group. This implies that, with a suitable substituent at the carbonyl group, the potency could be fine-tuned through variation of the second substituent at the fluoro-anilin fragment. The first slide containing compounds one to 75 was reproduced and showed the same trend in activity with respect to the amino acids, however, the potency of the individual compounds varied (Figure 39). This could be an indicator for highly comparable IC_{50} values that in turn would lead to fluctuation based on small differences in chemical yield. Due to this, the most promising compounds that showed increased activity compared to the positive control in both experiments need to be individually synthesized and isolated. This allows them to be tested with a precise control over the concentration to record dose-response curves and in turn gives exact IC_{50} values as key parameter for their respective potencies.

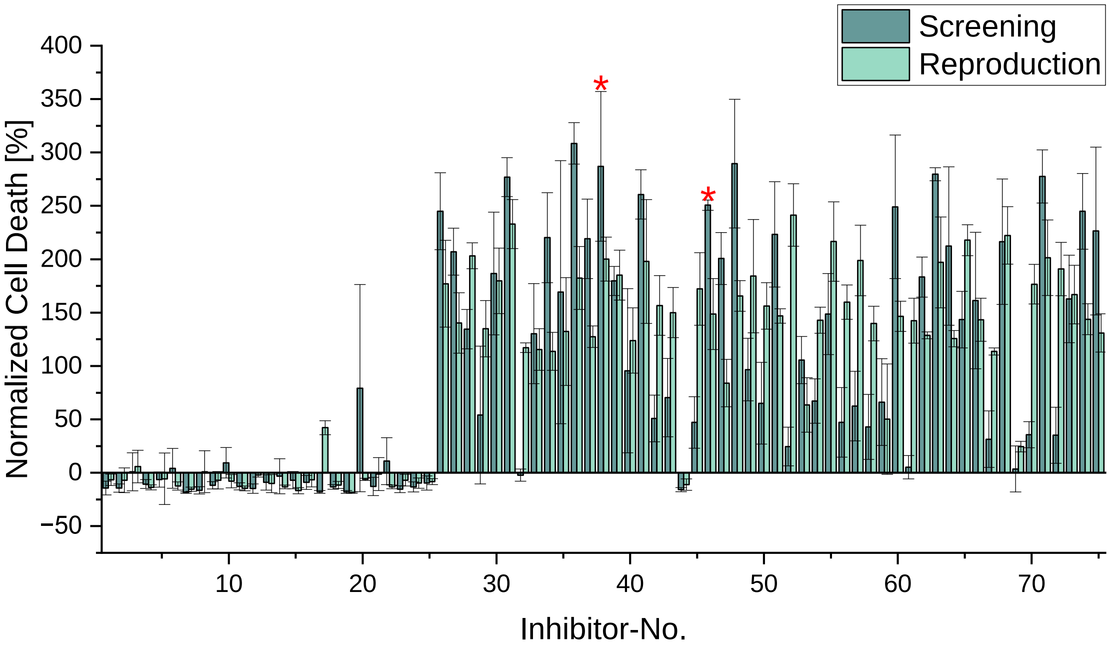

Figure 39: Normalized Cell Death of 75 different compounds as ratio of reduced average dead cells per sample spot to reduced average dead cells per positive control spot on DMA for two independent experiments (screening and reproduction). A clear increase is observed for the groups containing A2 (Compound 26-50) and A3 (Compound 51-75) while no increase is visible for compounds containing A1 (Compound 1-25). The value for the individual compounds, however, shows moderate to high relative deviation between the two experiments. Values are average values of three replicates, error bars show the standard deviation. Red stars indicate the compounds chosen for the first dose-response measurements.

For this, two compounds were prepared on a larger scale through SUZUKI-coupling by JULIUS HÖPFNER, Inhibitor-No. **38** (Compound **7**) and Screening-ID **47** (Compound **8**) and tested together with their precursor (**6**) and MIRDAMETINIB (**5**) for their dose-response curves (Figure 40).

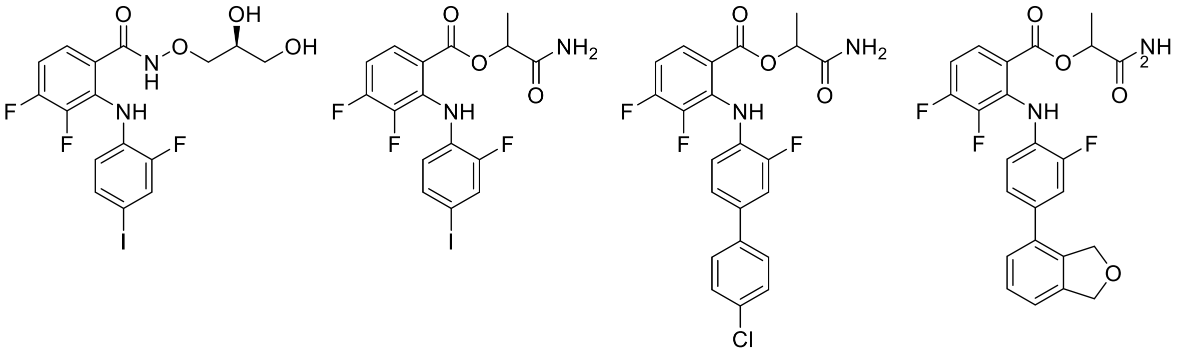

5 **6** **7** **8**

Figure 40: The four selected compounds for the validation measurement.

To do this, HT-29 colon cancer cells were seeded at 5000 cells per well in a 384-well plate and incubated with the respective compound at different concentrations for 72 h.

The results showed moderate activity for both compounds **6** and **7** with IC50 values of >100 µM and a cell viability at 100 µM of around 75-85 %. Compound **8** exhibited a much higher activity with a fitted IC50 of 72±27 µM and a cell viability at 100 µM of 44 %. However, the positive control **5** showed a fitted IC50 of 4.8±0.7 µM and a cell viability of <10 % at 100 µM, indicating a much higher potency than all the selected compounds (Figure 41).

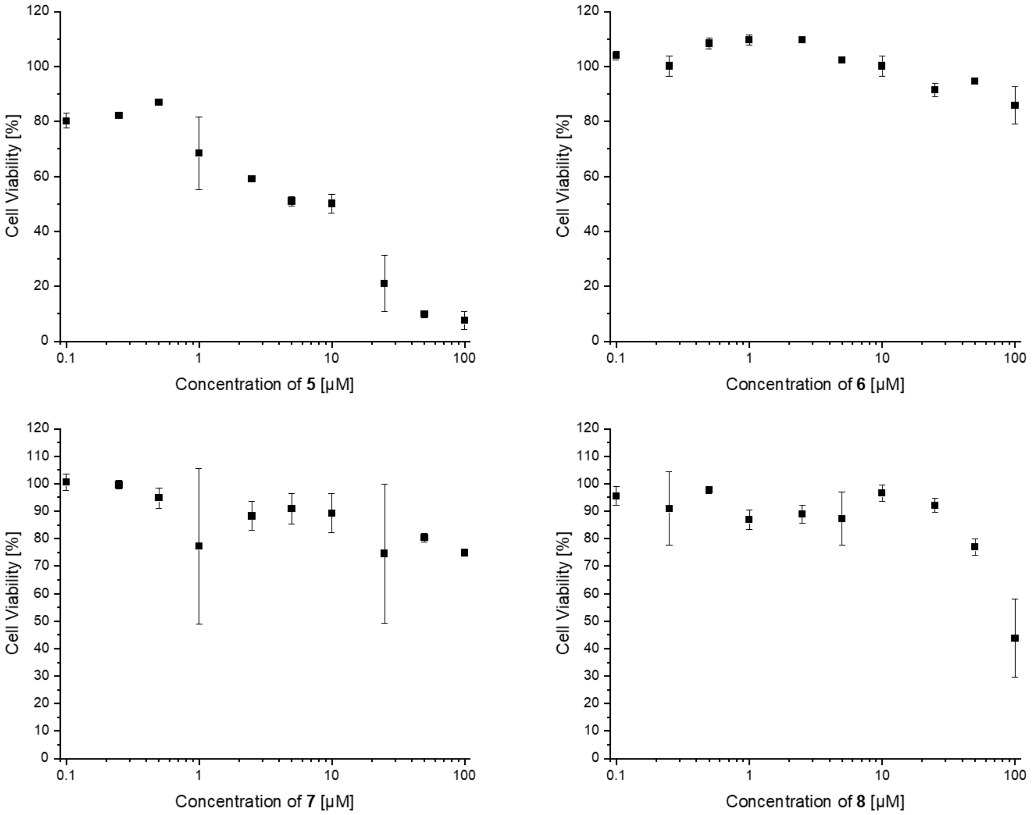

Figure 41: Results of the dose-response measurements of HT-29 human colon cancer cells against 4 different compounds. Experiments were conducted using 384 well plates, cells were seeded at 5000 cells per well and incubated with the different compounds 72 h prior to analysis using a Cell Titer-Glo® luminescence assay. Values are the average of three replicates, error bars show the standard deviation.

Based on the outcome of these measurements it is clearly visible that the substituent on the aniline-fragment has a huge influence on the activity of the compounds. The comparison between compound **6** and **8** shows that aromatic fragments can be more beneficial for the binding process compared to iodine, proving that the modification in this position with aromatic fragments is a viable option to fine tune the potency and can maybe even increase selectivity or make it more effective for treatment of cell lines bearing a mutation on the target protein.

2.2.6 Summary

This chapter described the design and characterization of a chemical workflow that allows preparation of novel compounds exhibiting potentially biologically active core structures. The chemistry was optimized to allow generating the desired products reliably in controlled purity and concentration for a direct subsequent biological evaluation. Out of 325 possible compounds, the formation of the products could be proven through both MALDI-TOF-MS in a standard fashion as well as through MALDI-TOF-MSI to facilitate a HT analysis, with a confirmation rate of 93% and 81%, respectively. Both methods showed comparable results and confirmed the success of the designed chemical reaction sequence for a variety of included building blocks.

Additionally, a cell-based PI-staining assay for a primary screening of the designed molecules against human colon cancer HT-29 cells was optimized and applied for a direct screening of a library of 325 possible compounds with an assay concentration of 10 µM to identify potentially active structural motifs. Two classes of potentially active substituents on one position of the core motif could be identified based on the alanine and beta-alanine amino acids. The substitution on the boronic acid seemed to have an observable effect, with 30 different compounds exceeding the effect of the positive control MIRDAMETINIB, with the most potent compounds exceeding the control by a factor of up to three times. The general activity was confirmed in an independent repetition of the experiment, but the fluctuation on the exact screening values between the independent slides showed an insufficient precision for a systematic optimization of this position under the used conditions. This is most likely due to relatively minor improvements when incorporating the aromatic fragments as compared to the iodine-substituent and fluctuation in the SUZUKI-coupling conversion rate. As an additional validation, selected compounds were prepared individually and tested in a 384 well plate using a luciferase assay to measure dose-response curves. These dose-response measurements performed in well plates clearly confirm that the effect of the second substituent can be significant. The use of aromatic fragments instead of iodine proved successful as was seen with the increased potency of compound **8** compared to compound **6**, with the only difference being in this position. The reduced potency of the target compounds in the control experiment compared to the positive control is still concerning and is very likely linked to racemization during the SUZUKI-coupling step. The bulk preparation of the compounds was done at 80 °C under basic conditions, which could be sufficient to allow racemization of the alanine-residue through the respective enolate. If only one of the enantiomers is biologically active, the effective concentration of the target compound in the dose-response measurements could be down to halve the desired values. This requires additional investigation with chiral HPLC to confirm. On the other hand, more than 30 compounds that showed potency have not been tested yet, roughly half of them including β-alanine, an amino acid that bears no stereo center. Further experiments on those compounds could elucidate whether the discrepancy between well plate and DMA is based on the bulk reaction conditions or some other factor.

Even though the selected compounds were less effective than the commercial control drug in the most recent experiments, systematic derivatization of commonly accepted binding motifs can help to develop new medication with increased potency and will maybe allow to overcome resistance caused by mutations on the target protein through access to additional binding structures.

2.3 High-Throughput Miniaturized Synthesis of PROTAC-like Molecules

2.3.1 Introduction and Motivation

2.3.1.1 Proteolysis Targeting Chimeras

Although generally considered state-of-the-art, small molecule inhibitors also face major challenges when regarding their application in targeted therapy. Due to their mode of action, inhibitors require a binding site that directly affects the protein-function, which not only limits them mostly to enzymes, but often also leads to a low specificity among homologous proteins due to the highly conserved active sites.[125, 126] Another problem is the direct dependence of activity and concentration, requiring comparably high amounts of substance to generate the required protein occupation, thereby risking an increased general toxicity.[126] To overcome these difficulties, alternative mechanisms for the suppression of proteins are researched. A research field that showed explosive growth over the last years is on the topic of proteolysis targeting chimeras (PROTACs) that use cellular mechanisms to degrade proteins rather than inhibiting them, leading to a lasting reduction in protein availability and activity. PROTACs are molecules consisting of three distinct regions: a ligand able to bind the protein of interest (POI) which is supposed to be degraded, a ligand that is able to recruit an E3-ligase and a linker unit connecting these parts. By recruitment of both the E3-ligase and the POI through the PROTAC, a ternary complex is formed that allows both proteins that are involved to get into close proximity. This proximity promotes the ubiquitination of the POI, marking it for the degradation through the proteasome (Figure 42).[127] Since the complex is dynamic, the three components can separate after the ubiquitin transfer, leaving the PROTAC unconsumed and rendering the mode of action thereby catalytic. Additionally, since the POI-binding site does not affect the activity as long as ubiquitin can be transferred, PROTACs do not share the limitations and prerequisites for the binding pocket with inhibitors which were discussed at the beginning of this chapter.

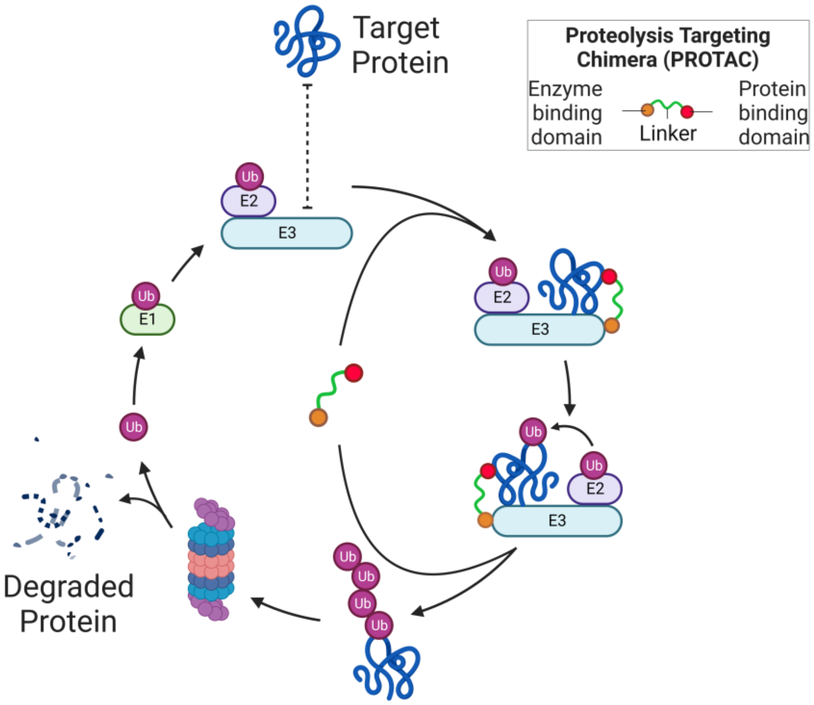

Figure 42: Schematic depiction of the catalytic cycle by which PROTACs induce target protein degradation through ubiquitin transfer and the proteasome. Figure was created with Biorender.com.

As of 2001, the first PROTAC was synthesized and characterized by SAKAMOTO *et al.* containing an Ovalicin moiety to bind methionine aminopeptidase-2 (MetAP-2) as the POI and a phosphopeptide to recruit the heterotetrametric Skp1-Cullin-F-box complex. Here, the induced protein degradation through a PROTAC was shown for the first time.[128] However, the required concentration to observe degradation for the first set of PROTACs was usually in the micromolar range, against the expectations set by the catalytic mode of action.[129] One of the reasons for the poor-performance of those PROTACs at first was the poor cell permeability of the comparably large molecules. After this, general interest in the development of small molecule PROTACs without the need of large peptides and with the ability to recruit different E3-ligases arose. The first real small-molecule PROTAC was then published in 2008 by *Crews* and coworkers who developed a peptide-free degrader that could induce the cellular degradation of non-steroidal androgen receptor ligand (SARM) by recruitment of the MDM2 E3-ligase.[130] From there on, the development of PROTACs proceeded rapidly with a variety of possible POIs and POI-ligands. For the E3-ligases, two major recruitment-domains have been established, the cereblon (CRBN) subunit or the von-Hippel-Lindau (VHL) subunit.[131, 132] The choice of the right E3-ligase can make drastical differences in the overall performance of PROTACs, because the ubiquitin-transfer from ligase to POI is in many cases more favored for specific pairs of proteins.[133] Additionally, the choice of the right ligands for both proteins is of major importance since a low affinity can lead to a decreased activity and specificity but too high affinity can prevent the ternary complex from dissociating as observed in covalent PROTACs, thereby blocking the PROTAC from further reactions or even leading to the degradation of the PROTAC together with the POI.[134] While the protein ligands used are definitely the most obvious parameters to affect a PROTACs efficiency, the structure of the linker in between can be crucial, too, and reaches from simple effects on the solubility or cell permeability to more complex effects such as conformational stabilization or secondary binding.[135-137]

2.3.1.2 Motivation and Aim

The aim of this work was to develop and characterize a workflow to synthesize a library of PROTACs on the DMA in a way that would consume only minimal amounts of material and allow a direct evaluation of the synthesized molecules in a cellular assay to assess their degradation potency. The ligand-parts for both the POI and the E3 ligase were chosen as fixed to prioritize the synthesis of PROTACs bearing the same binding motifs with different linker-lengths and -branching to further investigate the effects of the linker on the degradation behavior and elucidate the structure-activity relation (SAR).

Therefore, a similar solid-phase synthesis approach as described in Chapter 2.2 was chosen, utilizing the Ugi 4-component reaction instead to cover a large chemical space with a limited number of starting materials. The recruited E3 ligase was chosen to be CRBN with the respective binding motif being the thalidomide subunit. The E3 recruiting part of the molecule was to be introduced into the reaction in form of aliphatic aldehydes bearing a terminal functionalization with the ligand. As POI, MEK1 and 2 were chosen again and the binding motif used here was similar to the core structure in Chapter 2.2. The POI binding part was introduced to the reaction as carboxylic acid for which 3,4-difluoro-2-(2-fluoro-4-iodophenylamino)benzoic acid (**4**) was used again. The amines in the reaction were surface amino groups on the DMA that were directly attached to a *o*-nitrobenzyl moiety and served both as anchor-point as well as cleavage site. The fourth component were the isocyanides for which commercially available isocyanides were chosen in order to facilitate a broad variety of structural motifs in the branching. The whole reaction scheme is shown below (Figure 43)

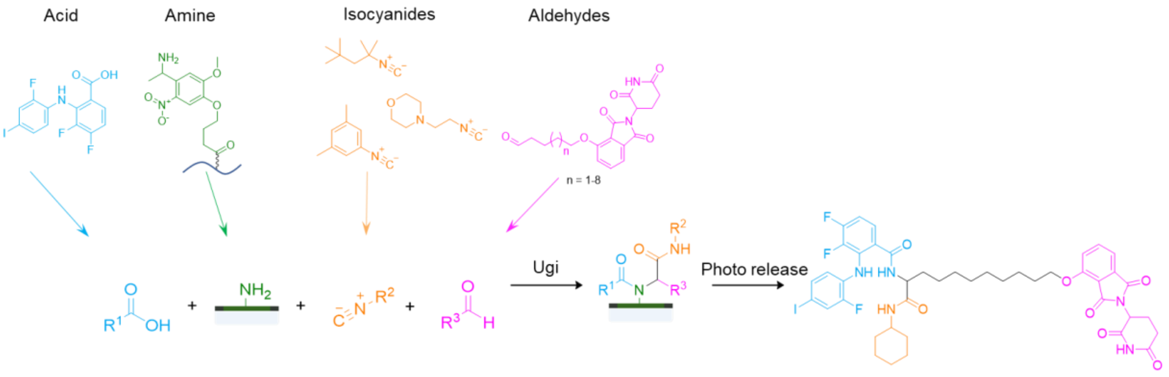

Figure 43: Reaction Scheme for the preparation and release of PROTAC-like molecules on the DMA *via Ugi*4CR. Example structures for all reagents as well as a possible product are given. The figure was adapted from TIAN *et al.*[2]

2.3.2 Chemical Characterization

As it was shown previously that the UGI reaction works on the DMA and is compatible with solid-phase synthesis, the foundation for this project was clear. In order to include the desired binding motifs, substituted aldehydes containing a thalidomide subunit had to be synthesized, which was performed by Dr. YE TIAN (IBCS-FMS) through oxidation and subsequent nucleophilic substitution of halogenated alcohols (Figure 44).[138]

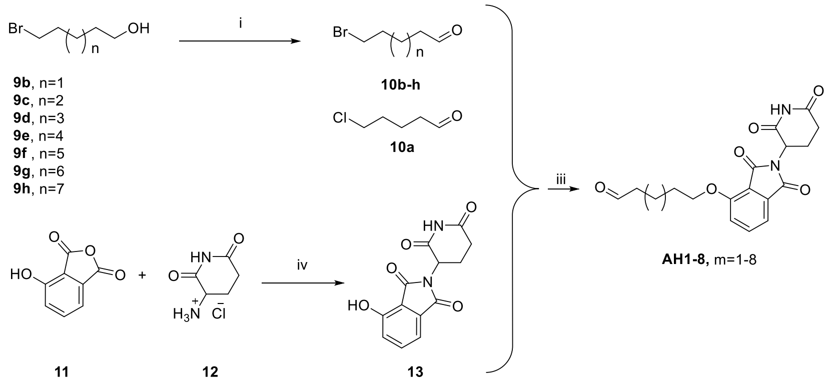

Figure 44: Synthetic route for the preparation of aldehydes containing a thalidomide warhead and various aliphatic linkers for the UGI reaction: (i) PCC, DCM, N_2, 3h at rt; (ii). AcONa, AcOH, 12 h at 110°C; (iii). KI, KHCO3, DMF, 12 h at 60°C. The figure was adapted from TIAN *et al.*[2]

To optimize the conditions for the reaction without use of these tailored molecules, a model reaction was conducted using commercially available small molecules with comparable properties.

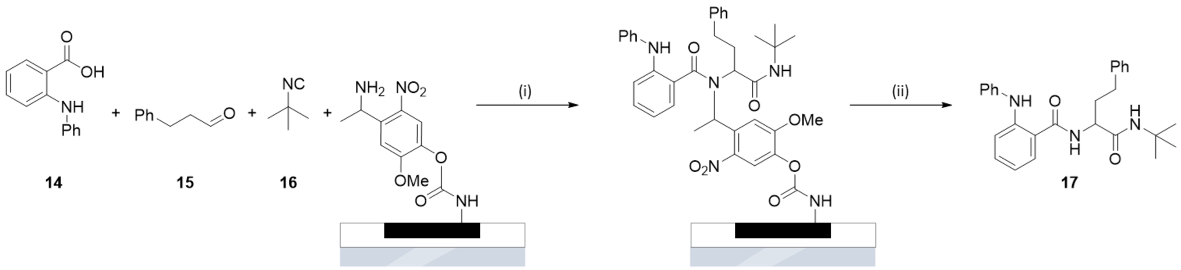

Figure 45: Model reaction for the characterization of product loading and release kinetics of the solid-phase UGI-reaction on DMA: (i) Acid 14, Aldehyde 15, Isocyanide 16 on DMA in ethylene glycol/γ-butyrolactone (1:9, v/v), 18 h at rt; (ii) UV-irradiation.

As the goal was again to achieve a final product concentration of 10 µM per spot with an assay volume of 1 µL, the desired product release per spot was 10 pmol or 6.5 pmol/mm^2. To identify conditions that were suitable for this, an optimization procedure similar to chapter 2.2.2 was performed. A DMA with 80 round spots (diameter 2.8 mm) was modified with photolinker solution (10 mM) and used for a UGI-*4CR*. The surface amines were preincubated with a solution of 3-phenylpropionaldehyde (**15**) for 2h to preform an imine. Afterwards, solutions of *N*-phenylanthranilic acid (**14**) and *tert*-butyl isocyanide (**16**) were added, and the reaction was carried out for 18 h (Figure 45). The three different reaction components were all added in an equimolar amount with three different final reactant concentrations (10, 20 and 50 mM). The different surfaces were irradiated for different times (5-40 min) and the release of product **17** was measured *via* LC-MS in dependency of the reactant concentration and the irradiation time. For the calculation, the integration values were compared to standard compound **18**, supplied by Dr. YE TIAN. From this, three photorelease curves were obtained that showed the product release per area, which was translated into the corresponding assay concentration with an assay volume of 1 µL per spot (Figure 46). With a reactant concentration of 10 mM and an irradiation time of 5 min, a product release of 7.44 ±3.1 pmol/mm^2 was obtained, which would lead to an ideal assay concentration of 11.4±4.71 µM.

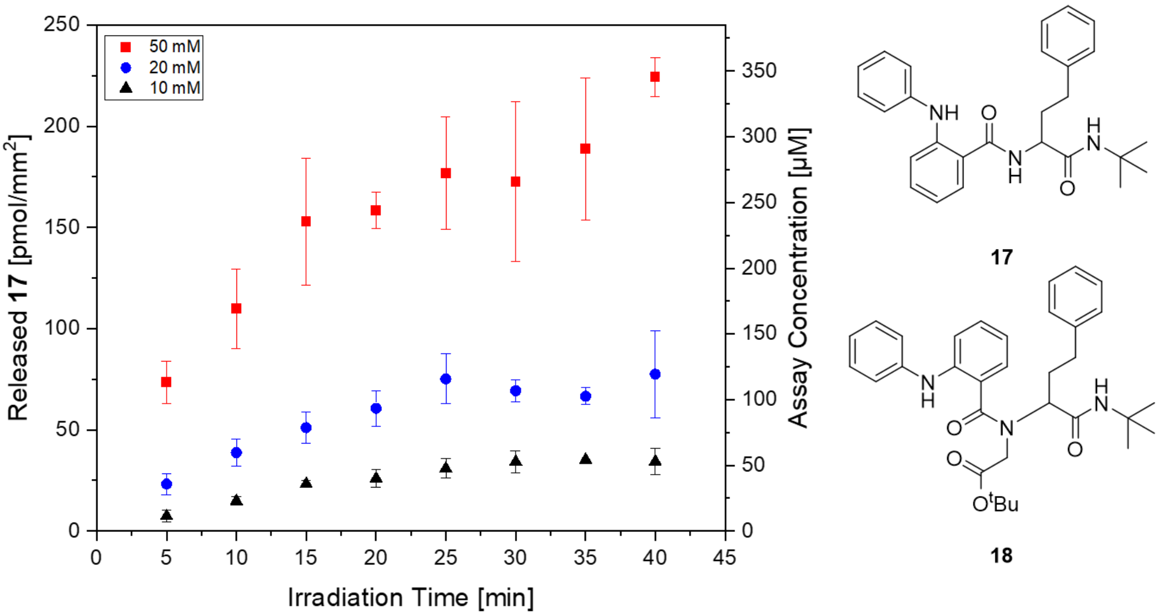

Figure 46: Released amount of compound **17** after solid-phase UGI-reaction on DMA with three different final reagent concentrations (10, 20, 50 mM). Values are calculated based on a calibration done with compound **18** as standard. Error bars show the standard deviation of three independent repetitions. The figure was adapted from TIAN *et al.*[2]

In order to confirm that the reaction proceeds and forms the desired products within the scope of reactants applied for the synthesis of PROTAC-like molecules, MALDI-TOF-MS analysis was carried out again. A library of 160 compounds was prepared, using 8 aldehydes with different length of the aliphatic linker and 20 different isocyanides. The library was prepared on two DMA slides bearing 320 round spots (diameter 1.4 mm) modified with 100 mM photolinker. The reaction was carried out with 300 nL reaction volume per spot with a final concentration of each reagent at 10 mM. After the reaction was conducted, the substrate was cleaned and the target compounds were released off the solid phase with 40 min UV-irradiation. The target compounds were extracted from the spots using 1 µL of a DMF/Water mixture (3:1) and transferred to a ground steel target plate. The target was spraycoated with 2,5-dihydroxybenzoic acid (DHB) and then mass spectra of each spot were recorded by Dr. *STEFAN SCHMIDT* (CeMOS) using a rapifleX MALDI-TOF system (Bruker, Bremen, Germany) in positive ion mode. The spectra were analyzed for the presence of the most prominent adducts of the target compounds ($[M+H]^+$, $[M+Na]^+$, $[M+K]^+$), out of 160 compounds 132 could be identified, leading to a synthetic success rate of 83 % (Table 4).

Table 4: Identification rate of different PROTAC-like molecules as product of solid-phase synthesis on DMA, regarding each component of Ugi reaction. The figure was adapted from Tian *et al.*[2]

No.	Structure	Identified Products (%)	No.	Structure	Identified Products (%)	No.	Structure	Identified Products (%)
AC1	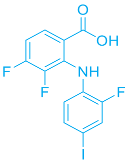	83	**IC2**	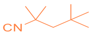	87.5	**IC12**	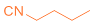	75
AH1	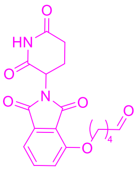	90	**IC3**	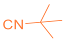	75	**IC13**	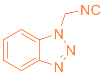	75
AH2	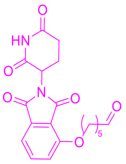	75	**IC4**	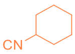	100	**IC14**	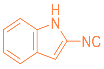	88
AH3	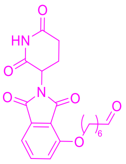	85	**IC5**	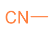	25	**IC15**	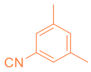	88
AH4	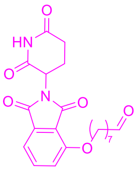	85	**IC6**	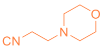	100	**IC16**	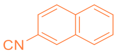	100
AH5	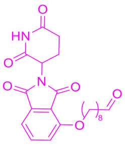	90	**IC7**	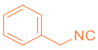	100	**IC17**	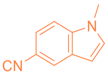	88
AH6	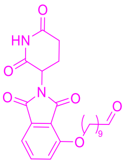	90	**IC8**	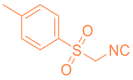	87.5	**IC18**	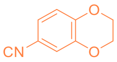	100
AH7	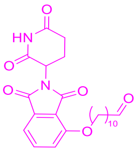	95	**IC9**	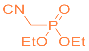	100	**IC19**	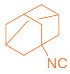	100
AH8	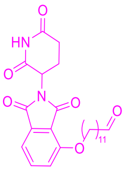	50	**IC10**	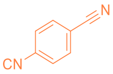	25	**IC20**	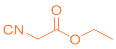	88
IC1	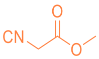	100	**IC11**	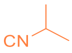	50	**Total**		83

The product confirmation rate was comparable for the different aldehydes (±14 %) and the isocyanides (±23 %). Only **AH8**, **IC5**, **IC10** and **IC11** showed significantly lower success rates. While for **IC5** and **IC11** the volatility might be the biggest issue, leading to a lower concentration than intended, the results of **AH8** and **IC10**, most likely indicate a decreased reactivity compared to the other components. The limitations of volatile components in miniaturized open systems are known, thus, leaving only one aldehyde (1 of 8, 13 %) and one isocyanide (1 in 20, 5 %) that are not suitable for the reaction conditions, which shows a high tolerance of the synthetic workflow for different structural motifs.

Table 5: Purity of selected PROTAC-like molecules 1-25, prepared on 2.8 mm spots of a DMA modified with 20 mM photolinker solution. The figure was adapted from TIAN *et al.*[2]

Compound	Aldehyde	Isocyanide	Purity (%)
PROTAC1	AH1	IC4	76
PROTAC2	AH1	IC6	78
PROTAC3	AH1	IC7	60
PROTAC4	AH1	IC10	73
PROTAC5	AH1	IC14	69
PROTAC6	AH1	IC16	73
PROTAC7	AH1	IC20	43
PROTAC8	AH2	IC4	71
PROTAC9	AH2	IC6	99
PROTAC10	AH2	IC7	57
PROTAC11	AH2	IC14	70
PROTAC12	AH2	IC16	63
PROTAC13	AH2	IC20	40
PROTAC14	AH3	IC4	78
PROTAC15	AH3	IC6	64
PROTAC16	AH3	IC7	62
PROTAC17	AH3	IC14	71
PROTAC18	AH3	IC16	57
PROTAC19	AH3	IC20	61
PROTAC20	AH4	IC4	80
PROTAC21	AH4	IC6	74
PROTAC22	AH4	IC7	65
PROTAC23	AH4	IC14	71
PROTAC24	AH4	IC16	66
PROTAC25	AH4	IC20	50

Out of these 132 compounds, 25 were selected and prepared on a larger scale on a DMA with 80 spots (diameter 2.8 mm). They were prepared on a surface modified with 10 mM photolinker solution with a final reactant concentration of 20 mM. After the reaction, the slides were washed and irradiated with UV-light to release the target compounds, these were then extracted out of the spots and analyzed *via* LC-MS to assess the purity (Table 5).

The average purity was determined to be 67 % with only two compounds possessing a purity below 50 %. This purity was regarded as sufficient for a primary screening; thus, the compounds were put to use for further biological screenings.

2.3.3 Biological Screening

Applying a similar screening procedure to the one described in chapter 2.2.5, a small library of randomly selected PROTAC-like molecules containing a MEK-targeting warhead was tested again HT-29 human colon cancer cells (Table 6). For this, the library was prepared in three independent experiments on DMAs with 320 spots (diameter 1.4 mm). The spots were modified with photolinker solution (10 mM) and the reaction was then carried out with a total volume of 300 nL per spot and a final reactant concentration of 10 mM. For the preparation, a randomized layout was chosen, each slide contained the same 22 different compounds with 10 replicates and 20 spots without compounds for controls. After 18 h, the slides were washed and sterilized with an ethanol/water mixture (70:30) for 30 min. The slides were dried and 700 nL of DMEM (supplemented with Penicillin/Streptomycin, 0.1 % (v/v) and DMSO, 0.14 % (v/v)) were added to the compound containing spots and 10 of the empty spots. To the remaining 10 empty spots, 350 nL of DMEM (supplemented with Penicillin/Streptomycin, 0.1 % (v/v) and DMSO, 0.14 % (v/v)) were added. The slides were sealed in a petri dish containing 2 mL phosphate buffered saline (PBS) and then irradiated with UV-light for 5 min. To the spots containing only 350 nL medium, 350 nL of a solution of MIRDAMETINIB (28.6 µM) in DMEM (supplemented with Penicillin/Streptomycin, 0.1 % (v/v) and DMSO, 0.14 % (v/v)) were added. The slides were preincubated at 37 °C for 18 h to dissolve the compounds out of the polymer layer and then 300 nL HT-29 cell suspension ($1 \cdot 10^6$ cells/mL) in DMEM (supplemented with Penicillin/Streptomycin, 0.1 % (v/v) and FBS, 30 % (v/v)) were added to each spot. The slides were incubated for 72 h and then stained with PI and imaged with fluorescence microscopy.

Table 6: Building blocks used in the preparation of 22 different PROTAC-like molecules for a primary screening against HT-29 human colon cancer cells.

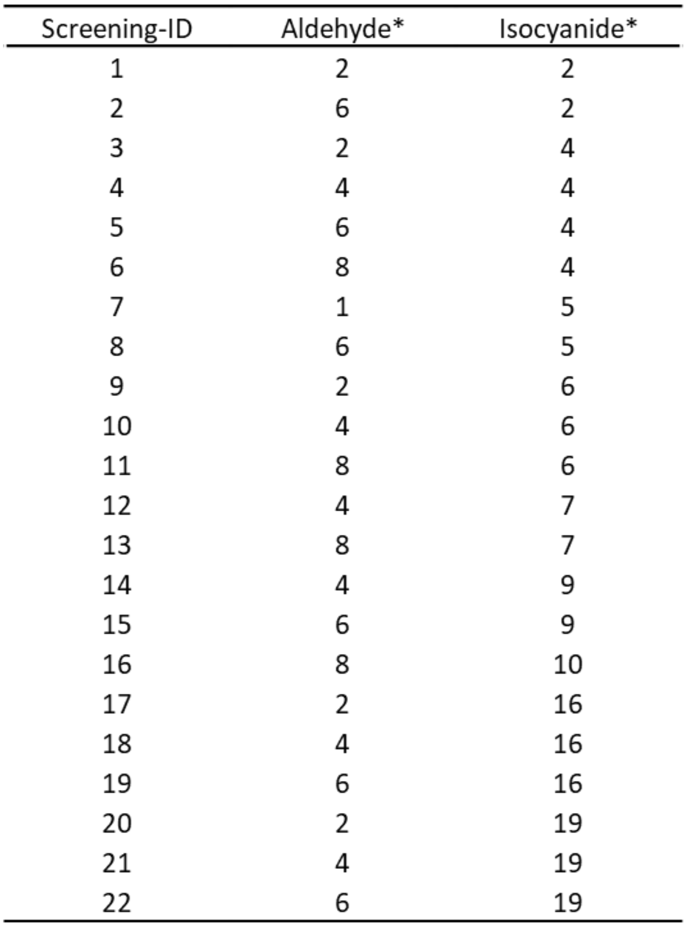

Screening-ID	Aldehyde*	Isocyanide*
1	2	2
2	6	2
3	2	4
4	4	4
5	6	4
6	8	4
7	1	5
8	6	5
9	2	6
10	4	6
11	8	6
12	4	7
13	8	7
14	4	9
15	6	9
16	8	10
17	2	16
18	4	16
19	6	16
20	2	19
21	4	19
22	6	19

*Aldehyde and isocyanide used for the synthesis of the target PROTAC-like molecule

While no significant activity could be observed, the results showed a very good reproducibility throughout all three repetitions in both the samples as well as the controls (Figure 47). These results indicate a reliable readout when combining chemistry and biology, however, the lack of activity is something that could be attributed to a concentration- or a potency issue. To investigate this, further experiments with a larger set of compounds would be required. On top of that, variation in the target compound concentration would be beneficial to further pinpoint the lack of activity in the tested system to either of the two aforementioned factors.

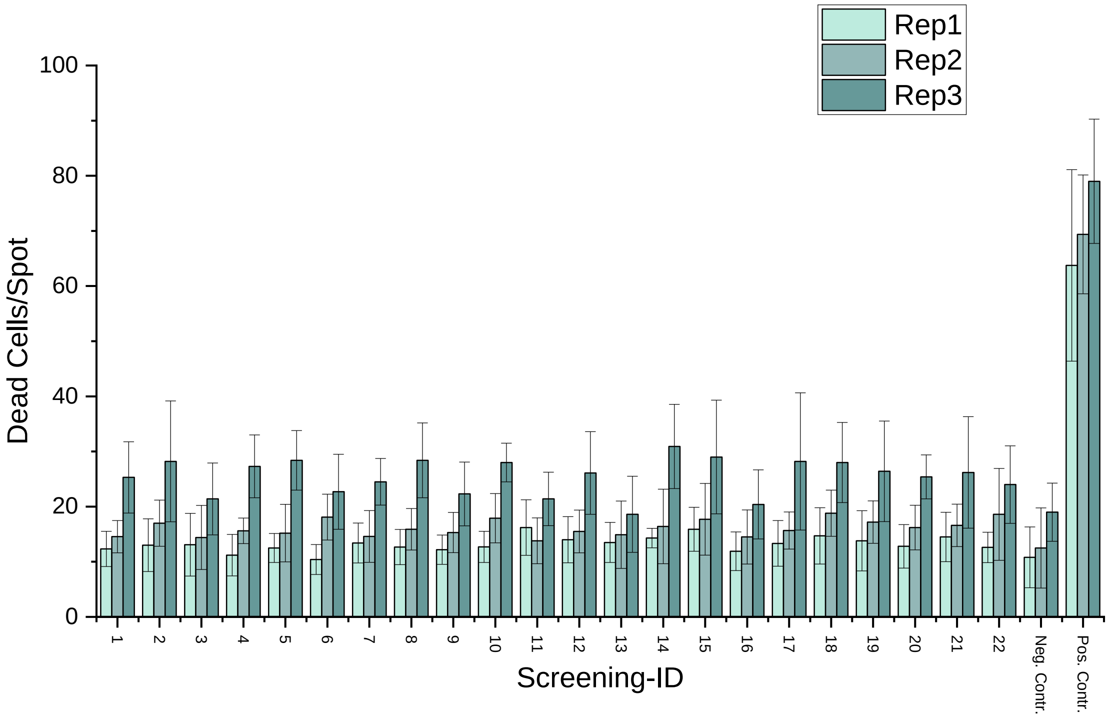

Figure 47: Results of a primary screening of randomly selected 22 PROTAC-like molecules against HT-29 colon cancer cells. Each graph represents an independent experiment with the average number of PI-positive cells versus the compound identifier. Error bars show the standard deviation of 10 replicates. The figure was adapted from TIAN *et al.*[2]

2.3.4 Summary

This chapter showed the preparation and characterization of a synthetic workflow to use multicomponent reactions to generate multifunctional molecules in a single reaction step through solid-phase synthesis on DMA and applied this approach to synthesize a library of PROTAC-like molecules. The synthetic parameters were optimized using a model reaction to gain precise control over the overall product loading with respect to the reagent concentrations and the irradiation time for the photorelease through LC-MS analysis. A set of 160 compounds was then prepared and analyzed via MALDI-TOF-MS to yield a confirmation rate for the synthetic success of 83 %. To further assure no contamination with side products and a sufficient purity for subsequent biological experiments, 25 of these PROTAC-like molecules were prepared on a larger scale for analysis via LC-MS and showed an average purity of > 67% with no major side product presence.

The biological evaluation of 22 different PROTAC-like molecules in a primary cell-based screening against human colon cancer HT-29 cells was performed on DMA using PI-staining and fluorescence microscopy as readout. These experiments showed very good reproducibility indicating stability in both the assay and the chemical synthesis. However, none of the 22 tested compounds showed a significant increase compared to the negative control. This hint at a problem with the chosen concentration range, as the relation between activity and concentration of PROTACs is more complicated than it is for inhibitors such as the used positive control due to the competition between binary and ternary complex formation of the POIs and the PROTAC-molecule (Hook-Effect). Due to this, ideal concentrations for a screening of PROTAC-like molecules are hard to determine and need step wise approximation. This issue can be overcome by variation in target molecule concentration which was shown to be possible using the DMA and a solid-phase synthesis approach. Covering a concentration range in the assay rather than testing a single concentration can already be enough to differentiate between biological inactivity and concentration-dependent inactivity. Therefore, this does not limit the application of the developed experimental workflow for the design and evaluation of novel PROTACs, but shows additional parameters important in the experimental design.

Should the cell-based assay not be viable for the analysis of degradation potency due to a lack of sensitivity or something comparable, different approaches such as antibody staining or cell lysate-based experimentation could be considered to further simplify the experimental workflow and make it more robust.

3 Conclusion

The core of this work focuses on the overall application of high-throughput experimentation on the interfaces of chemistry, biology and material science. While miniaturization and parallelization are getting more and more commonly applied in different disciplines, the transition of one field of science into another one is still challenging as the requirements to miniaturized platforms vary drastically depending on the conducted research. Nevertheless, transitioning from one scientific discipline to another one on the same platform offers unique advantages such as resource and time conservation and is therefore of utter importance. The droplet microarray used here proves suitable for this due to the high tolerance of different experimentation conditions such as solvents, irradiation and temperature, while offering the potential of scaling down experiments into the submicroliter range. Typical chemical reactions were carried out at 300 nL and biological screenings at 1000 nL per sample, reducing the required volume of samples and reagents by more than two orders of magnitude compared to 384 microtiter plates. This is also reflected by the experimental density of the used arrays here, which ranged from 4.2 experiments/cm^2 to 61.4 experiments/cm^2 in comparison to 3.5 experiments/cm^2 for a 384 well plate. While the miniaturization itself offers various challenges such as differences in reaction kinetics, side reactions or evaporation, the DMA is proven to be a viable option for miniaturized HT-experimentation.

The first part of the work focused on the application of miniaturization for the acceleration of material design, through the creation of soft material libraries with a sample volume of 130 nL. Binary combinations of radically polymerizable monomers and crosslinkers were prepared and photopolymerized to yield ~ 1000 different materials for the evaluation of their photostability. The analysis was carried out in HT fashion using fluorescence microscopy and semi-automatic image analysis. The data sets generated from this contained more than 66.000 data points and was successfully applied to train a ML model by Dr. PATRICK REISSER showcasing the advantage of parallelized experimentation in terms of time saving. The translation of the properties obtained from nanoliter-scale experimentation back to bulk material was shown to be successful to validate that the experimental workflow designed here can accelerate materials design while drastically reducing the amount of materials consumed compared to microliter scale by three orders of magnitude. The entire workflow is not restricted to radically polymerizable materials and other key parameters such as swelling ratio can be obtained with the same setup or only minor changes in the workflow. By combining the reliable preparation of materials on a nanoliter scale shown here with biological analysis and physical characterization, the DMA can be used as a platform to develop materials with complex properties, as required, for example, in tissue engineering with a drastically reduced material and time consumption compared to the microliter scale.

The second part of the work revolves around the solid-phase synthesis of small molecule MEK inhibitors through a combination of two different chemical reactions, the SUZUKI-coupling and amidation. While both reactions were already characterized on the miniaturized format, the combination of them gave access to close derivatives of FDA-approved MEK-inhibitors with structural changes on the two most important parts of the binding motif. The characterization of each reaction step in terms of purity and conversion gave full control over the amount of product formed on the surface as well as how much is released to optimize the conditions for a subsequent cell screening to evaluate the potency of those derivatives. The formation of the 325 possible different reaction products could be confirmed through MALDI-MS imaging as a HT analysis technique without the need to transfer the samples from the hydrophilic spot. By this, analysis could be conducted using roughly 3 ng of substance for each compound. Measurements from ground steel target plates confirmed the results of the MS imaging and allowed MS/MS measurements for additional confirmation of the target molecules structures. The overall confirmation rate for the ground steel and ITO-measurements were 93 % and 81 %, respectively. In a different experiment, a cell death-based assay based on PI-staining and fluorescence microscopy was then applied directly on the spots used to carry out the chemical reaction in a direct to biology approach and allowed to identify beneficial substituents on one position of the binding motif that were actively leading to cell death of HT-29 human colon cancer cells. To further investigate this, two compounds of the potential hits were synthesized individually and chemically characterized through NMR spectroscopy, LC-MS and MS. These pure compounds were then analyzed together with their respective precursor and a positive control for their dose-response curves in a viability assay in 384 well plates. The compounds didn’t show higher activity as suggested by the primary screening but did in fact possess activity against the cell line. One of the compounds showed significantly higher activity compared to the precursor, suggesting that substitution of the commonly applied iodine group with an aromatic fragment can increase the binding of the hydrophobic pocket in MEK leading to increased potency. The insight gained from this can be potentially used to create more potent inhibitors or ones more effective in the treatment of cell lines resistant to MEK inhibition due to mutations on MEK itself. While the IC_{50} value of this compound was only at 72 µM compared to the 4.7 µM of the FDA approved inhibitor, there are still several compounds remaining that showed increased activity in the primary screening. Additional studies to assure that the decreased activity is not due to racemization occurring during the bulk preparation are also required.

The final part followed a similar idea to create bioactive molecules through solid-phase synthesis but applied multicomponent reactions for the creation of PROTAC-like molecules. The formation and the amount of target compound was analyzed in a similar manner to the previous work on inhibitors using a model reaction and analysis via LC-MS. After the product loading was optimized, the possible compounds were analyzed using ground steel target MALDI-TOF-MS which identified 83 % of the possible 120 compounds. Additionally, 25 of these compounds were analyzed *via* LC-MS to assure a sufficient purity, which laid at 67 %. Out of these 120 compounds, 22 were randomly selected and subjected to the same biological screening conditions as described in chapter 2.2. The test showed very good reproducibility, showcasing the robustness of the designed workflow. However, no active compounds could be identified in this small screening, a screening of the entire library could prove to me more fruitful. Even though the dose-response relation of PROTACs is more complicated than the one of inhibitors due to binary and ternary complex formation, making it harder to set an ideal concentration for such a screening, the insight gained from potential hits can help accelerate the understanding of the structure-function relation and therefor increase the developmental pace of novel degraders. Wider screening parameters with varying target concentrations might already be sufficient to help identify bioactive molecules.

Altogether, this work showed the development of robust screening pipelines for the application on the interface of different research disciplines to conduct experiments with a faster pace while reducing the material and time consumption. Approaches such as "Direct-to-Biology" that combine all aspects of an experimental workflow without clear restriction to just a part of it are becoming more and more prominent since the advantages outweigh the challenges in the experimental design, making this a viable option for the future of many research fields such as drug development or personalized medicine. While it is not necessarily the best for all parts of science, developing and applying those platforms will help identify the strengths and weaknesses in each individual case to make future research as efficient as possible.

4 Materials and Methods

Monomer Purification

Monomers were purified from inhibitors prior to use by passing over a column of basic aluminum oxide (Alfa Aesar, Ward Hill, MA, USA).

Preparation of Nanoparticle DMA

The preparation of Droplet Microarrays was done according to a patented procedure.[139] For the preparation uncoated Nexterion glass slides (Schott AG, Mainz, Germany) were used. The glass was activated prior to use by 10 min ozone treatment in an UVO-Cleaner (Jetlight Co. Inc., Irvine, CA). Afterward the slides were coated with a solution of AEROSIL 200 (Evonik Industries AG, Essen, Germany), trimethoxyvinylsilane (VWR International, Radnor, PA), and hydrochloric acid (VWR International, Radnor, PA) in ethanol (VWR International, Radnor, PA). Slides were cured at 150 °C for an hour and then washed with ethanol. For the creation of hydrophobic or hydrophilic regions slides were covered with a solution or 1H,1H,2H,2H-perfluorodecanethiol in isopropanol or mercaptoethanol in ethanol/water (1:1) respectively, and irradiated for 90 s using a UVA Cube 2000 (Dr. Hönle AG, Gilching, Germany).[1]

Preparation of HEMA-*co*-EDMA DMA

An uncoated Nexterion glass slide (Schott AG, Mainz, Germany) was activated by a UVO cleaner (Jetlight Co. Inc., Irvine, CA) for 10 min. Then 150 uL of modification mixture (20% 3-(trimethoxysilyl)propyl methacrylate in ethanol) was applied on the slide and covered with another activated glass slide. The solution was evenly distributed between these two slides and all the bubbles were removed. The slides were left to react for 30 min. These functionalization steps were repeated two times, followed by washing with acetone and drying with nitrogen gun.

Nanoporous poly(2-hydroxyethyl methacrylate-*co*-ethylene dimethacrylate (HEMA-co-EDMA) polymerization mixture was prepared with following components: 24 wt%

2-hydroxyethyl methacrylate (HEMA), 16 wt% ethylene dimethacrylate (EDMA), 12 wt% 1-decanol, 48 wt% cyclohexanol, and 0.4 wt% 2,2-dimethoxy-2-phenylacetophenone (DMPAP). 15-30 µL of polymerization mixture were pipetted on a fluorinated glass slide, and then a modified glass slide was placed on top allowing the mixture to spread without formation of air bubbles. The sandwich-like slides were put under the UV lamp (260 nm wavelength) and irradiated for 20 min with 10 mW/cm^2 intensity. After that, the slides were separated and washed with ethanol, followed by immersing the substrate in ethanol for several hours.

The esterification solution was prepared in a 50 mL falcon tube by mixing 45 ml of acetone, 56.0 mg of 4-(dimethylamino)pyridine and 111.6 mg of 4-pentynoic acid. The slides with poly(HEMA-*co*-EDMA) surfaces were immersed in the solution and cooled at -20°C for 15 min. Then, 180 µl of N,N'-diisopropylcarbodiimide was added to the solution, and the tube was fixed on a shaker for overnight at 200 rpm. After esterification, the slide was immersed in ethanol for 2 h to remove unreacted chemicals.

In a dark room, 200 µL of the perfluorodecanethiol solution (10% 1*H*,1*H*,2*H*,2*H*-perfluorodecanethiol in 2-propanol) was pipetted on the alkyne substrate and covered with a photomask (round spots with diameter of 900 µm, 18x 64 spots per slide, round spots with diameter of 1.4 mm, 10 x 32 spots per slide; or round spots with diameter of 2.8 mm, 5 x 16 spots per slide). After irradiation with UV light at 10 mW/cm^2 for 3 min, the substrate was washed and dried. Then 200 µL of the hydrophilic thiol solution (15 wt% cysteamine HCl in a 1:1 water:ethanol solution) was pipetted on the substrate and covered with a fluorinated quartz slide. Next, it was again irradiated with 260 nm UV light at for 3 min, washed with water/ethanol and dried with an air gun.

The morphology of the poly(HEMA-co-EDMA) film on a silanized glass substrate was characterized by a scanning electron microscope (Zeiss LEO 1530) at an operating voltage of 2 kV. Prior to the SEM measurements, the samples were coated with a 10 nm thick platinum layer.

Preparation of HEMA-*co*-EDMA DMA on ITO-coated Glas

ITO-coated glass slides (Diamonds Coatings, West Midlands, UK) were activated first, by submerging in a solution of hydrogen peroxide in water (30%, v/v) for 45 min. The slides were afterwards washed with water and acetone, dried with nitrogen flow and then submerged in a solution of 3-(Trimethoxysilyl)propylmethacrylate (3%, v/v) in toluene. The mixture was heated to 80 °C overnight, the slides were removed from the solution and washed with acetone. After drying, the slides were used like normal glass slides for the preparation of polymer films.

Liquid Dispensing

For dispensing of liquids, a Certus Flex (Fritz Gyger AG, Gwatt, Switzerland) was used, viscosity of printing solutions was adjusted and calibrated to assure reproducible and precise printing.

Preparation and Analysis of Hydrogels on Nanoliter-Scale

In a typical printing procedure 130 nL PBS (Thermo Fisher Scientific Inc., Waltham, MA) were dispensed to the outer frame of the droplet microarray to make sure every gel containing spot will be surrounded by other gel-containing spots or humidifying rows containing PBS. Then 30 nL lithium phenyl-2,4,6-trimethylbenzoylphosphinate (Sigma-Aldrich, St. Louis, MO) solution (5 mg/mL) in PBS, supplemented with glucose oxidase (40 µM) (VWR International, Radnor, PA) and glucose (0.1 M) (Sigma-Aldrich, St. Louis, MO) were dispensed into the inner spots. 60 nL of monomer solution (1.66 M) and 30 nL cross-linker solution (0.581 M) in PBS or DMF were added subsequently. For larger libraries, the slide was stored on a metal cooling plate at 0 °C during the exchange of stock solutions to fully suppress evaporation-induced concentration changes.

After printing, the slides containing prepolymerization mixture were transferred into a petri dish containing 2 mL PBS in the bottom, covered with a quartz glass plate, and irradiated for 30 min with a UV LED (Opsytec, Ettlingen, Germany) at 5.41 mW/cm^2.

After the polymerization Slides were taken out of the dish and submerged in a solution of Rhodamine 6G (10 mg/L) in PBS for 16 h.

Swollen hydrogel pads were taken out of solution, excess solvent was carefully removed and the slide was sealed with a PDMS frame stuck to a quartz glass slide. The sealed slide was irradiated with the quartz glass slide pointing towards the light source. As UV source a UVA Cube 2000 (Dr. Hönle AG, Gilching, Germany) was used (11.45 mW/cm^2). and with a regular frequency imaged by fluorescence microscopy on a Keyence BZ-X800 with a 2X magnification lense (Keyence Co., Ösaka, Japan) in the TRITC channel (Excitation 544 nm, Emission 570 nm) at 4 ms excitation time. The recorded images were segmented and analyzed to determine the fluorescence area and the integrated intensity of every single pad.[1]

Preparation and Analysis of Hydrogels on Microliter-Scale

To a solution of monomer (0.89 M) and crosslinker (from 5 to 15 mol% w.r.t. Monomer) in PBS and DMF, LAP was added (1.13 mg/mL). Nitrogen was bubbled through the mixture for 15 min to remove oxygen, then the Prepolymerization mixture was ready to use for the following experiments. The hydrogels were prepared by dispensing 150 µL prepolymerization mixture into an PTFE mold, which was then covered with a quartz glass plate and irradiated according to the polymerization protocol. The gel pads were taken out of the mold and submerged in PBS for 7 days to achieve full swelling. Samples were taken out and dried of excess water using tissues. The samples were irradiated in a close petri dish with 2 mL PBS in the bottom under the same conditions as for the sub-microliter degradation studies. After specific time intervals, the samples were taken out, liquefied parts were removed again and the sample was weighed. The mass change was measured over 20 min and the mass was normalized to the starting mass to generate the course of degradation. For every measurement, three independent repetitions were performed.[1]

Image Analysis

Fluorescence microscopy images were evaluated with an in-house developed software tool for automatic droplet grid- and edge-detection, featuring a graphical user interface for supervision and adjustment. The code is available at https://github.com/aimat-lab/microdroplet_segmentation. For edge detection, a sobel filter with median and gaussian blurring from scikit-image was chosen.[140, 141] After droplet segmentation with a two-label watershed algorithm within each array box on the sobel elevation map,[142-144] the pixel size and integrated gray-scale intensities of each droplet were recorded. The script was written by Dr. *PATRICK REISSER*.[1]

Photolinker Attachment and Deprotection

Fmoc-Photolinker at certain concentration, diisopropyl carbodiimide (DIC, 10 %, v/v) and 1-hydroxybenzotriazol (HOBT, same concentration as Fmoc-Photolinker) were dissolved in N-methyl-2-pyrrolidone (NMP) to prepare the photolinker solution. To immobilize the linker onto the surface of the hydrophilic spots, certain volume (300 nL for 1.4 mm pattern and 3 µL for 2.8 mm pattern, 150 nL for 900 µm pattern) of photolinker solution was dispensed. Then the slides were placed in a Petri dish and protected from light. The reaction was carried out overnight at rt, followed by washing with ethanol/acetone, and drying with nitrogen flow. The unreacted free amines on the surface were capped with 10% vol pyridine in acetic anhydride for 10 min at rt. The slides were again washed and dried. To deprotect the photolinker, the whole slide was submerged in a solution of piperidine in DMF (20%, v/v) for 30 min. Afterwards the slide was washed with acetone and used directly.

UGI-Reaction Protocol

The three different Components (Carboxylic acid, aldehyde and isocyanide) were first dissolved in GBL/EG (9:1, v:v). Then, 100 nL of aldehydes solution and 100 nL were added (1 µL for 2.8 mm spots) to each spot and the reaction was preincubated for 2 h at rt in a Petri dish protected from light. Then 100 nL of acid and isocyanide solution was printed to the spots (1 µL for 2.8 mm spots) to let the reaction continue overnight at rt in dark. After the reaction was finished, the slides were washed thoroughly by acetone and ethanol, and immersed in ethanol on a shaker at 200 rpm for at least 4h.

Aminoacid Immobilization Protocol

The hydrophilic spots of a DMA modified with photolinker solution were treated with a solution of Fmoc-amino acid and HOBT (equimolar amount) in a mixture of NMP/DIC (9:1, v/v) (150 nL for 900 µm spots, 300 nL for 1.4 mm spots, 3 µL for 2.8 mm spots). The reaction proceeded overnight, then the solution was washed off with acetone and the slide was dried with nitrogen flow.

Deprotection of Immobilized Aminoacids

Slides modified with surface bound aminoacids were submerged in a solution of piperidine in DMF (20%, v/v) for 1 h. Afterwards, the slides were washed with acetone and dried under nitrogen flow.

Attachment of 3,4-Difluoro-2-(2-fluoro-4-iodophenylamino)benzoic acid (4)

The hydrophilic spots of a DMA modified with deprotected aminoacids were treated with a solution of 3,4-Difluoro-2-(2-fluoro-4-iodophenylamino)benzoic acid (**4**) and HOBT (100 mM, respectively) in a mixture of NMP/DIC (9:1, v/v) (150 nL for 900 µm spots, 300 nL for 1.4 mm spots, 3 µL for 2.8 mm spots). The reaction proceeded overnight, then the solution was washed off with acetone and the slide was dried with nitrogen flow.

SUZUKI-Reaction Protocol

To the hydrophilic spots of a DMA modified with aromatic iodides, a solution of sodium tetrachloropalladat(II) (0.2 M) in water (1.5 µL on 2.8 mm pattern, 60 nL on 1.4 mm pattern, 40 nL on 900 µm pattern) and a solution of *N*,*N*-diisopropyl-dibenzoylphosphinate (0.5 M) in NMP (1.5 µL on 2.8 mm pattern, 60 nL on 1.4 mm pattern, 40 nL on 900 µm pattern) were added and preincubated to form the catalytic active species for 15 min at rt. Afterwards, a solution of boronic acid (0.5 M) in NMP (3.0 µL on 2.8 mm pattern, 120 nL on 1.4 mm pattern, 80 nL on 900 µm pattern) and aqueous sodium carbonate solution (sat.) (2.0 µL on 2.8 mm pattern, 60 nL on 1.4 mm pattern, 40 nL on 900 µm pattern) are added and the reaction is conducted at rt over night. The slide is afterwards washed with water and ethanol, then submerged in a solution of potassium cyanide (0.1 M) in a mixture of DMSO/water (1:1, v:v) for 3 h. The slide is again washed with water and ethanol and then dried under nitrogen flow.

Photorelease of Compounds

To release the compounds off the solid phase, DI water is added to each spot of the DMA (5 µL for 2.8 mm pattern, 150 nL for 1.4 mm pattern, 100 nL for 900 µm pattern) and the slide is enclosed in a petri dish. The slide is then irradiated using a Biolink BLX UV chamber (Witec, Sursee, Switzerland) at 365 nm (2.19 mW/cm^2) for different times. Afterwards, the water is evaporated and the sample can be extracted.

LC-MS Sample Preparation from DMA

To the irradiated 2.8 mm spots of a DMA 5 µL DMF were added and the liquid was collected. Then 5 µL DI-water were added to these spots, to dissolve any hydrophilic compounds, and combined with the organic phase. For every measurement, 5 repetitions of those 10 µL samples were collected into one, then 10 µL of this solution was injected for LC-MS measurements. Standard compounds were prepared as stock solution (10 mM) in DMSO or acetonitrile and were then serial diluted with water to get different concentrations for the calibration. Calibration curves were recorded using the same HPLC- and MS-methods as for the DMA samples and ranged from 10 to 10000 µM.

MALDI-TOF-MS Measurements on Target Plate

Each compound was synthesized in duplicates and extracted from the poly(HEMA-*co*-EDMA) slides using 1 µL of DMF/Water (2:1) per spot and transferred onto a ground steel MALDI target plate. 2,5-Dihydroxybenzoic acid (DHB) as matrix was sprayed onto the target plate using an HTX M5 sprayer (HTX Tech., Chapel Hill, NC, USA) Therefore 20 mg/ml of DHB was dissolved in 50 % acetonitrile/H_2O (v/v) supplemented with 2.5 % TFA (v/v). Mass spectra were recorded on a rapifleX MALDI TOF system (Bruker Daltonics) in reflector positive ion mode or negative ion mode, covering a mass range of m/z 500 to 1400 or m/z 300 to 2000. Accordingly, the laser power was set to 51% or 40%, having a laser field size of 100 µm (Smartbeam parameter M5). The acquisition mode was set to random walk with 20 different positions with 500 laser shots, resulting in a total of 10000 shots, per target spot and a repetition rate of 10kHz. Mass calibration was performed using peptide calibration standard II by a quadratic correction.

In order to validate results, the synthesis of the priorly identified target molecules was confirmed by a measurement using the timsTOF flex mass spectrometer (Bruker Daltonics). Hereby, ion profiles were rapidly acquired and analyzed for the occurrence of $[M+H]^+$, $[M+Na]^+$ and $[M+K]^+$ in synthesis screening mode using timsTOF MALDI PharmaPulse 2023 software (Bruker Daltonics) with an extraction tolerance of 10 mDa. For each mass spectrum recorded in a mass range of m/z 600 to 1540, ion intensities resulting from 5000 laser shots were accumulated at a repetition rate of 10kHz and a laser power of 60%. Calibration of the mass spectrometer was done using the electrospray ion source using molecules from ESI tune mix in cubic enhanced mode. Measurements were performed by Dr. *STEFAN SCHMIDT* (CeMOS).

For in-depth verification of synthesized compounds, selected molecules were identified by their unique fragmentation spectra. MS/MS was performed on a solariX 7T XR Fourier transform Ion Cyclotron Resonance (FT-ICR) mass spectrometer (Bruker Daltonics GmbH, Bremen, Germany) with a smartbeam II 2 kHz laser using ftms control 2.3.0 software. Mass spectra were acquired in negative ion mode using 'single MS mode' over a m/z range from 100-1200, accumulating 100 shots with a laser intensity of 30% and a frequency of 2000 Hz, with a mass resolution at m/z 400 of approximately 150000. The isolation window of the target masses was set to +- 3 Da.

MALDI-TOF-MS-Imaging on ITO-coated HEMA-*co*-EDMA DMAs

Chemical library screening of in total 325 MEK-inhibitors was performed by Matrix-Assisted Laser Desorption/Ionization Mass Spectrometry Imaging (MALDI-MSI). The use of a timsTOF fleX mass spectrometer (Bruker Daltonics GmbH, Bremen, Germany) with its orthogonal trap geometry enabled us to perform identification of the synthesis compounds directly from the HEMA-co-EDMA syntheses slide for the first time. To this end, 42.0 nmol of N-(1-naphthyl) ethylenediamine dihydrochloride (NEDC) matrix was deposited automatically on each spot by use of a liquid dispensing system (CERTUS

FLEX, Fritz Gyger AG, Gwatt, Switzerland) followed by MALDI-TOF MSI. MALDI-TOF MSI measurements were performed on a timsTOF fleX (Bruker Daltonics GmbH, Bremen, Germany) in negative ion mode with a lateral step size and laser spot size of 100 µm each, 400 laser shots per pixel and a repetition rate of 10,000 Hz, with a laser intensity of 75%. The 'focus pre TOF' parameters 'prepulse storage' and 'transfer time' were set to 10 µs and 110 µs, respectively. The collision cell RF was set to 25000.0 Vpp, with a collision cell energy offset of -10 V. Funnel 0 RF was set to 200 Vpp and Funnel 1 Rf to 350 Vpp.

Prior to MSI data acquisition, external mass calibration was performed *via* the electrospray ionization source using ESI-Low Concentration Tuning Mix (Agilent Technologies, Santa Clara, USA) and an enhanced quadratic calibration model.

LC-MS Measurements

Liquid Chromatography coupled Mass Spectroscopy (LC-MS) measurements were performed on an Agilent 1260 Infinity II system consisting of a quaternary pump (GB7111B;), autosampler (G7129A, 100 µL sample loop), a temperature-controlled column oven (G7114A) and a variable UV-VIS detector (G7114 A, VWD, flow cell G7114A 018, d = 10 mm, V = 14 µL). Separation was performed on a C18 HPLC-column (Agilent Poroshell 120 EC-C18 4,6x100mm, 2,7µm) operating at 40 °C. A gradient of ACN:H_2O 10:90 – 80:20 v/v (additive 10 mmol L-1 $NH_4CH_3CO_2$) at a flow rate of 1 mL/min during 15 min was used as the eluting solvent. The flow was directed into an Agilent MSD (G6136BA, AP-ESI ion source). The instrument was calibrated in the m/z range 118-2121 in the positive mode and 113-2233 in the negative using a premixed calibration solution (Agilent). The following parameters were used: spray chamber flow: 12 L/min; drying gas temperature: 350 K, Capillary Voltage: 3000 V, Fragmentor Voltage: 100 V.

Optimization of HT-29 Seeding Conditions using CCK8

For the optimization of the seeding conditions of human colon cancer cells HT-29 on DMA, a DMA (1.4 mm pattern) was prepared and modified with different photolinker solutions (concentration between 0 to 100 mM). The slide was irradiated for 40 min to cleave the surface functionalities and washed with acetone. The slide was submerged in ethanol (70 %) for 30 min and dried under sterile conditions. 1000 nL cell suspension (HT-29 cells, 0.0-5.0·10^6 cells/mL) in DMEM (0.1 % P/S, v/v; 10 % FBS, v/v; 0.1 % DMSO, v/v) was added to each spot. The slide was incubated at 37 °C for 72 h, then 100 nL CCK8 were added to each spot and the slide was incubated at 37 °C for 1 h. The slide was then imaged using a document scanner CanoScan 8800F from CANON Deutschland GmbH (Krefeld, Germany) at 70% exposure and 6400 dpi. The images were analyzed using MatLab for the overall color intensity in the spot.

Optimization of HT-29 Screening Protocol using PI-Staining

For the optimization of the screening conditions of human colon cancer cells HT-29 on DMA, a DMA (1.4 mm pattern) was prepared and modified with photolinker solution (10 mM). The slide was irradiated for 40 min to cleave the surface functionalities and washed with acetone. The slide was submerged in ethanol (70 %) for 30 min and dried under sterile conditions. 1000 nL DMEM (+0.1 % P/S, 10 % FBS, 0.1 % DMSO, v/v) or 1000 nL cell suspension (HT-29 cells, 3.0·10^5 cells/mL) in DMEM (0.1 % P/S, v/v; 10 % FBS, v/v; 0.1 % DMSO, v/v) was added to each spot. The slide was incubated at 37 °C for 72 h, then 100 nL PI solution (10 µg/mL) was added to each spot and the slide was incubated at 37 °C for 15 min. Each spot was then imaged with a Leica Thunder 3D Imager (Leica Camera AG, Wetzlar, Germany) at 20x magnification. The number of dead cells was calculated using ImageJ automatic particle counting.

Optimized Screening Protocol using PI-Staining

To the slides containing compounds, 700 nL (to compound containing spots and negative control spots) or 350 nL (to positive control spots) of DMEM (1 % P/S, v/v; 0.15 % DMSO, v/v) were added. The slide was sealed in a petri dish, containing 2 mL PBS in the bottom and was then irradiated for 5-40 min. Afterwards, 350 nL of control compound (28.6 µM) in DMEM (1 % P/S, v/v, 0.15 % DMSO, v/v) were added to the positive control spots. A humidifying pad was added to the lid of the petri dish and soaked with 5 mL PBS, the slide was then preincubated overnight to dissolve the compounds. 300 nL cell suspension (HT-29 cells, 1.0·10^6 cells/mL) in DMEM (1 % P/S, v/v; 30 % FBS, v/v;)

was added to each spot. The slide was incubated at 37 °C for 72 h, then 100 nL PI solution (10 µg/mL) in PBS was added to each spot and the slide was incubated at 37 °C for 15 min. Each spot was then imaged with a Leica Thunder 3D Imager (Leica Camera AG, Wetzlar, Germany) at 20X magnification. The number of dead cells was calculated using ImageJ's automatic particle counting feature.

NMR Measurements

^{1}H and ^{13}C NMR spectra were recorded on a Bruker Avance III HD 500 MHz spectrometer at 400 MHz for ^{1}H NMR and 100 MHz for ^{13}C NMR at 298K. Chemical shifts (ppm) are reported relative to TMS using the solvent peak as reference.

High-Resolution Mass Spectrometry

Electron-spray ionization (ESI) mass spectrometry was performed on a ThermoFisher Scientific Q Exactive Orbitrap by LARA HIRSCH (IOC).

CELL TITER-GLO® Assay

15 µL of a solution of target compounds in the desired concentration dissolved in DMEM (1 % P/S, v/v, 0.15 % DMSO, v/v) were predispensed into wells of a 384 well plate. Wells for negative controls contained no compound, wells for blank measurements contained 25 µL of the same medium. Then, 10 µL of a suspension of HT-29 human colon cancer cells ($5 \cdot 10^5$ cells/mL) were dispensed to all wells exluding the blank measurement wells. The well plate was closed and incubated for 72 h at 37 °C, then equilibrated at rt for 30 min. 25 µL of a solution of CELL TITER-GLO® were added to each well, the plate was covered with aluminium foil and shaked for 2 at 50 rpm. The slide was then incubated for ten more min at rt. Luminescence was recorded using a CLARIOstar plus microplate reader (BMG Labtech). Blank values were subtracted from all other values and the measurements were normalized to the negative control to obtain viability.

Preparation of Compound 1 (Chapter 2.2): N-(1-amino-1-oxopropan-2-yl)-3,4-difluoro-2-((2-fluoro-4-iodophenyl)amino)benzamide

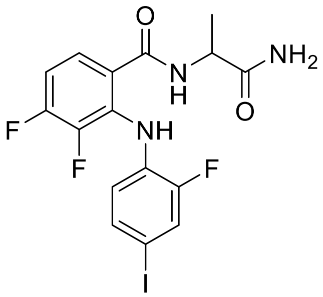

Exact Mass: 463,00
Molecular Weight: 463,20

75.0 mg 3,4-Difluoro-2-(2-fluoro-4-iodophenylamino)benzoic acid (**4**) (191 µmol, 1.00 Eq.) and 35.7 mg Alanine amide·HCl (286 µmol, 1.50 Eq.) were dissolved in 200 µL DMSO. 38.7 mg HOBT (286 µmol, 1.50 Eq.), 54.9 mg EDC·HCl (286 µmol, 1.50 Eq.) and 62.9 µL N-Methylmorpholine (57.9 mg, 572 µmol, 3.00 Eq.) were added and the mixture was stirred overnight. The crude mixture was poured into 1 mL DI water, the precipitate was filtrated and dried under vacuum to obtain compound **1** as pure white powder (65.1 mg, 74 %).

^{1}**H-NMR** (400 MHz, DMSO-d_6) δ [ppm]: 9.09 (s, 1H, N*H*Ar), 8.72 (d, 1H, CON*H*), 7.68-7.63 (m, 1H, H_{Ar}), 7.61-7.55 (m, 1H, H_{Ar}), 7.45 (s, 1H, NH_2), 7.05 (s, 1H, NH_2), 7.40-7.35 (m, 1H, H_{Ar}), 7.25-7.16 (m, 1H, H_{Ar}), 6.72-6.64 (m, 1H, H_{Ar}), 4.36-4.29 (m, 1H, C*H*), 1.28 (d, 3H, CH_3).

^{13}**C-NMR** (400 MHz, DMSO-d_6) δ [ppm]: 174.43, 168.8, 154.06, 152.1, 133.56, 132.02, 131.45, 125.68, 124.22, 124.04, 122.96, 120.47, 110.17, 82.64, 49.24, 18.22.

ESI-HRMS: calc. for $C_{16}H_{14}F_3IN_3O_2$ $[M+H]^+$: 464.0083; found: 464.008.

Preparation of Compound 2 (Chapter 2.2): N-(1-amino-1-oxopropan-2-yl)-3,4-difluoro-2-((3-fluoro-[1,1'-biphenyl]-4-yl)amino)benzamide

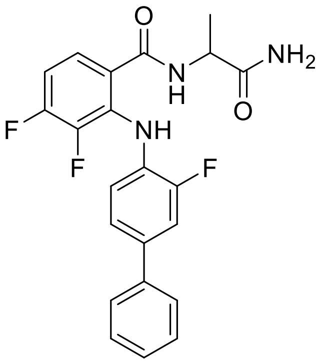

Exact Mass: 413,14
Molecular Weight: 413,40

A solution of 0.2 mg $Pd(OAc)_2$ (0.001 mmol, 0.01 Äq.) and 1.0 mg PPh_3 (0.005 mmol, 0.05 Äq.) in 3 mL THF/H_2O (9:1, v/v) was stirred for 10 min under argon atmosphere. 11.0 mg phenylboronic acid (0.092 mmol, 1.07 Äq), 32 mg amide **1** (0.086 mmol, 1.00 Äq) and 32.0 mg K_2CO_3 (0.231 mmol, 3.00 Äq.) were added carefully, afterwards the mixture was stirred under reflux for 16 h. The solvent was removed under reduced pressure and the crude was redissolved in ethyl acetate. The organic phase is washed with water and sodium bicarbonate solution, the aqueous phase is then back extracted with ethyl acetate and the combined organic layers are dried over sodium sulfate. The solvent is again removed under reduced pressure and the crude is purified *via* column chromatography (SiO_2, DCM:MeOH, 9:1) to obtain compound **2** as white powder (28.5 mg, 80%).

^{1}H-NMR (400 MHz, DMSO-d_6) δ [ppm]: 9.25 (s, 1H, N*H*Ar), 8.79 (d, 1H, CON*H*), 7.75-7.68 (m, 3H, H_{Ar}), 7.53-7.40 (m, 5H, H_{Ar}), 7.30-7.18 (m, 1H, H_{Ar}), 7.09 (s, 1H, NH_2), 7.04-6.95 (m, 1H, H_{Ar}), 4.45-4.35 (m, 1H, C*H*), 1.35 (d, 3H, CH_3).

^{13}C-NMR (400 MHz, DMSO-d_6) δ [ppm]: 174.21, 169.98, 154.82, 152.42, 139.13, 134.25, 130.38, 129.40, 127.70, 126.7, 125.80, 122.49, 119.00, 113.87, 113.67, 109.93, 109.70, 49.26, 18.22.

ESI-HRMS: calc. for $C_{22}H_{19}F_3N_3O_2$ $[M+H]^+$: 414.1429; found: 414.142.

Preparation of Compound 7 (Chapter 2.2): N-(1-amino-1-oxopropan-2-yl)-2-((4'-chloro-3-fluoro-[1,1'-biphenyl]-4-yl)amino)-3,4-difluorobenzamide

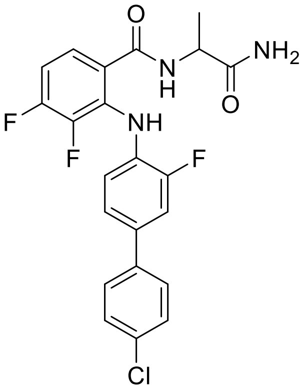

Exact Mass: 447,10
Molecular Weight: 447,84

A solution of 0.5 mg $Pd(OAc)_2$ (0.002 mmol, 0.01 Äq.) and 2.4 mg PPh_3 (0.009 mmol, 0.05 Äq.) in 3 mL THF/H_2O (9:1, v/v) was stirred for 10 min under argon atmosphere. 33.0 mg 4-chlorophenylboronic acid (0.208 mmol, 1.20 Äq), 80.0 mg amide **1** (0.173 mmol, 1.00 Äq) and 72.0 mg K_2CO_3 (0.519 mmol, 3.00 Äq.) were added carefully, afterwards the mixture was stirred under reflux for 16 h. The solvent was removed under reduced pressure and the crude was redissolved in ethyl acetate. The organic phase is washed with water and sodium bicarbonate solution, the aqueous phase is then back extracted with ethyl acetate and the combined organic layers are dried over sodium sulfate. The solvent is again removed under reduced pressure and the crude is purified *via* column chromatography (SiO_2, DCM:MeOH 9:1) to obtain compound **7** as white powder (19.2 mg, 25%).

^{1}H-NMR (400 MHz, d_6-Acetone) δ [ppm]: 9.35 (s, 1H, NH_{Ar}), 8.05 (d, 1H, CON*H*), 7.74-7.63 (m, 3H, H_{Ar}), 7.52-7.35 (m, 4H, H_{Ar}), 7.19-6.95 (m, 3H, NH_2+H_{Ar}), 6.52-6-48 (m, 1H, H_{Ar}), 4.61 (quin., 1H, C*H*CH_3), 1.42 (d, 3H, CH_3).

^{13}C-NMR (400 MHz, d_6-Acetone) δ [ppm]: 173.85, 166.96, 166.94, 154.96, 154.03, 153.92, 152.54, 151.55, 151.43, 141.85, 141.71, 138.24, 133.50, 132.70, 130.58, 130.46, 128.87, 128.00, 124.70, 124.66, 122.40, 121.42, 113.44, 113.24, 109.20, 109.02, 49.00, 17.71.

ESI-HRMS: calc. for $C_{22}H_{18}ClF_3N_3O_2$ $[M+H]^+$: 448.1040; found: 448.103

Preparation of Compound 8 (Chapter 2.2): N-(1-amino-1-oxopropan-2-yl)-2-((4-(1,3-dihydroisobenzofuran-4-yl)-2-fluorophenyl)amino)-3,4-difluorobenzamide

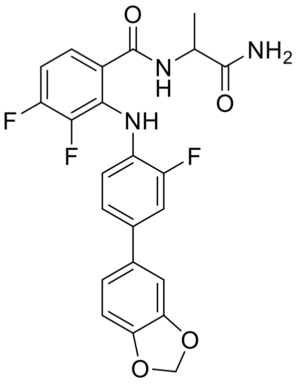

Exact Mass: 457,12
Molecular Weight: 457,41

A solution of 0.5 mg $Pd(OAc)_2$ (0.002 mmol, 0.01 Äq.) and 2.4 mg PPh_3 (0.009 mmol, 0.05 Äq.) in 3 mL THF/H_2O (9:1, v/v) was stirred for 10 min under argon atmosphere. 35.0 mg 3,4-(Methylenedioxy)phenylboronic acid (0.208 mmol, 1.20 Äq), 80.0 mg amide **1** (0.173 mmol, 1.00 Äq) and 72.0 mg K_2CO_3 (0.519 mmol, 3.00 Äq.) were added carefully, afterwards the mixture was stirred under reflux for 16 h. The solvent was removed under reduced pressure and the crude was redissolved in ethyl acetate. The organic phase is washed with water and sodium bicarbonate solution, the aqueous phase is then back extracted with ethyl acetate and the combined organic layers are dried over sodium sulfate. The solvent is again removed under reduced pressure and the crude is purified *via* column chromatography (SiO_2, DCM:MeOH 9:1) to obtain compound **7** as white powder (10.9 mg, 12%).

^{1}H-NMR (400 MHz, d_6-Acetone) δ [ppm]: 9.32 (s, 1H, NH_{Ar}), 8.05 (d, 1H, CON*H*), 7.74-7.51 (m, 2H, H_{Ar}), 7.42-7.36 (m, 1H, H_{Ar}), 7.33-7.28 (m, 1H, H_{Ar}), 7.18-7.08 (m, 3H, H_{Ar}), 7.08-6.85 (m, 3H, NH_2+H_{Ar}), 6.53-6.45 (m, 1H, H_{Ar}), 6.03 (s, 1H, CH_2), 4.61 (quin., 1H, C*H*CH_3), 1.42 (d, 3H, CH_3).

^{13}C-NMR (400 MHz, d_6-Acetone) δ [ppm]: 173.87, 167.02, 169.99, 148.42, 147.21, 135.02, 134.95, 133.45, 131.85, 131.75, 128.62, 128.50, 124.68, 122.09, 119.98, 118.96, 113.27, 113.08, 108.89, 108.71, 108.46, 106.82, 101.33, 49.00, 17.71.

ESI-HRMS: calc. for $C_{23}H_{19}F_3N_3O_4$ $[M+H]^+$: 458.1328; found: 458.132

5 References

[1] Seifermann, M.; Reiser, P.; Friederich, P.; Levkin, P. A., *Small Methods* **2023**, e2300553.

[2] Tian, Y.; Seifermann, M.; Bauer, L.; Luchena, C.; Wiedmann, J. J.; Schmidt, S.; Geisel, A.; Afonin, S.; Hopfner, J.; Brehm, M.; Liu, X.; Hopf, C.; Popova, A. A.; Levkin, P. A., *Small* **2024**, e2307215.

[3] Zheng, T.; Xia, C., *Trends. Chem.* **2023,** *5* (1), 7-10.

[4] Koytsoumpa, E. I.; Bergins, C.; Kakaras, E., *J. Supercrit. Fluids* **2018,** *132*, 3-16.

[5] Linthorst, J. A., *Found. Chem.* **2009,** *12* (1), 55-68.

[6] Brzezinska, J.; Trzcinski, S.; Strzelec, J.; Chmielewski, M. K., *Bioorg. Chem.* **2023,** *140*, 106806.

[7] Labadie, J. W., *Curr. Opin. Chem. Biol.* **1998,** *2* (3), 346-52.

[8] Doran, T. M.; Dickson, P.; Ndungu, J. M.; Ge, P.; Suponitsky-Kroyter, I.; An, H.; Kodadek, T., *Methods Enzymol.* **2019,** *622*, 91-127.

[9] Liang, R.; Yan, L.; Loebach, J.; Ge, M.; Uozumi, Y.; Sekanina, K.; Horan, N.; Gildersleeve, J.; Thompson, C.; Smith, A.; Biswas, K.; Still, W. C.; Kahne, D., *Science* **1996,** *274* (5292), 1520-2.

[10] Shin, D. S.; Kim, D. H.; Chung, W. J.; Lee, Y. S., *J. Biochem. Mol. Biol.* **2005,** *38* (5), 517-25.

[11] Wittmann, V.; Seeberger, S., *Angew. Chem. Int. Ed.* **2000,** *39* (23), 4348-4352.

[12] Gesmundo, N.; Dykstra, K.; Douthwaite, J. L.; Kao, Y.-T.; Zhao, R.; Mahjour, B.; Ferguson, R.; Dreher, S.; Sauvagnat, B.; Saurí, J.; Cernak, T., *Nat. Synth.* **2023**.

[13] Buitrago Santanilla, A.; Regalado, E. L.; Pereira, T.; Shevlin, M.; Bateman, K.; Campeau, L. C.; Schneeweis, J.; Berritt, S.; Shi, Z. C.; Nantermet, P.; Liu, Y.; Helmy, R.; Welch, C. J.; Vachal, P.; Davies, I. W.; Cernak, T.; Dreher, S. D., *Science* **2015,** *347* (6217), 49-53.

[14] Shaabani, S.; Xu, R.; Ahmadianmoghaddam, M.; Gao, L.; Stahorsky, M.; Olechno, J.; Ellson, R.; Kossenjans, M.; Helan, V.; Domling, A., *Green Chem.* **2019,** *21* (2), 225-232.

[15] Niessen, W. M., *J. Chromatogr. A* **2003,** *1000* (1-2), 413-36.

[16] Korhammer, S. A.; Bernreuther, A., *Fresenius J. Anal. Chem.* **1996,** *354* (2), 131-135.

[17] Pu, F.; Elsen, N. L.; Williams, J. D., *ACS Med. Chem. Lett.* **2020,** *11* (11), 2108-2113.

[18] Jemal, M., *Biomed. Chromatogr.* **2000,** *14* (6), 422-429.

[19] Pereira, D. A.; Williams, J. A., *Br. J. Pharmacol.* **2007,** *152* (1), 53-61.

[20] Agnew, H. D.; Rohde, R. D.; Millward, S. W.; Nag, A.; Yeo, W. S.; Hein, J. E.; Pitram, S. M.; Tariq, A. A.; Burns, V. M.; Krom, R. J.; Fokin, V. V.; Sharpless, K. B.; Heath, J. R., *Angew. Chem. Int. Ed. Engl.* **2009,** *48* (27), 4944-8.

[21] Gehrtz, P.; Marom, S.; Buhrmann, M.; Hardick, J.; Kleinbolting, S.; Shraga, A.; Dubiella, C.; Gabizon, R.; Wiese, J. N.; Muller, M. P.; Cohen, G.; Babaev, I.; Shurrush, K.; Avram, L.; Resnick, E.; Barr, H.; Rauh, D.; London, N., *J. Med. Chem.* **2022,** *65* (15), 10341-10356.

[22] Sutanto, F.; Shaabani, S.; Oerlemans, R.; Eris, D.; Patil, P.; Hadian, M.; Wang, M.; Sharpe, M. E.; Groves, M. R.; Domling, A., *Angew. Chem. Int. Ed. Engl.* **2021,** *60* (33), 18231-18239.

[23] Schober, A.; Schlingloff, G.; Gro, A.; Henkel, T.; Albert, J.; Mayer, G.; Wurziger, H.; Dring, M.; Tietz, H., *Microsyst. Technol.* **2004,** *10* (4), 281-292.

[24] Sinha, A.; Gopinathan, P.; Chung, Y. D.; Lin, H. Y.; Li, K. H.; Ma, H. P.; Huang, P. C.; Shiesh, S. C.; Lee, G. B., *Biosens. Bioelectron.* **2018,** *122*, 104-112.

[25] Jothi Prakash, C. G.; Prasanth, R., *J. Mater. Sci.* **2021,** *56* (1), 108-135.

[26] *Philos. Trans. R. Soc. Lond.* **1997,** *95*, 65-87.

[27] Mądry, K.; Nowicki, W., *Eur. Phys. J. E Soft Matter* **2021,** *44* (11).

[28] Wenzel, R. N., *Ind. Eng. Chem.* **1936,** *28* (8), 988-994.

[29] Cassie, A. B. D.; Baxter, S., *Trans. Faraday Soc.* **1944,** *40*, 546-551.

[30] Zhang, M.; Feng, S.; Wang, L.; Zheng, Y., *Biotribology* **2016,** *5*, 31-43.

[31] Lu, L.; Yao, W.; Xie, Y.; Li, K.; Wan, Z., *Surf. Coat. Technol.* **2021,** *405*.

[32] Li, K.; Xie, Y.; Lei, J.; Zhang, S.; Liu, Z.; Lu, L., *Surf. Coat. Technol.* **2021,** *427*.

[33] Du, X.; Xin, B.; Xu, J.; Wang, C., *Colloids Surf. A: Physicochem. Eng. Asp.* **2021,** *612*.

[34] Jokinen, V.; Sainiemi, L.; Franssila, S., *Adv. Mater.* **2008,** *20* (18), 3453-3456.

[35] Geyer, F. L.; Ueda, E.; Liebel, U.; Grau, N.; Levkin, P. A., *Angew. Chem. Int. Ed. Engl.* **2011,** *50* (36), 8424-7.

[36] Liu, Y.; Tronser, T.; Peravali, R.; Reischl, M.; Levkin, P. A., *Adv. Biosyst.* **2020,** *4* (3), e1900257.

[37] Feng, W.; Li, L.; Ueda, E.; Li, J.; Heißler, S.; Welle, A.; Trapp, O.; Levkin, P. A., *Adv. Mater. Interfaces* **2014,** *1* (7).

[38] Cui, H.; Wang, X.; Wesslowski, J.; Tronser, T.; Rosenbauer, J.; Schug, A.; Davidson, G.; Popova, A. A.; Levkin, P. A., *Adv. Mater.* **2021,** *33* (4), e2006434.

[39] Benz, M.; Asperger, A.; Hamester, M.; Welle, A.; Heissler, S.; Levkin, P. A., *Nat. Commun.* **2020,** *11* (1), 5391.

[40] Neises, B.; Steglich, W., *Angew. Chem. Int. Ed.* **1978,** *90* (7), 556-557.

[41] Popova, A. A.; Dietrich, S.; Huber, W.; Reischl, M.; Peravali, R.; Levkin, P. A., *SLAS Technol.* **2021,** *26* (3), 274-286.

[42] Kapalczynska, M.; Kolenda, T.; Przybyla, W.; Zajaczkowska, M.; Teresiak, A.; Filas, V.; Ibbs, M.; Blizniak, R.; Luczewski, L.; Lamperska, K., *Arch. Med. Sci.* **2018,** *14* (4), 910-919.

[43] Cui, H.; Tronser, T.; Wang, X.; Wesslowski, J.; Davidson, G.; Popova, A. A.; Levkin, P. A., *Droplet* **2022,** *2* (1).

[44] Liu, Y.; Bertels, S.; Reischl, M.; Peravali, R.; Bastmeyer, M.; Popova, A. A.; Levkin, P. A., *Adv. Healthc. Mater.* **2022,** *11* (18), e2200718.

[45] Lei, W.; Deckers, A.; Luchena, C.; Popova, A.; Reischl, M.; Jung, N.; Brase, S.; Schwartz, T.; Krimmelbein, I. K.; Tietze, L. F.; Levkin, P. A., *Adv. Biol.* **2022,** *6* (12), e2200166.

[46] Benz, M.; Molla, M. R.; Boser, A.; Rosenfeld, A.; Levkin, P. A., *Nat. Commun.* **2019,** *10* (1), 2879.

[47] Wiedmann, J. J.; Demirdogen, Y. N.; Schmidt, S.; Kuzina, M. A.; Wu, Y.; Wang, F.; Nestler, B.; Hopf, C.; Levkin, P. A., *Small* **2023,** *19* (9), e2204512.

[48] Rosenfeld, A.; Brehm, M.; Welle, A.; Trouillet, V.; Heissler, S.; Benz, M.; Levkin, P. A., *Mater. Today Bio* **2019,** *3*, 100022.

[49] Wallbert, S.; Pfleiderer, W.; Steiner, U. E., *Helv. Chim. Acta* **2001,** *84*, 1601-1611.

[50] Neises, B.; Steglich, W., *Org. Synth.* **2003,** *63*, 93.

[51] Stuber, W.; Knolle, J.; Breipohl, G., *Int. J. Pept. Protein. Res.* **1989,** *34* (3), 215-21.

[52] Ugi, I.; Steinbrückner, C., *Angew. Chem.* **1960,** *72* (7-8), 267-268.

[53] Rocha, R. O.; Rodrigues, M. O.; Neto, B. A. D., *ACS Omega* **2020,** *5* (2), 972-979.

[54] Passerini, M., *Gazz. Chim. Ital.* **1921,** *51*, 181.

[55] Miyaura, N.; Suzuki, A., *J. Chem. Soc., CHem. Commun.* **1979,** (19).

[56] Farhang, M.; Akbarzadeh, A. R.; Rabbani, M.; Ghadiri, A. M., *Polyhedron* **2022,** *227*.

[57] Hopfner, J.; Brehm, M.; Levkin, P. A., *Small* **2023**, e2304325.

[58] Rosenfeld, A.; Oelschlaeger, C.; Thelen, R.; Heissler, S.; Levkin, P. A., *Mater. Today Bio* **2020,** *6*, 100053.

[59] Scarpa, J. S.; Mueller, D. D.; Klotz, I. M., *J. Am. Chem. Soc.* **1967,** *89* (24), 6024-6030.

[60] Fujishige, S.; Kubota, K.; Ando, I., *J. Phys. Chem.* **2002,** *93* (8), 3311-3313.

[61] Ebara, M.; Yamato, M.; Aoyagi, T.; Kikuchi, A.; Sakai, K.; Okano, T., *Biomacromolecules* **2004,** *5* (2), 505-510.

[62] Ebara, M.; Yamato, M.; Aoyagi, T.; Kikuchi, A.; Sakai, K.; Okano, T., *Adv. Mater.* **2008,** *20* (16), 3034-3038.

[63] Hatakeyama, H.; Kikuchi, A.; Yamato, M.; Okano, T., *Biomaterials* **2005,** *26* (25), 5167-5176.

[64] Hatakeyama, H.; Kikuchi, A.; Yamato, M.; Okano, T., *Biomaterials* **2006,** *27* (29), 5069-5078.

[65] Choi, C.; Chae, S. Y.; Nah, J.-W., *Polymer* **2006,** *47* (13), 4571-4580.

[66] Pan, Y.; Bao, H.; Sahoo, N.; Wu, T.; Li, L., *Adv. Funct. Mater.* **2011,** *21* (14), 2754-2763.

[67] Wei, H.; Cheng, S.; Zhang, X.; Zhuo, R., *Prog. Polym. Sci.* **2009,** *34* (9), 893-910.

[68] Liu, L.; Ghaemi, A.; Gekle, S.; Agarwal, S., *Adv. Mater.* **2016,** *28* (44), 9792-9796.

[69] Nagase, K.; Okano, T.; Kanazawa, H., *Nano-Struct.* **2018,** *16*, 9-23.

[70] Xue, P.; Valenzuela, C.; Ma, S.; Zhang, X.; Ma, J.; Chen, Y.; Xu, X.; Wang, L., *Adv. Funct. Mater.* **2023,** *33* (24), 2214867.

[71] Gaud, V.; Rougé, F.; Gnanou, Y.; Desvergne, J.-P., *React. Funct. Polym.* **2012,** *72* (8), 521-532.

[72] Chen, Q.; Yang, Q.; Gao, P.; Chi, B.; Nie, J.; He, Y., *Ind. Eng. Chem. Res.* **2019,** *58* (8), 2970-2975.

[73] Goulet-Hanssens, A.; Barrett, C. J., *J. Polym. Sci., Part A: Polym. Chem.* **2013,** *51* (14), 3058-3070.

[74] Pu, S.-Z.; Sun, Q.; Fan, C.-B.; Wang, R.-J.; Liu, G., *J. Mater. Chem. C* **2016,** *4* (15), 3075-3093.

[75] Keyvan Rad, J.; Balzade, Z.; Mahdavian, A. R., *J. Photochem. Photobiol. C: Photochem.* **2022,** *51*, 100487.

[76] Sinawang, G.; Wu, B.; Wang, J.; Li, S.; He, Y., *Macromol. Chem. Phys.* **2016,** *217* (21), 2409-2414.

[77] Batalov, I.; Stevens, K. R.; DeForest, C. A., *Proc. Natl. Acad. Sci. U. S. A.* **2021,** *118* (4).

[78] Francis, W.; Dunne, A.; Delaney, C.; Florea, L.; Diamond, D., *Sens. Actuators B Chem.* **2017,** *250*, 608-616.

[79] Wang, P., *Asian J. Org. Chem.* **2013,** *2* (6), 452-464.

[80] Görner, H., *Phys. Chem. Chem. Phys.* **2001,** *3* (3), 416-423.

[81] Bojtár, M.; Kormos, A.; Kis-Petik, K.; Kellermayer, M.; Kele, P., *Org. Lett.* **2019,** *21* (23), 9410-9414.

[82] Xi, H.; Zhang, Z.; Zhang, W.; Li, M.; Lian, C.; Luo, Q.; Tian, H.; Zhu, W.-H., *J. Am. Chem. Soc.* **2019,** *141* (46), 18467-18474.

[83] Karcher, J.; Kirchner, S.; Leistner, A.-L.; Hald, C.; Geng, P.; Bantle, T.; Gödtel, P.; Pfeifer, J.; Pianowski, Z. L., *RSC Adv.* **2021,** *11* (15), 8546-8551.

[84] Lerch, M. M.; Szymanski, W.; Feringa, B. L., *Chem. Soc. Rev.* **2018,** *47* (6), 1910-1937.

[85] Lee, S. C.; Kwon, I. K.; Park, K., *Adv. Drug. Deliv. Rev.* **2013,** *65* (1), 17-20.

[86] Guragain, S.; Bastakoti, B. P.; Malgras, V.; Nakashima, K.; Yamauchi, Y., *Chem. Eur. J.* **2015,** *21* (38), 13164-13174.

[87] Segler, M. H. S.; Preuss, M.; Waller, M. P., *Nature* **2018,** *555* (7698), 604-610.

[88] Liu, B.; Ramsundar, B.; Kawthekar, P.; Shi, J.; Gomes, J.; Luu Nguyen, Q.; Ho, S.; Sloane, J.; Wender, P.; Pande, V., *ACS Cent. Sci.* **2017,** *3* (10), 1103-1113.

[89] Coley, C. W.; Green, W. H.; Jensen, K. F., *Acc. Chem. Res.* **2018,** *51* (5), 1281-1289.

[90] Li, W.-X.; Tong, X.; Yang, P.-P.; Zheng, Y.; Liang, J.-H.; Li, G.-H.; Liu, D.; Guan, D.-G.; Dai, S.-X., *Aging* **2022,** *14* (3), 1448-1472.

[91] Xiong, H. Y.; Alipanahi, B.; Lee, L. J.; Bretschneider, H.; Merico, D.; Yuen, R. K. C.; Hua, Y.; Gueroussov, S.; Najafabadi, H. S.; Hughes, T. R.; Morris, Q.; Barash, Y.; Krainer, A. R.; Jojic, N.; Scherer, S. W.; Blencowe, B. J.; Frey, B. J., *Science* **2015,** *347* (6218), 1254806-1254806.

[92] Leung, M. K. K.; Xiong, H. Y.; Lee, L. J.; Frey, B. J., *Bioinformatics* **2014,** *30* (12), i121-i129.

[93] Riniker, S.; Wang, Y.; Jenkins, J. L.; Landrum, G. A., *J. Chem. Inf. Model.* **2014,** *54* (7), 1880-1891.

[94] Rouillard, A. D.; Hurle, M. R.; Agarwal, P., *PLOS Comput. Biol.* **2018,** *14* (5), e1006142.

[95] Iorio, F.; Knijnenburg, T. A.; Vis, D. J.; Bignell, G. R.; Menden, M. P.; Schubert, M.; Aben, N.; Goncalves, E.; Barthorpe, S.; Lightfoot, H.; Cokelaer, T.; Greninger, P.; van Dyk, E.; Chang, H.; de Silva, H.; Heyn, H.; Deng, X.; Egan, R. K.; Liu, Q.; Mironenko, T.; Mitropoulos, X.; Richardson, L.; Wang, J.; Zhang, T.; Moran, S.; Sayols, S.; Soleimani, M.; Tamborero, D.; Lopez-Bigas, N.; Ross-Macdonald, P.; Esteller, M.; Gray, N. S.; Haber, D. A.; Stratton, M. R.; Benes, C. H.; Wessels, L. F. A.; Saez-Rodriguez, J.; McDermott, U.; Garnett, M. J., *Cell* **2016,** *166* (3), 740-754.

[96] Raccuglia, P.; Elbert, K. C.; Adler, P. D. F.; Falk, C.; Wenny, M. B.; Mollo, A.; Zeller, M.; Friedler, S. A.; Schrier, J.; Norquist, A. J., *Nature* **2016,** *533* (7601), 73-76.

[97] Lu, S.; Zhou, Q.; Ouyang, Y.; Guo, Y.; Li, Q.; Wang, J., *Nat. Commun.* **2018,** *9* (1).

[98] Pilania, G.; Mannodi-Kanakkithodi, A.; Uberuaga, B. P.; Ramprasad, R.; Gubernatis, J. E.; Lookman, T., *Sci. Rep.* **2016,** *6* (1), 19375.

[99] Shields, B. J.; Stevens, J.; Li, J.; Parasram, M.; Damani, F.; Alvarado, J. I. M.; Janey, J. M.; Adams, R. P.; Doyle, A. G., *Nature* **2021,** *590* (7844), 89-96.

[100] Langner, S.; Hase, F.; Perea, J. D.; Stubhan, T.; Hauch, J.; Roch, L. M.; Heumueller, T.; Aspuru-Guzik, A.; Brabec, C. J., *Adv. Mater.* **2020,** *32* (14), e1907801.

[101] Macleod, B. P.; Parlane, F. G. L.; Morrissey, T. D.; Häse, F.; Roch, L. M.; Dettelbach, K. E.; Moreira, R.; Yunker, L. P. E.; Rooney, M. B.; Deeth, J. R.; Lai, V.; Ng, G. J.; Situ, H.; Zhang, R. H.; Elliott, M. S.; Haley, T. H.; Dvorak, D. J.; Aspuru-Guzik, A.; Hein, J. E.; Berlinguette, C. P., *Sci. Adv.* **2020,** *6* (20), eaaz8867.

[102] Krenn, M.; Pollice, R.; Guo, S. Y.; Aldeghi, M.; Cervera-Lierta, A.; Friederich, P.; Gabriel; Häse, F.; Jinich, A.; Nigam, A.; Yao, Z.; Aspuru-Guzik, A., *Nat. Rev. Phys.* **2022,** *4* (12), 761-769.

[103] Moosavi, S. M.; Jablonka, K. M.; Smit, B., *J. Am. Chem. Soc.* **2020,** *142* (48), 20273-20287.

[104] Flora, M. L.; Potvin, C. K.; Skinner, P. S.; Handler, S.; McGovern, A., *Mon. Weather Rev.* **2021,** *149* (5), 1535-1557.

[105] Reiser, P.; Neubert, M.; Eberhard, A.; Torresi, L.; Zhou, C.; Shao, C.; Metni, H.; Van Hoesel, C.; Schopmans, H.; Sommer, T.; Friederich, P., *Comm. Mater.* **2022,** *3* (1).

[106] Scheiger, J. M.; Li, S.; Brehm, M.; Bartschat, A.; Theato, P.; Levkin, P. A., *Adv. Funct. Mater.* **2021,** *31* (49), 2105681.

[107] Villiou, M.; Paez, J. I.; Del Campo, A., *ACS Appl. Mater. Interfaces* **2020,** *12* (34), 37862-37872.

[108] Frazier, P., *arXiv pre-print server* **2018**.

[109] Cancer, W. I. A. f. R. o. Estimated number of deaths in 2020, all cancers, both sexes, all ages. https://www.cancer.org/about-us/our-global-health-work/global-cancer-burden.html (accessed 25.08.2023).

[110] DeVita, V. T., Jr., *N. Engl. J. Med.* **1978,** *298* (16), 907-10.

[111] Wilson, B. E.; Jacob, S.; Yap, M. L.; Ferlay, J.; Bray, F.; Barton, M. B., *Lancet Oncol.* **2019,** *20* (6), 769-780.

[112] Tsimberidou, A. M.; Eggermont, A. M. M.; Schilsky, R. L., *Am. Soc. Clin. Oncol. Educ.* **2014,** *34* (34), 61-69.

[113] De Palma, M.; Hanahan, D., *Mol. Oncol.* **2012,** *6* (2), 111-27.

[114] Tsimberidou, A.-M., *Cancer Chemother. Pharmacol.* **2015,** *76* (6), 1113-1132.

[115] Dhillon, A. S.; Hagan, S.; Rath, O.; Kolch, W., *Oncogene* **2007,** *26* (22), 3279-90.

[116] Flaherty, K. T.; Puzanov, I.; Kim, K. B.; Ribas, A.; McArthur, G. A.; Sosman, J. A.; O'Dwyer, P. J.; Lee, R. J.; Grippo, J. F.; Nolop, K.; Chapman, P. B., *N. Engl. J. Med.* **2010,** *363* (9), 809-19.

[117] Kefford, R.; Arkenau, H.; Brown, M. P.; Millward, M.; Infante, J. R.; Long, G. V.; Ouellet, D.; Curtis, M.; Lebowitz, P. F.; Falchook, G. S., *J. Clin. Oncol.* **2010,** *28* (15_suppl), 8503-8503.

[118] Corcoran, R. B.; Ebi, H.; Turke, A. B.; Coffee, E. M.; Nishino, M.; Cogdill, A. P.; Brown, R. D.; Della Pelle, P.; Dias-Santagata, D.; Hung, K. E.; Flaherty, K. T.; Piris, A.; Wargo, J. A.; Settleman, J.; Mino-Kenudson, M.; Engelman, J. A., *Cancer Discov.* **2012,** *2* (3), 227-35.

[119] Han, J.; Liu, Y.; Yang, S.; Wu, X.; Li, H.; Wang, Q., *J. Hematol. Oncol.* **2021,** *14* (1).

[120] Zhao, Z.; Xie, L.; Bourne, P. E., *PLOS ONE* **2017,** *12* (6), e0179936.

[121] Wei, J.; Hu, J.; Wang, L.; Xie, L.; Jin, M. S.; Chen, X.; Liu, J.; Jin, J., *J. Med. Chem.* **2019,** *62* (23), 10897-10911.

[122] Gubler, H.; Schopfer, U.; Jacoby, E., *J. Biomol. Screen.* **2013,** *18* (1), 1-13.

[123] Wang, F.; Liigand, J.; Tian, S.; Arndt, D.; Greiner, R.; Wishart, D. S., *Anal. Chem.* **2021,** *93* (34), 11692-11700.

[124] Tanaka, R.; Tomosugi, M.; Sakai, T.; Sowa, Y., *Anticancer Res.* **2016,** *36* (9), 4537-43.

[125] Hopkins, A. L.; Groom, C. R., *Nat. Rev. Drug Disc.* **2002,** *1* (9), 727-730.

[126] Li, K.; Crews, C. M., *Chem. Soc. Rev.* **2022,** *51* (12), 5214-5236.

[127] Hershko, A.; Ciechanover, A., *Annu. Rev. Biochem.* **1992,** *61* (1), 761-807.

[128] Sakamoto, K. M.; Kim, K. B.; Kumagai, A.; Mercurio, F.; Crews, C. M.; Deshaies, R. J., *Proc. Natl. Acad. Sci. U. S. A.* **2001,** *98* (15), 8554-8559.

[129] Schneekloth, J. S.; Fonseca, F. N.; Koldobskiy, M.; Mandal, A.; Deshaies, R.; Sakamoto, K.; Crews, C. M., *J. Am. Chem. Soc.* **2004,** *126* (12), 3748-3754.

[130] Schneekloth, A. R.; Pucheault, M.; Tae, H. S.; Crews, C. M., *Bioorg. Med. Chem. Lett.* **2008,** *18* (22), 5904-5908.

[131] Wang, C.; Zhang, Y.; Wu, Y.; Xing, D., *Eur. J. Med. Chem.* **2021,** *225*, 113749.

[132] Wang, C.; Zhang, Y.; Wang, J.; Xing, D., *Eur. J. Med. Chem.* **2022,** *227*, 113906.

[133] Bricelj, A.; Steinebach, C.; Kuchta, R.; Gutschow, M.; Sosic, I., *Front. Chem.* **2021,** *9*, 707317.

[134] Tinworth, C. P.; Lithgow, H.; Dittus, L.; Bassi, Z. I.; Hughes, S. E.; Muelbaier, M.; Dai, H.; Smith, I. E. D.; Kerr, W. J.; Burley, G. A.; Bantscheff, M.; Harling, J. D., *ACS Chem. Biol.* **2019,** *14* (3), 342-347.

[135] Desantis, J.; Mammoli, A.; Eleuteri, M.; Coletti, A.; Croci, F.; Macchiarulo, A.; Goracci, L., *RSC Adv.* **2022,** *12* (34), 21968-21977.

[136] Cyrus, K.; Wehenkel, M.; Choi, E.-Y.; Han, H.-J.; Lee, H.; Swanson, H.; Kim, K.-B., *Mol. BioSyst.* **2011,** *7* (2), 359-364.

[137] Troup, R. I.; Fallan, C.; Baud, M. G. J., *Explor. Target. Anti-Tumor Ther.* **2020,** *1* (5).

[138] Brehm, M.; Heissler, S.; Afonin, S.; Levkin, P. A., *Small* **2020,** *16* (10).

[139] Levkin, P. A.; Grunze, M.; Dong, Z.; Demir, K.; Widmaier, S.; Brehm, M.; Popova, A. EP 3733277, 2020.

[140] Braski, G.; Kaehler, A., *Learning OpenCV: Computer Vision with the OpenCV Library*. O'Reilly Media Inc.: Sebastopol, California, 2008.

[141] van der Walt, S.; Schonberger, J. L.; Nunez-Iglesias, J.; Boulogne, F.; Warner, J. D.; Yager, N.; Gouillart, E.; Yu, T.; scikit-image, c., *PeerJ* **2014,** *2*, e453.

[142] Pedregosa, F.; Varoquaux, G.; Gramfort, A.; Michel, V.; Thirion, B.; Grisel, O.; Blondel, M.; Prettenhofer, P.; Weiss, R.; Dubourg, V.; Vanderplas, J.; Passos, A.; Cournapeau, D.; Brucher, M.; Perrot, M.; Duchesnay, E., *J. Mach. Learn. Res.* **2011,** *12*, 2825.

[143] Hunter, J. D., *Comput. Sci. Eng.* **2007,** *9*, 90.

[144] Neubert, P.; Protzel, P., In *International Conference on Pattern Recognition IEEE*, Piscataway, NJ, 2014; p 996.

6 Appendix

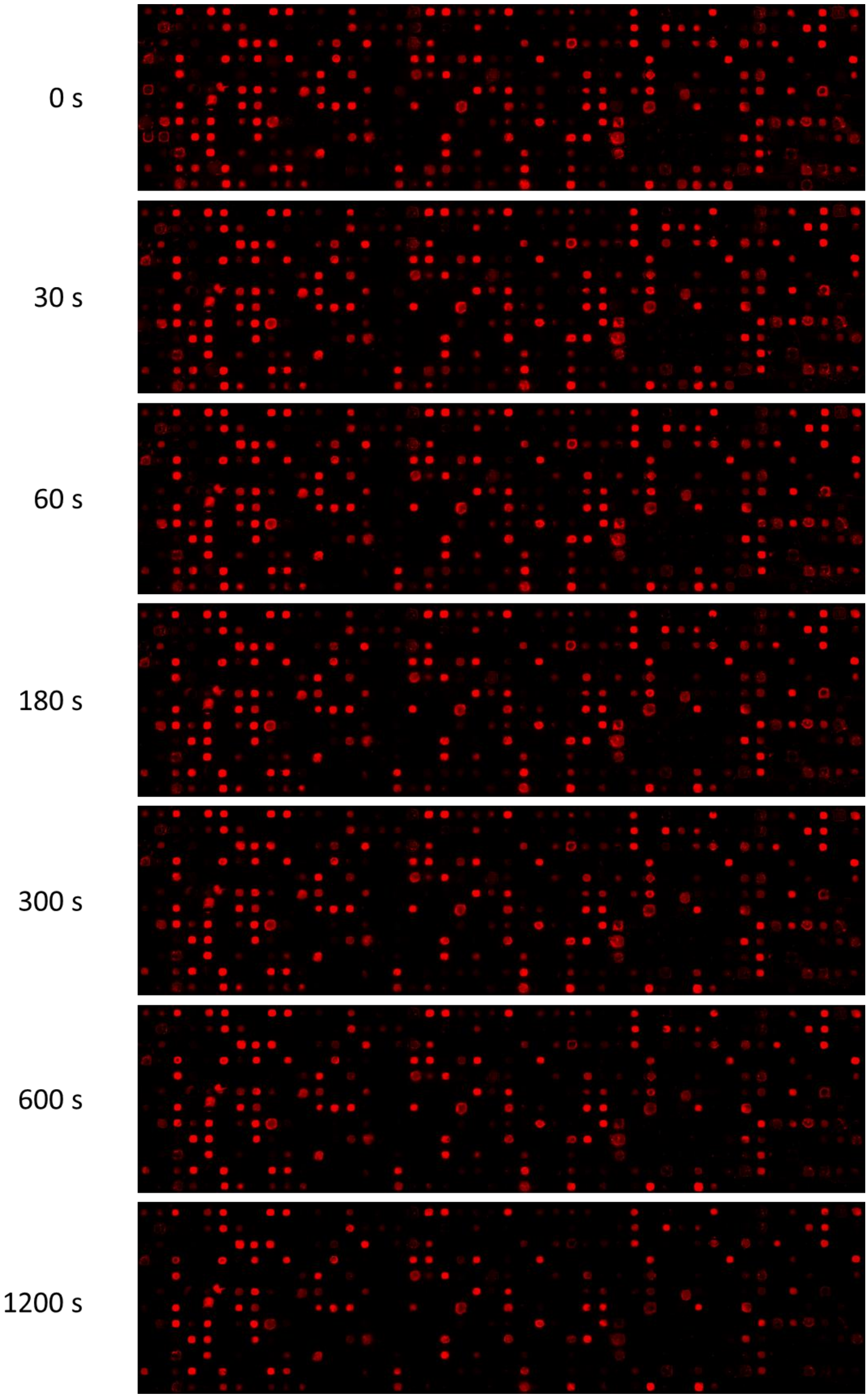
0 s
30 s
60 s
180 s
300 s
600 s
1200 s

Supporting Figure 1: Exemplary fluorescence microscopy images of a slide containing a library of 92 different materials with six replicates each in a randomized layout throughout the course of 20 min UVC irradiation.

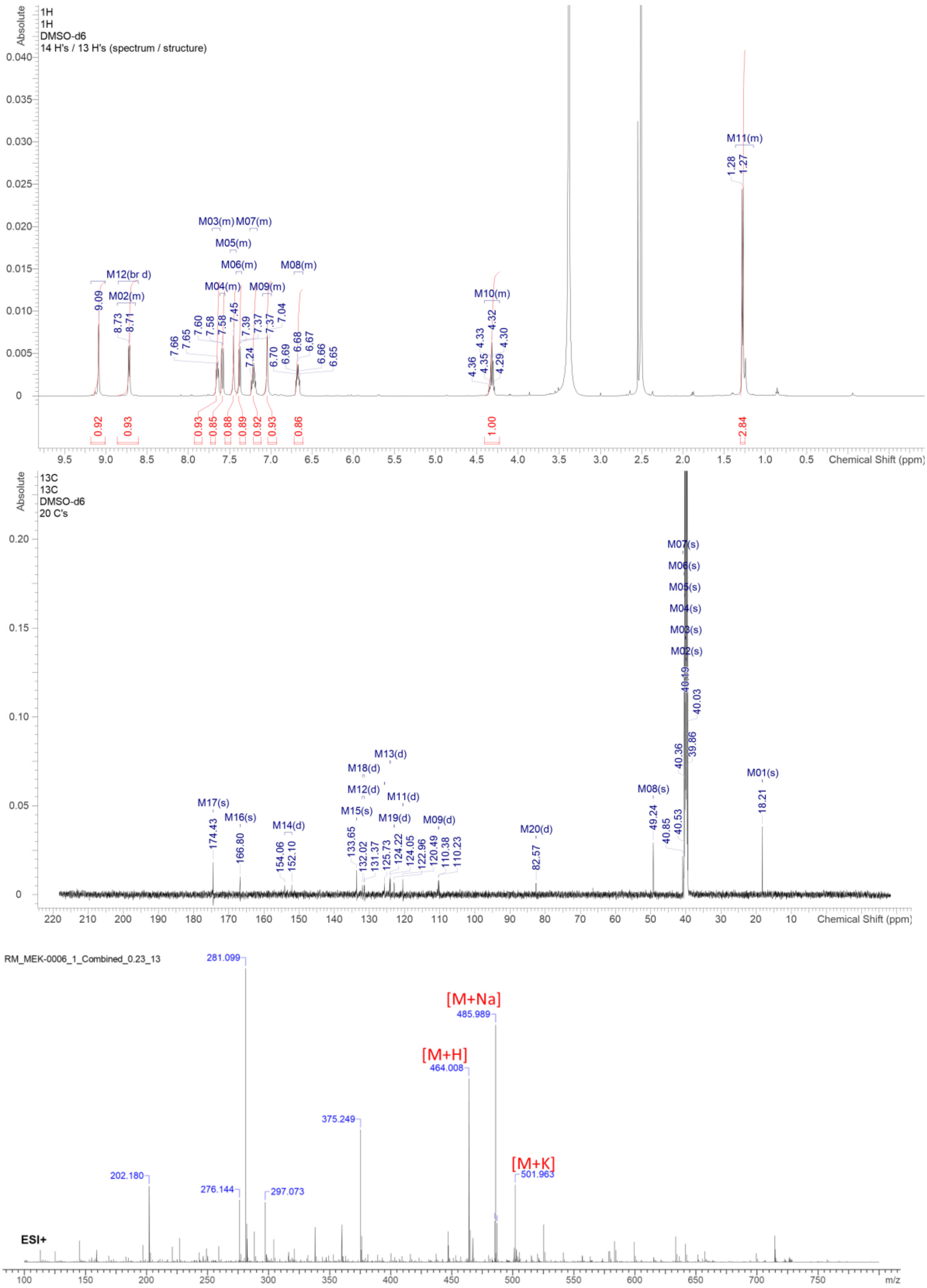

Supporting Figure 2: 1H- and 13C-NMR spectra and ESI-mass spectrum of compound **1**.

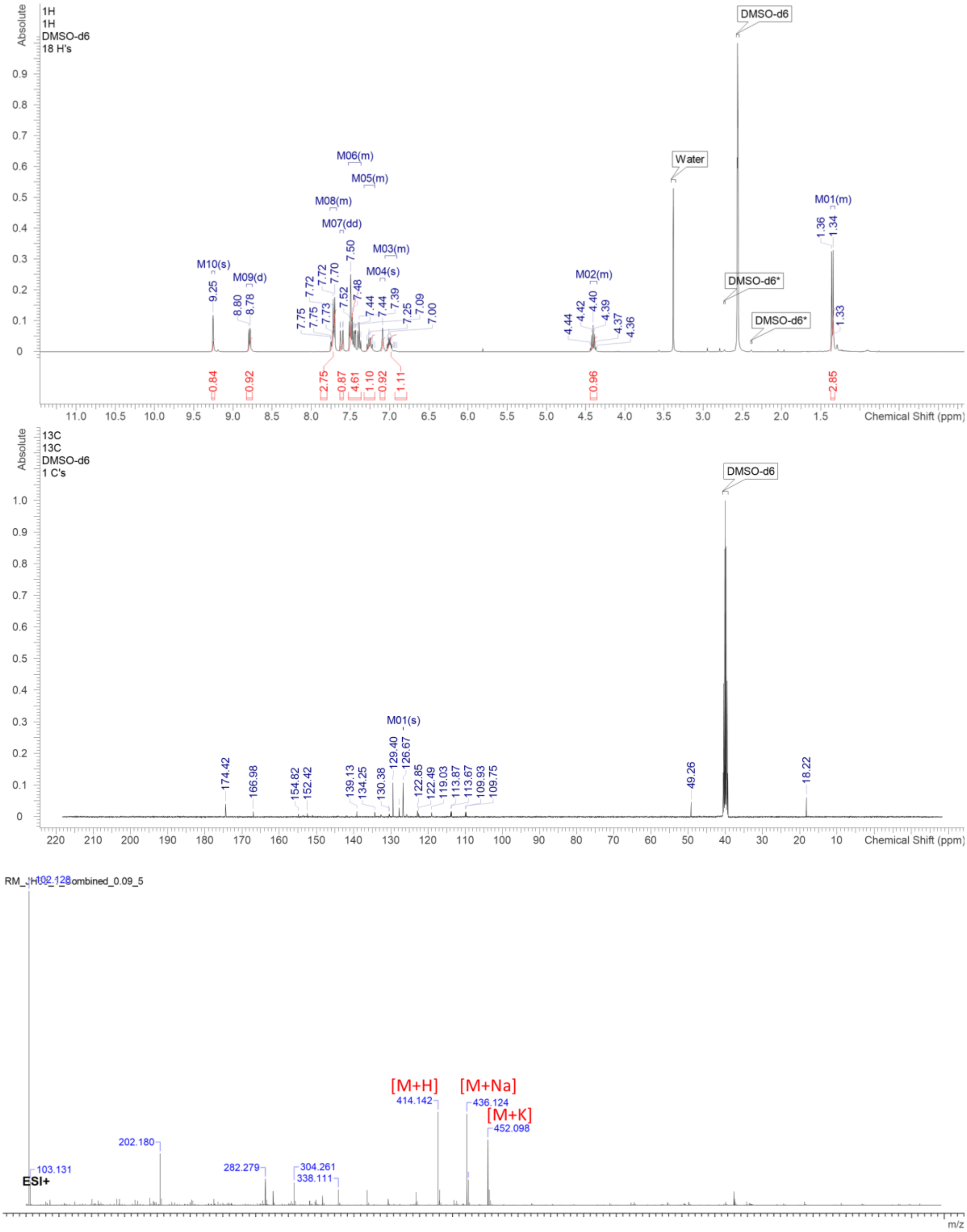

Supporting Figure 3: 1H- and 13C-NMR spectra and ESI-mass spectrum of compound **2.**

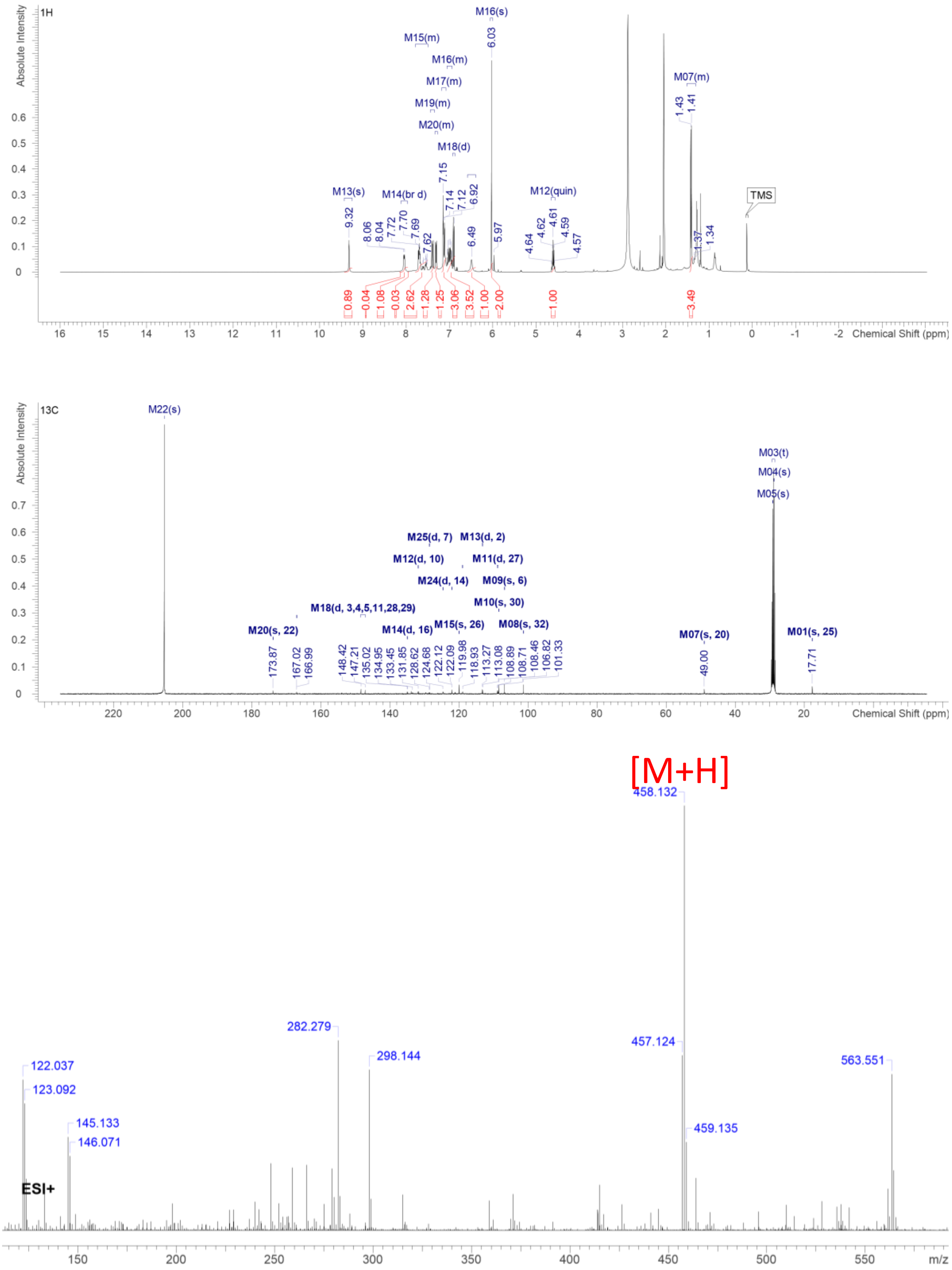

Supporting Figure 4: 1H- and 13C-NMR spectra and ESI-mass spectrum of compound **8**.

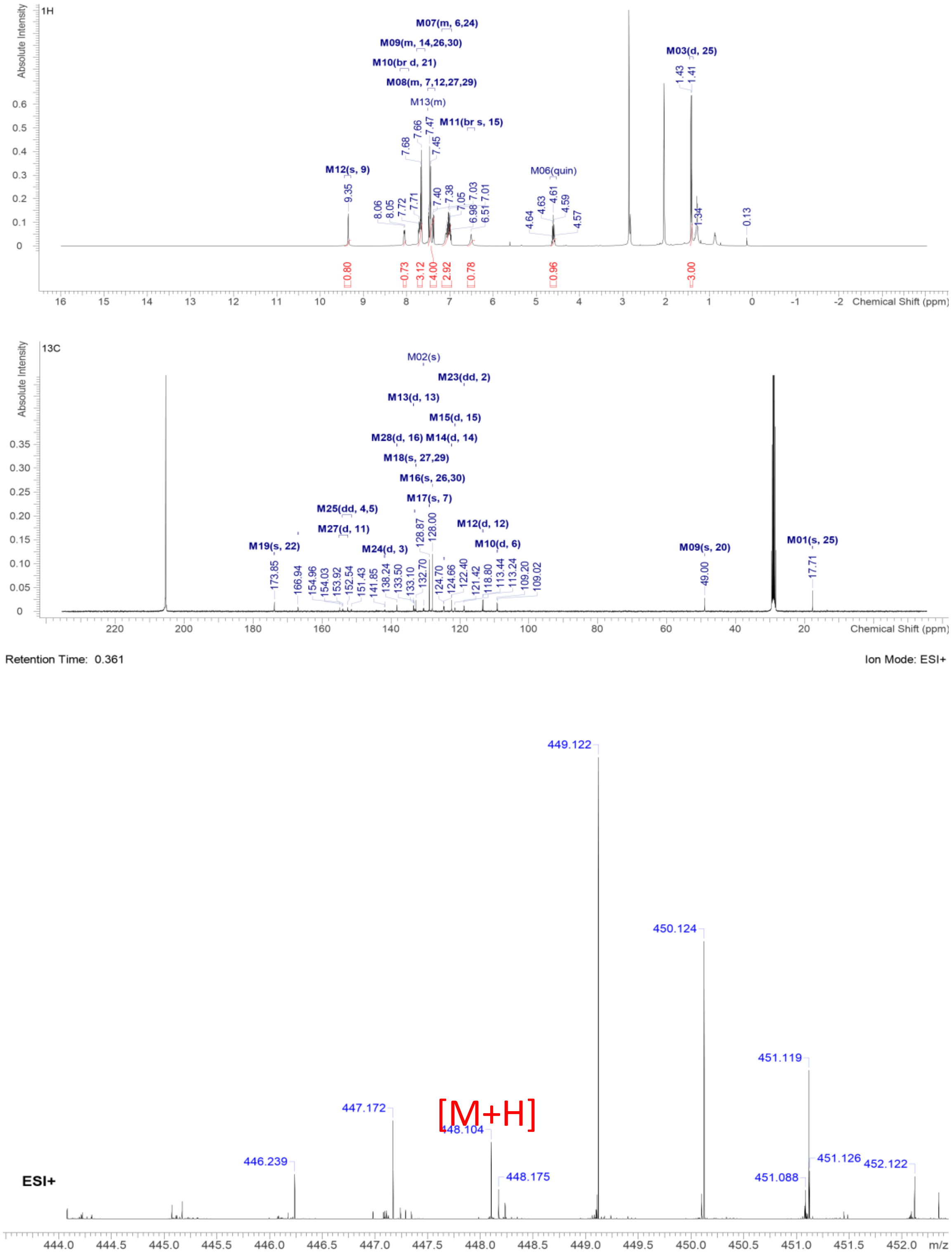

Supporting Figure 5: 1H- and 13C-NMR spectra and ESI-mass spectrum of compound **7.**

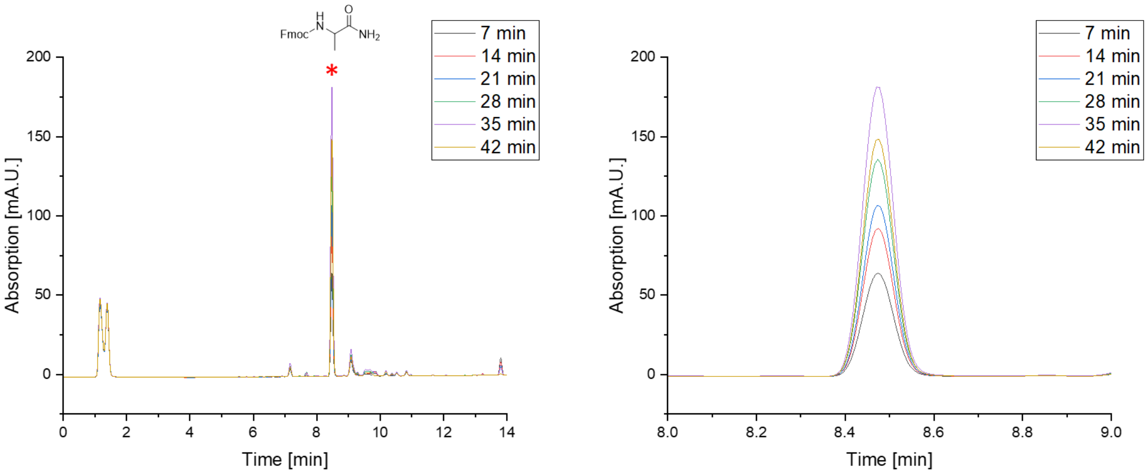

Supporting Figure 6: LC-MS measurements for the quantification of Fmoc-Ala-NH2 released from the surface of the DMA.

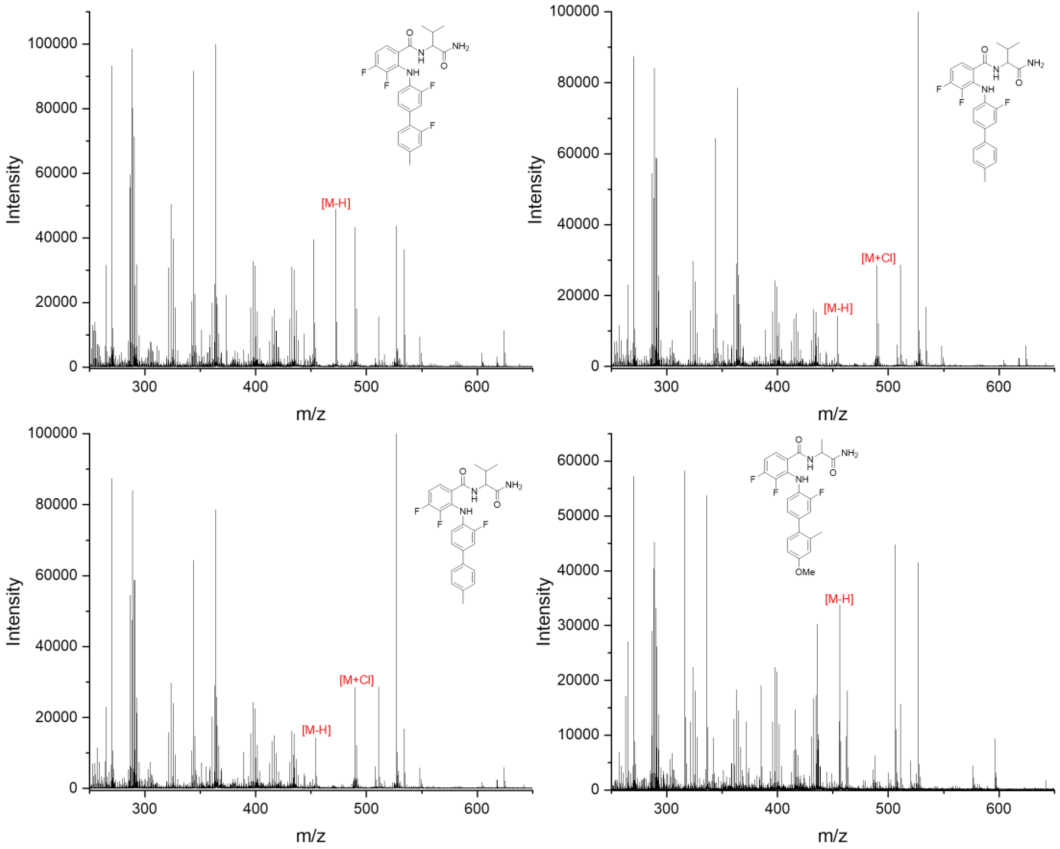

Supporting Figure 7: Exemplary MALDI-TOF-MS spectra of selected compounds, synthesized on the DMA and transferred to a ground steel target plate.

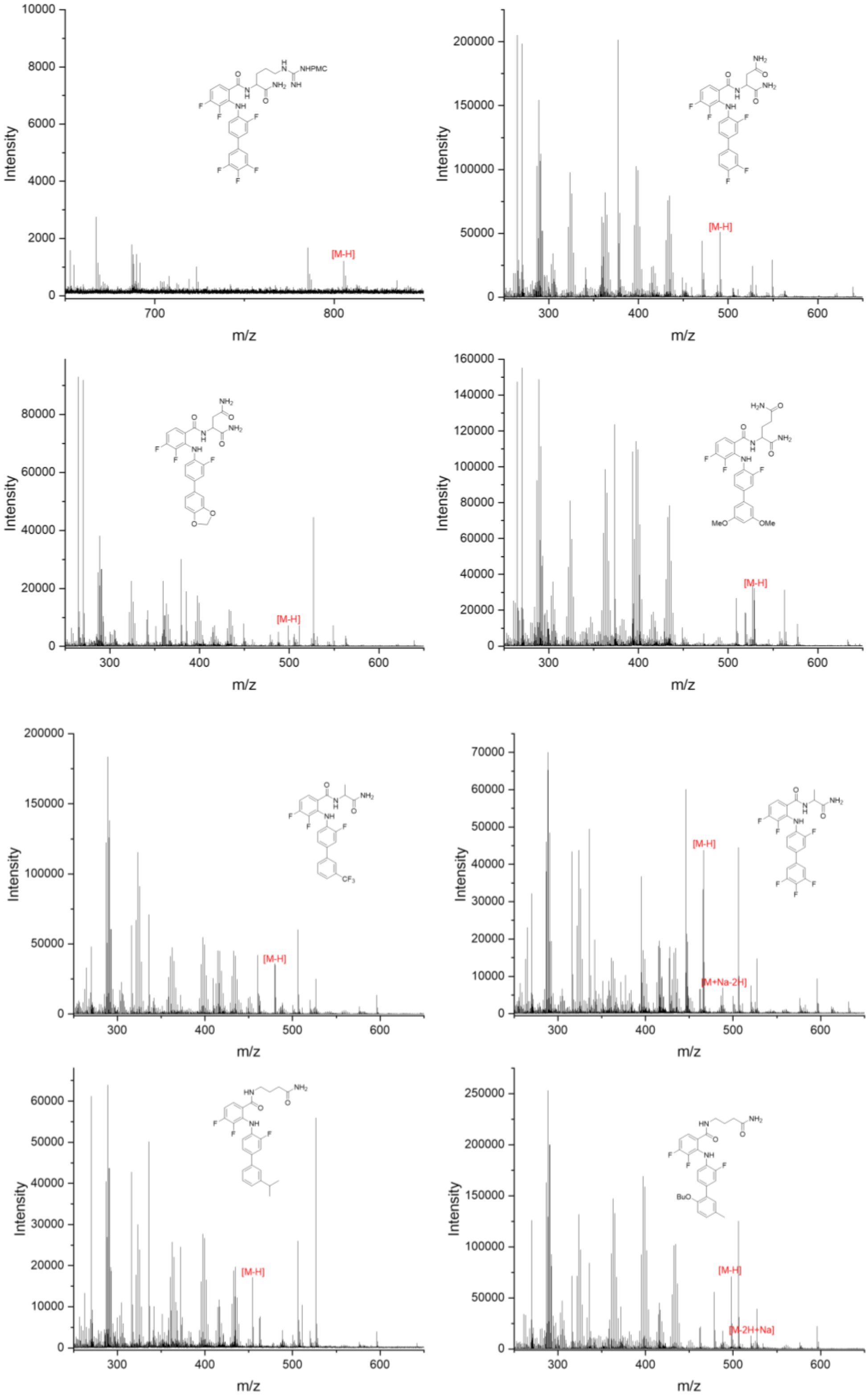

Supporting Figure 8: Exemplary MALDI-TOF-MS spectra of selected compounds, synthesized on the DMA and transferred to a ground steel target plate.

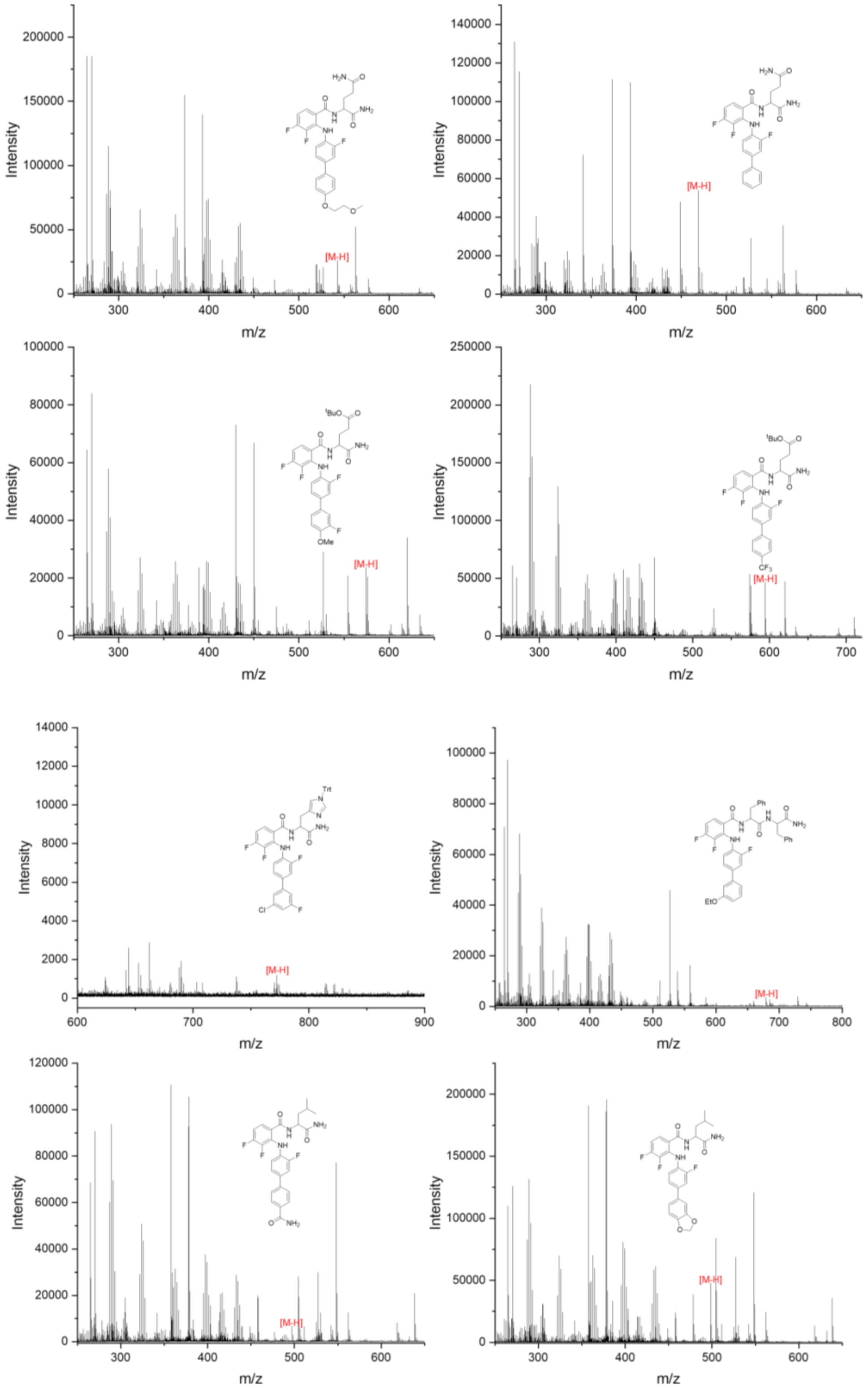

Supporting Figure 9: Exemplary MALDI-TOF-MS spectra of selected compounds, synthesized on the DMA and transferred to a ground steel target plate.

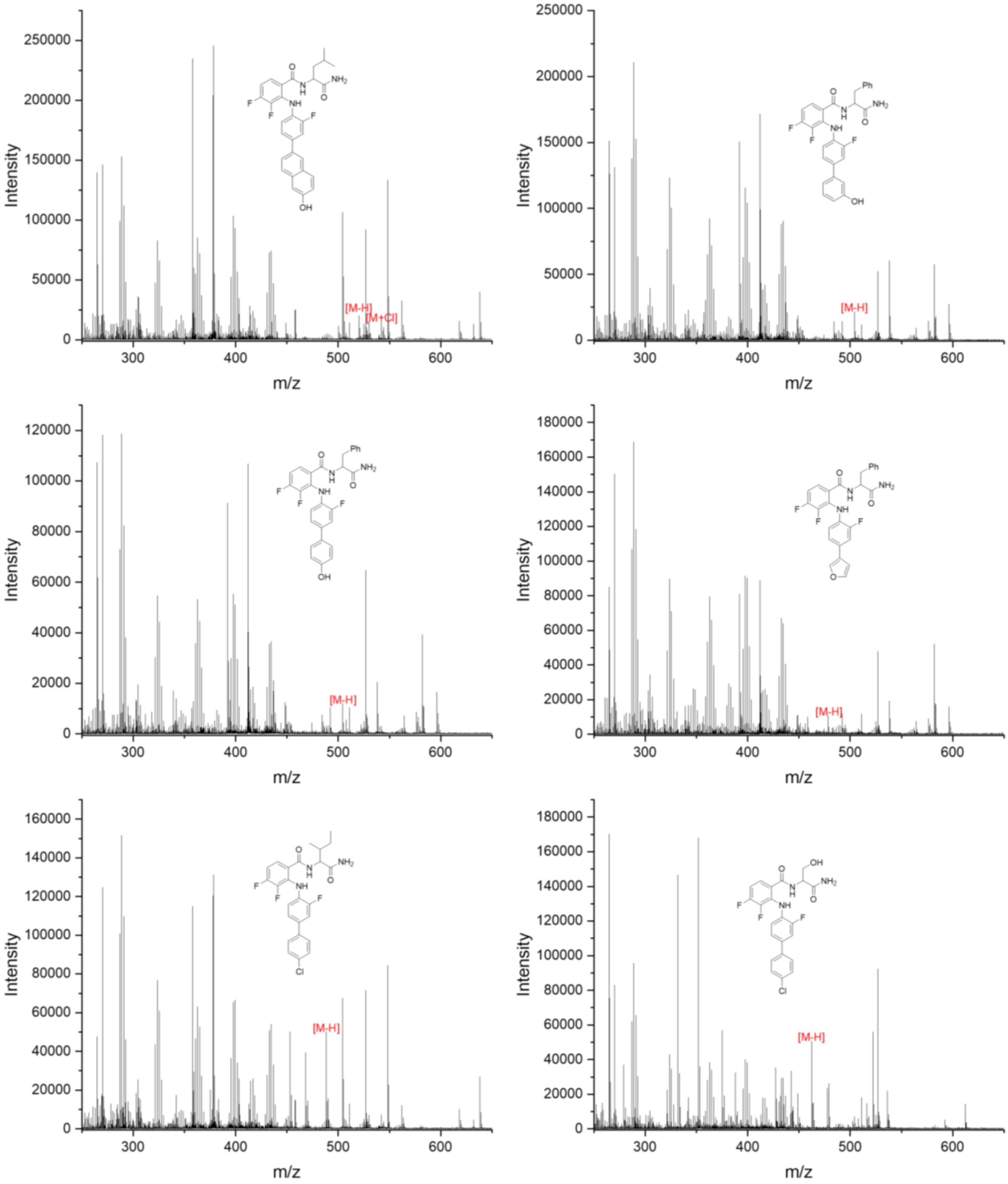

Supporting Figure 10: Exemplary MALDI-TOF-MS spectra of selected compounds, synthesized on the DMA and transferred to a ground steel target plate.

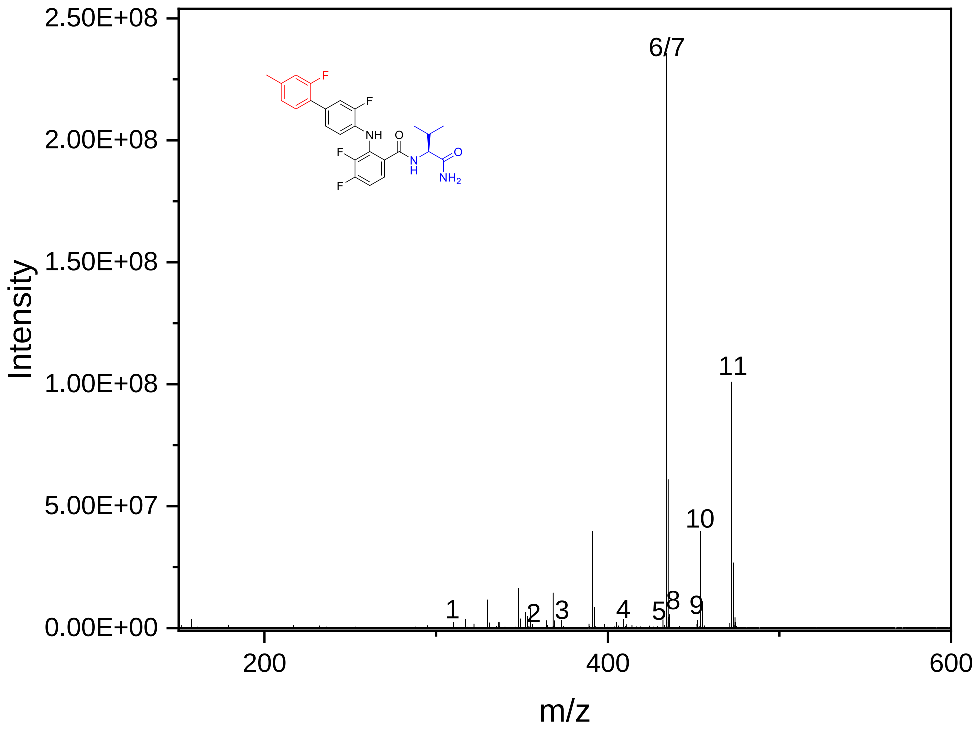

No.	m/z (Calc.)	m/z (Found)	Fragment	No.	m/z (Calc.)	m/z (Found)	Fragment
1	310.084908	310.080675	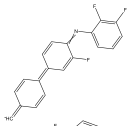	7	434.14857	434.140447	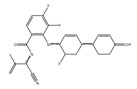
2	356.0704	356.084379	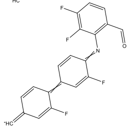	8	436.127835	436.146879	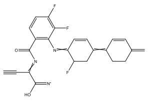
3	373.096949	373.090847	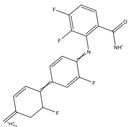	9	452.159135	452.14999	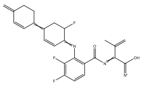
4	409.153321	409.146076	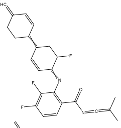	10	454.154799	454.145827	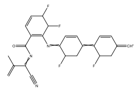
5	432.152907	432.144847	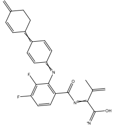	11	472.165363	472.156108	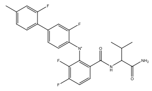
6	434.14857	434.140447	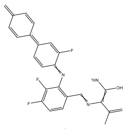				

Supporting Figure 11: Tandem MS-spectrum of a selected compound measured with an isolation window of ±1 Da around the [M-H]$^-$ peak with the according structures of the identified fragments.

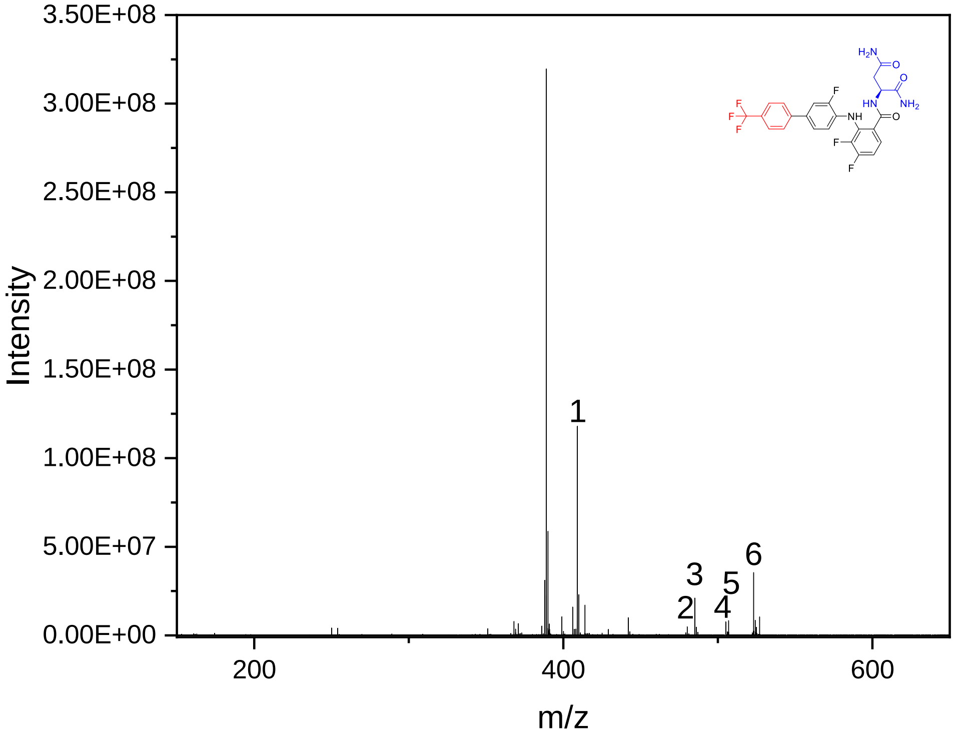

No.	m/z (Calc.)	m/z (Found)	Fragment	No.	m/z (Calc.)	m/z (Found)	Fragment
1	409.0781059	409.078106	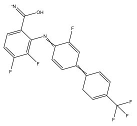	4	505.1104686	505.09857	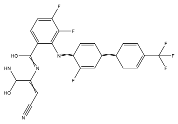
2	480.1152197	480.161571	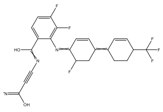	5	506.0944842	506.943538	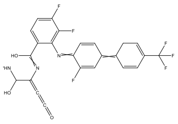
3	485.1042404	485.094032	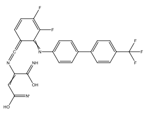	6	523.1210333	523.108686	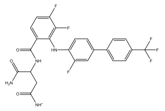

Supporting Figure 12: Tandem MS-spectrum of a selected compound measured with an isolation window of ±1 Da around the $[M-H]^-$ peak with the according structures of the identified fragments.

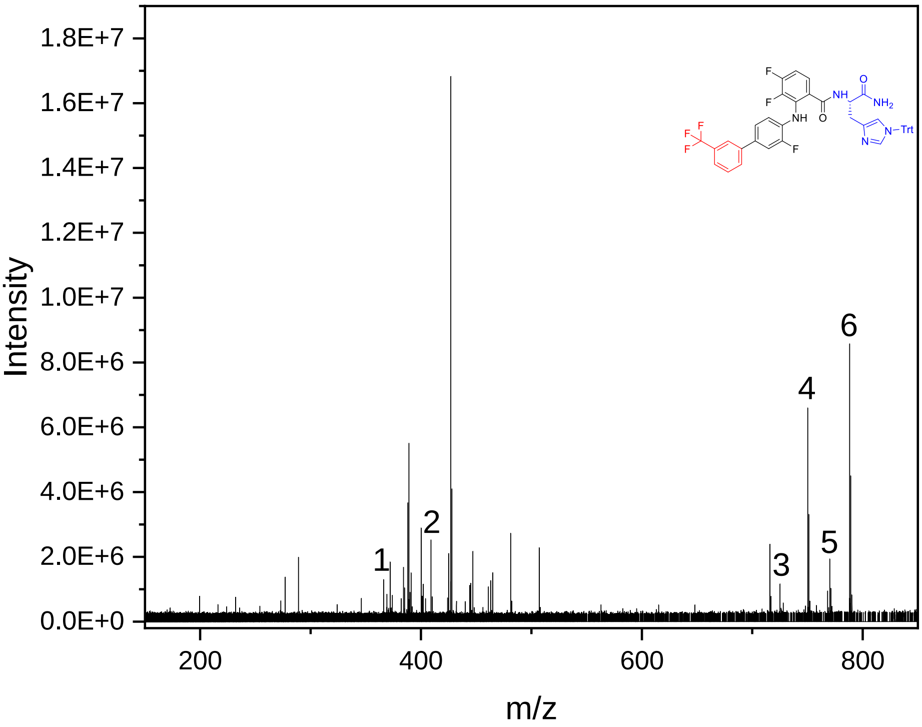

No.	m/z (Calc.)	m/z (Found)	Fragment	No.	m/z (Calc.)	m/z (Found)	Fragment
1	366.0722922	366.066343	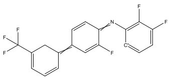	4	750.2297752	750.204194	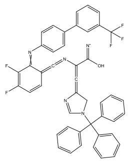
2	409.0781059	409.070505	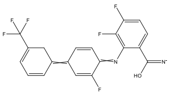	5	770.2360035	770.209349	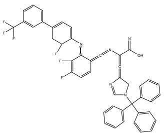
3	725.2345263	725.209731	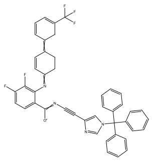	6	788.2465682	788.218714	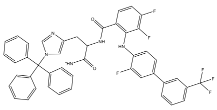

Supporting Figure 13: Tandem MS-spectrum of a selected compound measured with an isolation window of ±1 Da around the [M-H]$^-$ peak with the according structures of the identified fragments.

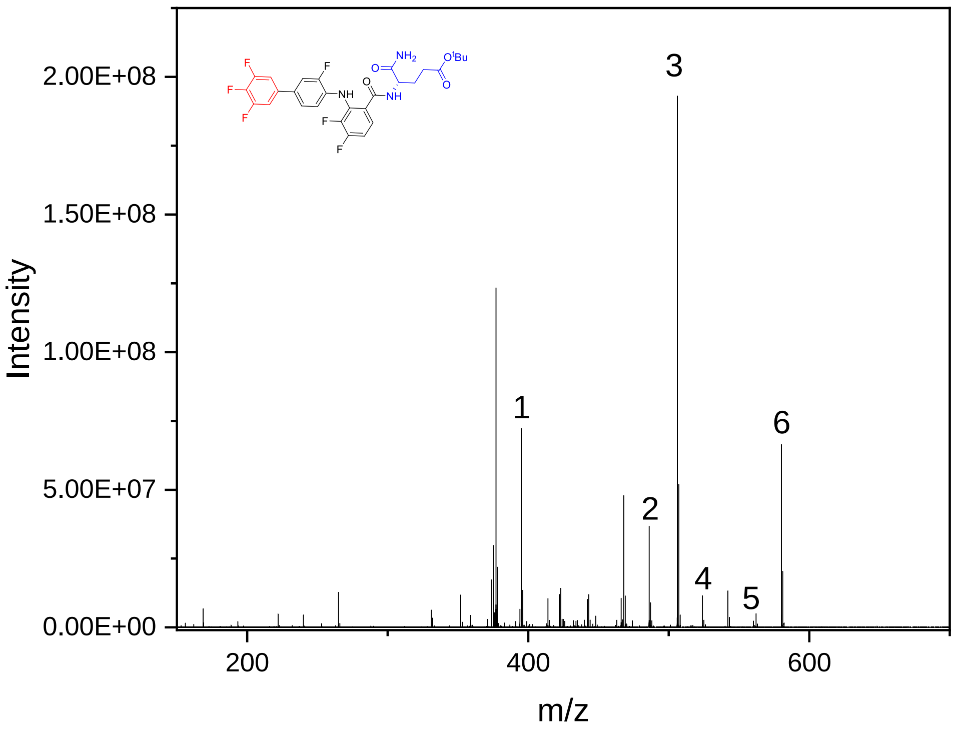

No.	m/z (Calc.)	m/z (Found)	Fragment	No.	m/z (Calc.)	m/z (Found)	Fragment
1	395.0624558	395.05561	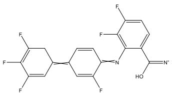	4	524.1050489	524.093125	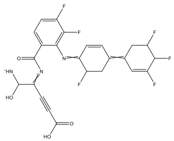
2	486.088256	486.07856	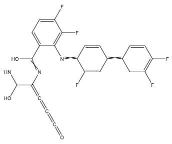	5	560.1614209	560.148181	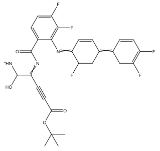
3	506.0944842	506.08373	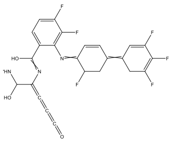	6	580.1676491	580.153075	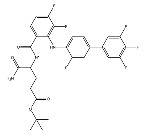

Supporting Figure 14: Tandem MS-spectrum of a selected compound measured with an isolation window of ±1 Da around the $[M-H]^-$ peak with the according structures of the identified fragments.

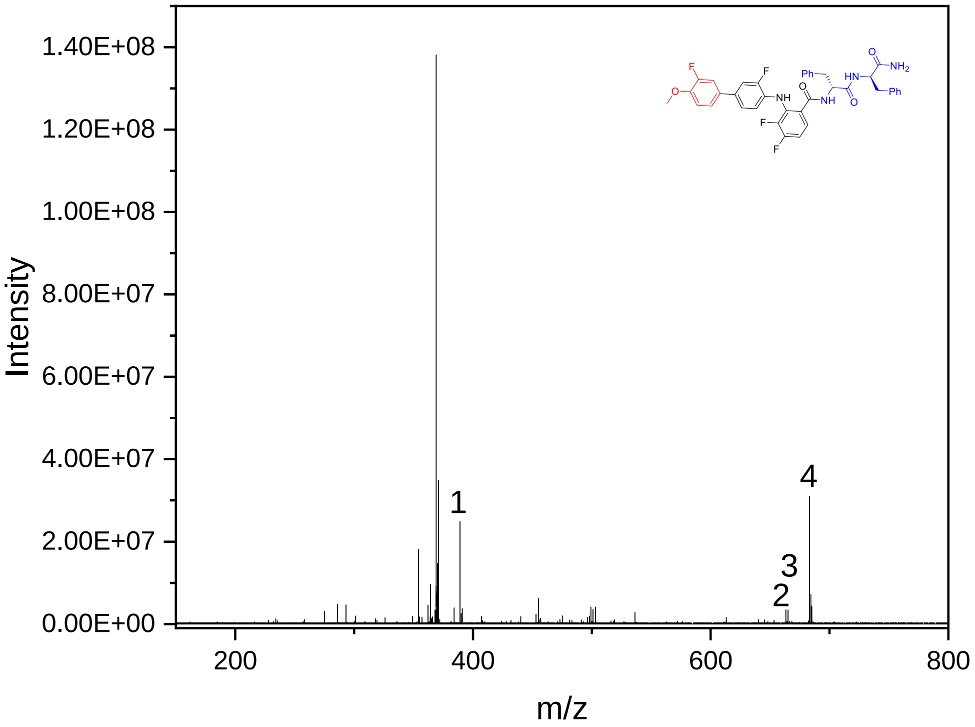

No.	m/z (Calc.)	m/z (Found)	Fragment	No.	m/z (Calc.)	m/z (Found)	Fragment
1	389.091864	389.085099	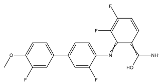	3	665.218127	665.196645	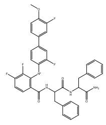
2	663.222464	663.20471	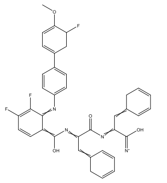	4	683.228692	683.228692	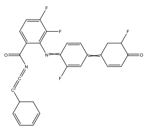

Supporting Figure 15: Tandem MS-spectrum of a selected compound measured with an isolation window of ±1 Da around the $[M\text{-}H]^-$ peak with the according structures of the identified fragments.

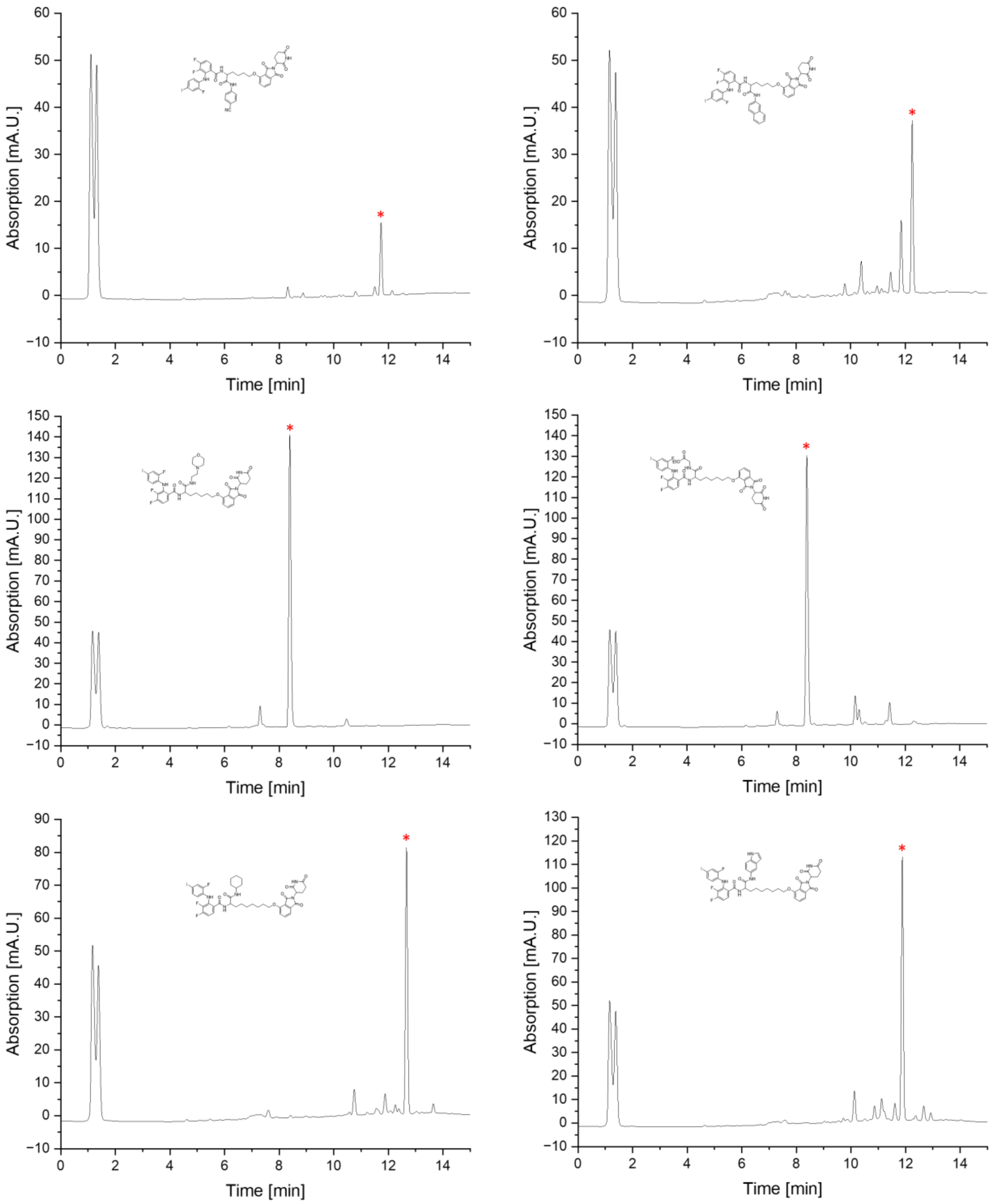

Supporting Figure 16: Exemplary LC-MS chromatograms of six different PROTAC-like molecules synthesized on DMA that were used to calculate the average purity of the compound library.

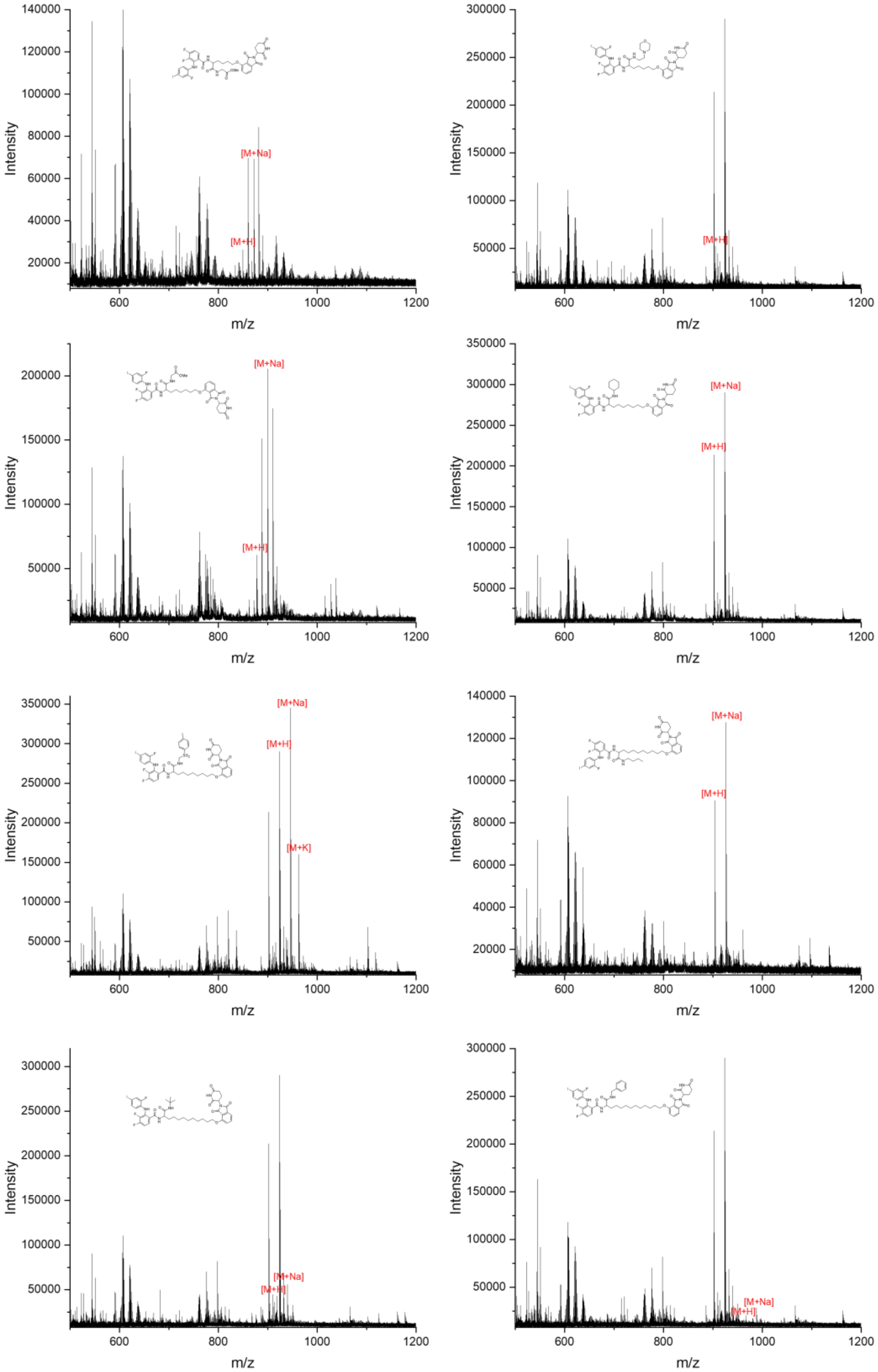

Supporting Figure 17: Exemplary MALDI-TOF-MS spectra measured for eight different PROTAC-like molecules, synthesized on DMA together with the target structure.

7 Acknowledgments

First of all, I want to thank my supervisor, Prof. Pavel Levkin, for the opportunity to conduct the research presented in this work in his lab. Besides this, thanks for the all the opportunities to learn and both acquire and develop skills that will prove highly valuable for my future.

Thanks to all my collaborators of years, especially Ye Tian, Stefan Schmidt, Pascal Friederich and Patrick Reiser. It is always a pleasure to work with you guys.

Thanks to Anna for always helping me when I as chemist ran into a problem with biological experiments, which somehow occurred surprisingly often.

Thanks to my lunch buddy Joaquin, who always manages to remind me of Pizza-Thursdays, you are the real MVP.

Special thanks to Janne, you always knew when I was about to starve and you always managed to save the situation.

Thanks to both my bachelor students/Hiwis Liana and Michelle, it could have been worse with you.

Huge thanks also to my lab buddy Julius, apparently it all worked out. I am just as surprised as you are.

I also want to thank all of the other members of the Levkin lab that I have encountered during my time there, both the discussions on and off the topic of scientific research were always helpful.

Finally, I want to thank my family: My parents, Christoph, my sister and her husband, my niece and my nephews, Frank and the most important of all, my girlfriend Rita. You guys always supported me when it was necessary and gave me the space and time to dive into work when I needed it. I couldn’t have done it without you.